

# **X-Ray Investigations of Mesoscopic Films at Liquid/Vapor Interfaces**

Dissertation  
zur Erlangung des Grades  
des Doktors der Naturwissenschaften  
der Naturwissenschaftlich-Technischen Fakultät II  
– Physik und Mechatronik –  
der Universität des Saarlandes



von

**VOLKER SCHÖN**

Saarbrücken

2013



Tag des Kolloquiums: 27.09.2013

Dekan: Univ.-Prof. Dr. Christian Wagner

Mitglieder des

Prüfungsausschusses: Univ.-Prof. Dr. rer. nat. J. Eschner (Vorsitz)

Univ.-Prof. Dr. rer. nat. P. Huber (Gutachter)

Univ.-Prof. Dr. rer. nat. R. Birringer (Gutachter)

Dr. rer. nat. M. Brust (Akademischer Mitarbeiter)



**There are two possible outcomes: if the result confirms the hypothesis, then you've made a measurement. If the result is contrary to the hypothesis, then you've made a discovery.**

- Enrico Fermi



# Affidavit

I hereby swear in lieu of an oath that I have independently prepared this thesis and without using other aids than those stated. The data and concepts taken over from other sources or taken over indirectly are indicated citing the source. The thesis was not submitted so far either in Germany or in another country in the same or a similar form in a procedure for obtaining an academic title.

Saarbrücken, October 10, 2013

Volker Schön



# Preface

When Wilhem Conrad Röntgen first reported to the *Physikalisch-medizinische Gesellschaft zu Würzburg* in 1895 on the new kind of rays - which he came to call x-rays ("for the sake of brevity" [1]) - he had begun to explore two months before, he still knew very little about them. He had discovered that these invisible rays were emanating from Crookes or Hittorf tubes - cold cathode discharge tubes - and that they were different from the already known cathode rays.

For once, they were cast in virtually every direction whereas the cathode rays were strictly directed towards the anode end. Moreover, they were able to pass through fairly large chunks of matter, quite thick books for instance. On the other hand, he noticed that for certain materials - like lead or platinum - only small amounts were required to block the x-rays completely. Apparently, the material's absorption qualities were somehow connected to its density.

And of course, when his wife held her hand between a tube and a photographic plate - that had proven to be quite sensitive to the new rays - they produced a pronounced contrast between her bones and the fleshy regions around them, a remarkable discovery that has saved many lives, helped cure many illnesses to this day and earned him a well deserved first Nobel Prize in physics.

But still he knew little about the nature of the new-found kind of radiation.

Another 27 years had to pass before Max von Laue (together with his colleagues Paul Knipping and Walter Friedrich) found evidence that x-rays are in fact electromagnetic waves - only with a much shorter wave length than visible light - and simultaneously showed the lattice structure of crystalline materials, thus laying the foundation for modern x-ray diffraction techniques with another Nobel Prize work.

Nowadays, x-rays are widely understood and serve as a means to acquire scientific insights themselves. While the most common application of x-rays is still mapping the interior of human bodies for medical analysis, they are relevant in many other fields as well. On the mesoscale (i.e. on length scales between micrometers and nanometers), x-ray diffraction - in all its various implementations - is one of the most versatile investigative instruments scientists have these days.

## **Abstract**

For this study, a university lab based x-ray reflectometer suitable for the investigation of liquid surfaces was designed and constructed. A highly automatizing computer program was written to control the installation.

A proof-of-concept measurement determining the structure of silane films on silicon substrates was performed.

Ensuing, the reflectometer was used to analyze the surface structure of Langmuir films of amphiphilic diblock copolymers. A probable scenario for the orientation of the hydrophobic part's side chains on the water surface could be given.

Additionally, the surface multilayer formation of gold nanoparticles suspended in toluene was discovered and investigated. A dependence on the suspension's concentration and temperature as well as the reversibility of the multilayer formation could be verified albeit the latter shows a small hysteresis.

## **Kurzdarstellung**

Für diese Studie wurde ein Röntgenreflektometer in einem Universitätslabor errichtet, das für die Untersuchung flüssiger Oberflächen tauglich ist. Zur Kontrolle der Anlage wurde ein stark automatisierendes Computerprogramm geschrieben.

Eine Messung zur Bestimmung der Struktur eines Silanfilms auf einem Siliziumsubstrat zeigt die Anwendbarkeit des Aufbaus.

Anschließend wurde das Reflektometer dazu verwendet die Struktur von Langmuirfilmen amphiphiler Diblock-Copolymere zu analysieren. Ein wahrscheinliches Szenario für die Ausrichtung der Nebenkette des hydrophoben Teils auf der Wasseroberfläche konnte gefunden werden.

Zudem wurde die Multilagenbildung von Goldnanopartikeln suspendiert in Toluol entdeckt und untersucht. Eine Abhängigkeit von Konzentration und Temperatur der Suspension sowie die Reversibilität der Multilagenbildung konnte nachgewiesen werden, wobei letztere eine leichte Hysterese aufweist.

# Contents

<b>Introduction</b>	<b>5</b>
<b>Outline</b>	<b>6</b>
<b>I Preliminary</b>	<b>7</b>
<b>1 Reflection of X-Rays</b>	<b>9</b>
1.1 The Index of Refraction . . . . .	9
1.2 External Total Reflection . . . . .	11
1.3 Unstructured Surfaces - Fresnel Reflectivity . . . . .	12
1.4 Structured Surfaces - Parratt Method . . . . .	15
1.5 Roughness . . . . .	17
1.5.1 Capillary Waves . . . . .	19
<b>2 Experimental Setup</b>	<b>21</b>
2.1 Incident Side . . . . .	21
2.1.1 X-Ray Source . . . . .	21
2.1.2 Multilayer Mirror . . . . .	21
2.2 Sample . . . . .	22
2.3 Detector side . . . . .	23
2.4 Alignment . . . . .	23
2.5 Control . . . . .	25
<b>3 Proof of Concept: Characterization of Hydrophobized Si-Wafers</b>	<b>27</b>
3.1 Sample Composition . . . . .	27
3.2 Measurements . . . . .	28
3.3 Conclusions . . . . .	29
<b>II Constitutive</b>	<b>31</b>
<b>4 Langmuir Films of Amphiphilic Diblock Copolymers</b>	<b>33</b>
4.1 Amphiphilic Polymers . . . . .	33
4.2 Polymer Synthesis . . . . .	35

---

4.3	Compression Isotherms . . . . .	35
4.4	X-Ray Reflectivity Measurements . . . . .	37
4.4.1	PEO <sub>5</sub> F <sub>22</sub> . . . . .	38
4.4.2	PEO <sub>5</sub> F <sub>64</sub> . . . . .	39
4.5	Conclusion . . . . .	40
<b>5</b>	<b>Surface Layering of Suspended Au-Nanoparticles</b>	<b>41</b>
5.1	Nanoparticle Suspensions . . . . .	41
5.2	Monolayer Formation . . . . .	42
5.3	Monolayer Electron Density . . . . .	44
5.4	Pure Toluene . . . . .	45
5.5	Multilayers . . . . .	47
5.5.1	Formation . . . . .	47
5.5.2	Temperature Ramps . . . . .	47
5.5.3	Reproducibility . . . . .	50
5.5.4	Conclusions . . . . .	50
5.6	Layering Peak Temperature Ramp . . . . .	53
5.7	Bulk Agglomerates . . . . .	55
<b>6</b>	<b>Summary</b>	<b>57</b>
6.1	Outlook . . . . .	58
	<b>III Supplemental</b>	<b>59</b>
<b>A</b>	<b>X-Surf</b>	<b>61</b>
A.1	List of Commands . . . . .	61
A.2	Screenshot . . . . .	63
A.3	List of Motors . . . . .	64
<b>B</b>	<b>Calculations</b>	<b>65</b>
B.1	Thiol Layer Density . . . . .	65
B.2	Complete NP (Mono)-Layer Density Model . . . . .	68
<b>C</b>	<b>Additional Figures</b>	<b>73</b>
	<b>List of Figures</b>	<b>77</b>
	<b>Bibliography</b>	<b>79</b>
	<b>Acknowledgements</b>	<b>91</b>

# Introduction

Nowadays, nanosciences and technologies have permeated almost every aspect of our lives – From self-cleaning ceramics in kitchens to more efficient catalytic converters in cars. From fire protective coatings to specially tailored drug delivery systems that take the active ingredients only to those cells that need them.

Even more so than microscopic ones, meso- and nanoscopic systems are largely dominated by surficial and interfacial effects. While in bulk materials any given atom or molecule is mostly in contact with their own kind, the confinement to nanoscales, and thus to a small number of atoms, causes many of them to be primarily surrounded by alien particles (or nothing).

Usually, the stability of a nanoscopic structure will be uncertain and has to be artificially maintained. There is quite a number of means to achieve this. For instance, there is the possibility of encasing a material in a porous matrix or to have ligand molecules sterically stabilize singular particles.

Furthermore, there are systems that are only confined in one or two dimensions, effectively forming a two- or one-dimensional entity. Carbon nanotubes are an example for such a one-dimensional structure. One realization of confinement to two dimensions are Langmuir layers, i.e. films on the surface of a liquid (or at the interface between two liquids) composed of amphiphilic molecules.

Amphiphilic molecules consist of a part that is soluble in the liquid phase and one that is not. Usually this means that there is a polar end and a non-polar end.

First and foremost, this work is to show the feasibility of an x-ray anode based reflectometer even for a liquid sample. Managing a liquid sample is generally a bit more challenging as opposed to a solid one. They require additional effort to keep them contained as they are more prone to contamination and for the most part, they exhibit a certain amount of volatility.

In addition to that, apart from liquid metals, which are not part of this study, liquid samples tend to have a lower electron density which leads to a reduction in reflectivity that can only be overcome by increasing the brilliance of the primary beam. That is why a synchrotron is traditionally used as the x-ray source when it comes to liquid samples.

While the tremendous increase in brilliance is a clear advantage of synchrotrons

versus simple x-ray anodes, their operational expenses are equally immense and their availability quite limited. An x-ray anode based reflectometer can be run in any standard university lab.

Also, the orientation of their surface is entirely governed by the direction of gravity which also necessitates a vertically oriented plane of reflection. Thus, either the anode (which can be quite heavy) or the sample (which can be quite sensitive) has to be moved against gravitational forces which adds to the challenge.

## **Outline**

In the first part, the technique of x-ray reflectivity measurements will be covered as well as the actual setup built and then used in this study. Concluding, a proof-of-concept measurement demonstrating the usability of the reflectometer will be presented.

The second part will present the two main studies performed using the installation: An analysis of the structure of Langmuir films of amphiphilic diblock copolymers and an investigation of the occurrence of a surface multilayer formation in a gold nanoparticle suspension.

The third part will give some supplemental information such as some additional figures and a detailed presentation of the nanoparticle electron density model used for the analysis in the second chapter of part II.

# Part I

## Preliminary

In this part, the general theory of x-ray reflectometry as well as the instrument built during this work will be described. It also includes a proof-of-concept demonstration of the applicability of the setup.



# 1 Reflection of X-Rays

X-ray reflectometry is a non-invasive technique probing the vertical electron density profile at an interface - mostly the surface of a rigid body, but also that of a liquid. Because of the finite dimensions of the x-ray beam, there is an averaging of the lateral structure in the area of the beam's footprint. Thus a necessary prerequisite for the feasibility of x-ray reflectometry is for the structure of the investigated sample to be laterally homogeneous at least to some extent.

The penetration depth of perpendicularly impinging x-rays is already rather low: usually on the order of a few hundred micrometers. Due to the grazing incidence used in x-ray reflectometry, the penetration depth is further reduced making the technique mostly sensitive to the region less than one micrometer below the irradiated surface.

## 1.1 The Index of Refraction

Although x-rays are electromagnetic radiation just like visible light, there are certain peculiarities in their interaction with matter. Basically, as described for x-rays in reference [2] or more generally in reference [3], the electrons (that are modeled to be bound elastically to the nuclei) are solely interacting with the electromagnetic field of the x-rays.

The movement of a charge  $q$  with mass  $m$  in an electric field  $E$  has to obey the general equation

$$m \frac{d^2 \vec{r}}{dt^2} + k \vec{r} = -q \vec{E}(t) \quad (1.1.1)$$

where  $k$  is the spring constant of the electron-nucleus system. Solving the equation for an electron of charge  $-e$  and the field  $\vec{E}(t) = E_0 e^{i\omega t}$  yields

$$\vec{r} = \frac{e \vec{E}(t)}{m(\omega_0^2 - \omega^2)} \quad (1.1.2)$$

with

$$\omega_0^2 = \frac{k}{m}. \quad (1.1.3)$$

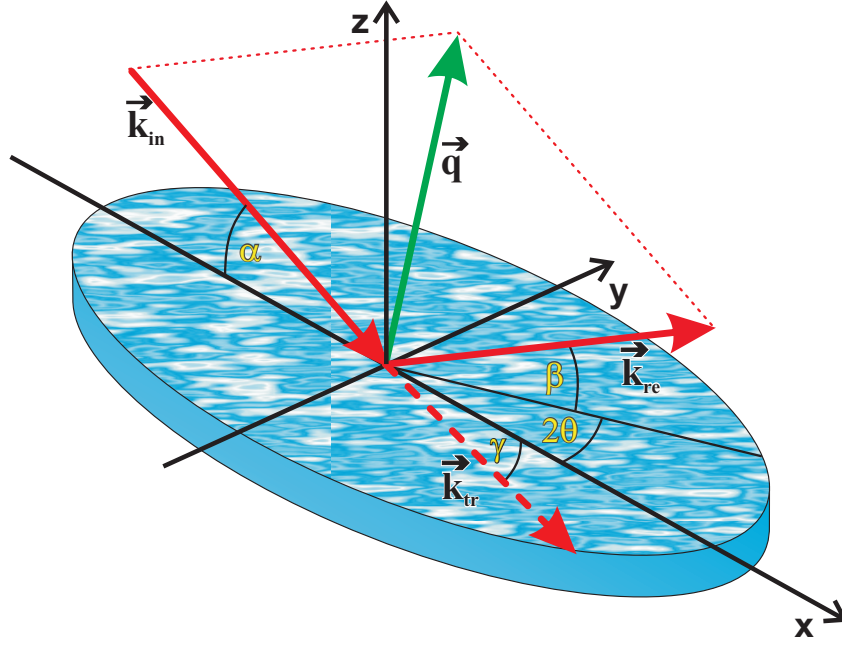


**Figure 1.1:** Geometry of x-ray reflection: Incident beam  $\vec{k}_{in}$  - reflected beam  $\vec{k}_{re}$  - transmitted beam  $\vec{k}_{tr}$ .  $\vec{q}$  is the wave vector transfer from the surface to the photon.

Since  $\omega_0$  is approximately four orders of magnitude smaller than  $\omega$  for x-rays, it can be neglected, reducing (1.1.2) to

$$\vec{r} \approx \frac{-e\vec{E}(t)}{m\omega^2} \quad (1.1.4)$$

Each electron generates the dipole moment  $\vec{p} = e\vec{r}$  so the polarization density  $\vec{P}$  can be expressed by

$$\vec{P} = \rho\vec{p} \quad (1.1.5)$$

where  $\rho$  is the electron density.

Using the relation

$$\vec{P} = \epsilon_0\chi\vec{E} \quad (1.1.6)$$

with (1.1.4) and (1.1.5) yields

$$\epsilon_0\chi\vec{E} = -\frac{\rho e^2\vec{E}}{m\omega^2}. \quad (1.1.7)$$

Here,  $\chi$  is the dielectric susceptibility and  $\epsilon_0$  is the permittivity of vacuum. Since  $\chi$  and the relative permittivity  $\epsilon_r$  are connected via  $\epsilon_r = 1 + \chi$  and the refractive index  $n = \sqrt{\epsilon_r}$ , eliminating  $\vec{E}$  from (1.1.7) leads to

$$n = \sqrt{1 - \frac{\rho e^2}{m\epsilon_0\omega^2}} \quad (1.1.8)$$

and since the second term under the square root is much smaller than unity (usually about  $10^{-6}$ )

$$n = 1 - \frac{\rho e^2}{2m\varepsilon_0\omega^2} \quad (1.1.9)$$

is a very good approximation. With

$$r_e = \frac{e^2}{4\pi\varepsilon_0 mc^2} \quad (1.1.10)$$

(1.1.9) becomes

$$n = 1 - \frac{r_e \rho \lambda^2}{2\pi}. \quad (1.1.11)$$

The last term usually referred to as  $\delta$ . In a more strict quantum mechanical calculation, the anomalous form factor of the atoms has to be considered, but its influence is very small and negligible in most cases especially for small incident angles as they occur in x-ray reflectometry.

## 1.2 External Total Reflection

Figure 1.1 depicts how x-rays interact with a surface. Contrary to the practice in classical optics, the angles are not measured from the surface normal but with respect to the surface plane. The incident beam  $\vec{k}_{\text{in}}$  takes the wave vector transfer  $\vec{q}$  from the material and is scattered in the direction  $\vec{k}_{\text{re}}$ . For specular reflection  $\vec{k}_{\text{re}}$  has no component normal to the incident plane, i.e. that spanned by  $\vec{k}_{\text{in}}$  and the surface normal, and the incident angle  $\alpha$  and reflected angle  $\beta$  are of identical value. This also implies that  $\vec{q}$  is normal to the surface.

Generally, the index of refraction for x-rays is

$$n(\vec{r}) = 1 - \delta(\vec{r}) + i\beta(\vec{r}), \quad (1.2.1)$$

$\delta$  was introduced in the previous section and

$$\beta = \frac{\lambda}{4\pi} \mu(\vec{r}). \quad (1.2.2)$$

with the linear absorption coefficient  $\mu(\vec{r})$ .

This way, equation (1.2.1) can be expressed in a simplified manner by

$$n = 1 - \frac{\lambda^2}{2\pi} r_e \rho + i \frac{\lambda}{4\pi} \mu. \quad (1.2.3)$$

For a simple surface the angle of the transmitted, refracted beam  $\gamma$  can be calculated by

$$\gamma = \arccos(n \cdot \cos(\alpha)) = \arccos((1 - \delta) \cdot \cos(\alpha)). \quad (1.2.4)$$

Absorption is neglected here since usually  $\beta/\delta \approx 10^{-1}$  to  $10^{-2}$ .

For  $\gamma = 0$  and since  $\delta$  is very small, the critical angle  $\alpha_c$  can be written as

$$\alpha_c \approx \sqrt{2\delta} = \lambda \sqrt{r_e \rho / \pi}. \quad (1.2.5)$$

So for incident angles below  $\alpha_c$  - apart from some absorption losses - instead of being refracted all incoming photons are externally reflected from the medium and do not permeate the surface far into the bulk.

Since the wave length of the x-rays is usually a known quantity,  $\rho$  can be determined simply by measuring the critical angle of a given surface.

### 1.3 Unstructured Surfaces - Fresnel Reflectivity

If the electric part of a plane wave with wave vector  $\vec{k}_{\text{in}}$  (cf. figure 1.1) and amplitude  $\vec{E}_{\text{in}}$  impinging on a surface is separated into components parallel and perpendicular to the plane of incidence  $E_{\text{in}}^{\parallel}$  and  $E_{\text{in}}^{\perp}$ , the basic components can be expressed as ( $E^{\parallel}$  is always chosen, so the  $z$ -component is positive)

$$\vec{E}_{\text{in}} = \begin{pmatrix} E_{\text{in}}^{\parallel} \sin(\alpha) \\ E_{\text{in}}^{\perp} \\ E_{\text{in}}^{\parallel} \cos(\alpha) \end{pmatrix} e^{-i(\omega t - \vec{k}_{\text{in}} \cdot \vec{r})} \quad (1.3.1a)$$

If  $E_{\text{re}}$  and  $E_{\text{tr}}$  are the amplitudes of the transmitted and reflected field respectively, their respective components are

$$\vec{E}_{\text{re}} = \begin{pmatrix} -E_{\text{re}}^{\parallel} \sin(\beta) \\ E_{\text{re}}^{\perp} \\ E_{\text{re}}^{\parallel} \cos(\beta) \end{pmatrix} e^{-i(\omega t - \vec{k}_{\text{re}} \cdot \vec{r})} \quad (1.3.1b)$$

$$\vec{E}_{\text{tr}} = \begin{pmatrix} E_{\text{tr}}^{\parallel} \sin(\gamma) \\ E_{\text{tr}}^{\perp} \\ E_{\text{tr}}^{\parallel} \cos(\gamma) \end{pmatrix} e^{-i(\omega t - \vec{k}_{\text{tr}} \cdot \vec{r})} \quad (1.3.1c)$$

Analogous equations can be written for the magnetic field vectors  $\vec{H}$  since

$$\vec{H}_x = \sqrt{\frac{\varepsilon_n}{\mu_n}} \vec{e}_{k_x} \times \vec{E} \quad (1.3.2)$$

where  $\vec{e}_k$  is the unit vector in direction of  $\vec{k}$ , i.e. in the wave's direction of propagation, giving another set of three times three equations. The index  $n$  on the

permittivity and permeability is either 0 or 1, when referring to vacuum or the medium respectively while  $x$  is either *in*, *re* or *tr*.

$$\vec{H}_{\text{in}} = \begin{pmatrix} E_{\text{in}}^{\perp} \sin(\alpha) \\ -E_{\text{in}}^{\parallel} \\ E_{\text{in}}^{\perp} \cos(\alpha) \end{pmatrix} \sqrt{\frac{\varepsilon_0}{\mu_0}} e^{-i(\omega t - \vec{k}_{\text{in}} \cdot \vec{r})} \quad (1.3.3a)$$

$$\vec{H}_{\text{re}} = \begin{pmatrix} -E_{\text{re}}^{\perp} \sin(\beta) \\ -E_{\text{re}}^{\parallel} \\ E_{\text{re}}^{\perp} \cos(\beta) \end{pmatrix} \sqrt{\frac{\varepsilon_0}{\mu_0}} e^{-i(\omega t - \vec{k}_{\text{re}} \cdot \vec{r})} \quad (1.3.3b)$$

$$\vec{H}_{\text{tr}} = \begin{pmatrix} E_{\text{tr}}^{\perp} \sin(\gamma) \\ -E_{\text{tr}}^{\parallel} \\ E_{\text{tr}}^{\perp} \cos(\gamma) \end{pmatrix} \sqrt{\frac{\varepsilon_1}{\mu_1}} e^{-i(\omega t - \vec{k}_{\text{tr}} \cdot \vec{r})} \quad (1.3.3c)$$

Since the tangential components of the electric and magnetic fields have to be continuous, the following set of equations can be formed

$$E_{\text{in}}^x + E_{\text{re}}^x = E_{\text{tr}}^x \quad E_{\text{in}}^y + E_{\text{re}}^y = E_{\text{tr}}^y \quad (1.3.4a)$$

$$H_{\text{in}}^x + H_{\text{re}}^x = H_{\text{tr}}^x \quad H_{\text{in}}^y + H_{\text{re}}^y = H_{\text{tr}}^y \quad (1.3.4b)$$

Substituting equations (1.3.1) and (1.3.3) into (1.3.4) and using the fact that  $\sin(\alpha) = \sin(\beta)$  yields

$$\sin(\alpha) (E_{\text{in}}^{\parallel} - E_{\text{re}}^{\parallel}) = E_{\text{tr}}^{\parallel} \sin(\gamma) \quad (1.3.5a)$$

$$E_{\text{in}}^{\perp} + E_{\text{re}}^{\perp} = E_{\text{tr}}^{\perp} \quad (1.3.5b)$$

$$\sqrt{\frac{\varepsilon_0}{\mu_0}} \sin(\alpha) (E_{\text{in}}^{\perp} - E_{\text{re}}^{\perp}) = \sqrt{\frac{\varepsilon_1}{\mu_1}} E_{\text{tr}}^{\perp} \sin(\gamma) \quad (1.3.5c)$$

$$\sqrt{\frac{\varepsilon_0}{\mu_0}} (E_{\text{in}}^{\parallel} + E_{\text{re}}^{\parallel}) = \sqrt{\frac{\varepsilon_1}{\mu_1}} E_{\text{tr}}^{\parallel} \quad (1.3.5d)$$

For most materials,  $\mu$  does not differ very much from  $\mu_0$ , so  $\mu_1$  can be substituted for  $\mu_0$  and since  $n = \sqrt{\frac{\varepsilon_1 \mu_1}{\varepsilon_0 \mu_0}}$

$$E_{\text{in}}^{\parallel} - E_{\text{re}}^{\parallel} = E_{\text{tr}}^{\parallel} \frac{\sin(\gamma)}{\sin(\alpha)} \quad (1.3.6a)$$

$$E_{\text{in}}^{\perp} + E_{\text{re}}^{\perp} = E_{\text{tr}}^{\perp} \quad (1.3.6b)$$

$$E_{\text{in}}^{\perp} - E_{\text{re}}^{\perp} = n E_{\text{tr}}^{\perp} \frac{\sin(\gamma)}{\sin(\alpha)} \quad (1.3.6c)$$

$$E_{\text{in}}^{\parallel} + E_{\text{re}}^{\parallel} = n E_{\text{tr}}^{\parallel} \quad (1.3.6d)$$

These equations can be resolved to the quotients

$$r^{\parallel}(\alpha, \gamma) = \frac{E_{\text{re}}^{\parallel}}{E_{\text{in}}^{\parallel}} = \frac{n \sin(\alpha) - \sin(\gamma)}{n \sin(\alpha) + \sin(\gamma)} \quad (1.3.7a)$$

$$r^{\perp}(\alpha, \gamma) = \frac{E_{\text{re}}^{\perp}}{E_{\text{in}}^{\perp}} = \frac{\sin(\alpha) - n \sin(\gamma)}{\sin(\alpha) + n \sin(\gamma)} \quad (1.3.7b)$$

$$t^{\parallel}(\alpha, \gamma) = \frac{E_{\text{tr}}^{\parallel}}{E_{\text{in}}^{\parallel}} = \frac{2 \sin(\alpha)}{n \sin(\alpha) + \sin(\gamma)} \quad (1.3.7c)$$

$$t^{\perp}(\alpha, \gamma) = \frac{E_{\text{tr}}^{\perp}}{E_{\text{in}}^{\perp}} = \frac{2 \sin(\alpha)}{\sin(\alpha) + n \sin(\gamma)} \quad (1.3.7d)$$

By using Snell's law, the angle  $\gamma$  can be eliminated from the equations.

$$r^{\parallel}(\alpha) = \frac{n^2 \sin(\alpha) - \sqrt{n^2 - \cos^2(\alpha)}}{n^2 \sin(\alpha) + \sqrt{n^2 - \cos^2(\alpha)}} \quad (1.3.8a)$$

$$r^{\perp}(\alpha) = \frac{\sin(\alpha) - \sqrt{n^2 - \cos^2(\alpha)}}{\sin(\alpha) + \sqrt{n^2 - \cos^2(\alpha)}} \quad (1.3.8b)$$

$$t^{\parallel}(\alpha) = \frac{2n \sin(\alpha)}{n^2 \sin(\alpha) + \sqrt{n^2 - \cos^2(\alpha)}} \quad (1.3.8c)$$

$$t^{\perp}(\alpha) = \frac{2 \sin(\alpha)}{\sin(\alpha) + \sqrt{n^2 - \cos^2(\alpha)}} \quad (1.3.8d)$$

These are the well known Fresnel formulae that Augustin-Jean Fresnel derived from his elastic light theory already in 1821.

Since  $n$  is very close to unity for x-rays, the difference between the parallel and perpendicular case is absolutely negligible. For small angles as they occur in x-ray reflectometry, additional simplifications can be made. Using  $n^2 \approx 1 - 2\delta + 2i\beta$  and  $\cos^2(\alpha) \approx 1 - \alpha^2$  for small angles, the reflective coefficient becomes (the orientational index will be omitted henceforth)

$$r(\alpha) = \frac{\alpha - \sqrt{\alpha^2 - 2\delta + 2i\beta}}{\alpha + \sqrt{\alpha^2 - 2\delta + 2i\beta}} \quad (1.3.9)$$

The reflectivity  $R(\alpha)$ , i.e. the ratio of reflected to impinging intensity, is given by

$$R(\alpha) = r(\alpha)r^*(\alpha) = \left| \frac{\alpha - \sqrt{\alpha^2 - 2\delta + 2i\beta}}{\alpha + \sqrt{\alpha^2 - 2\delta + 2i\beta}} \right|^2 \quad (1.3.10)$$

For angles larger than  $\alpha_i \gtrsim 3\alpha_c$ , the reflectivity behaves like

$$R = \frac{\alpha_c^4}{16\alpha^4} \quad (1.3.11)$$

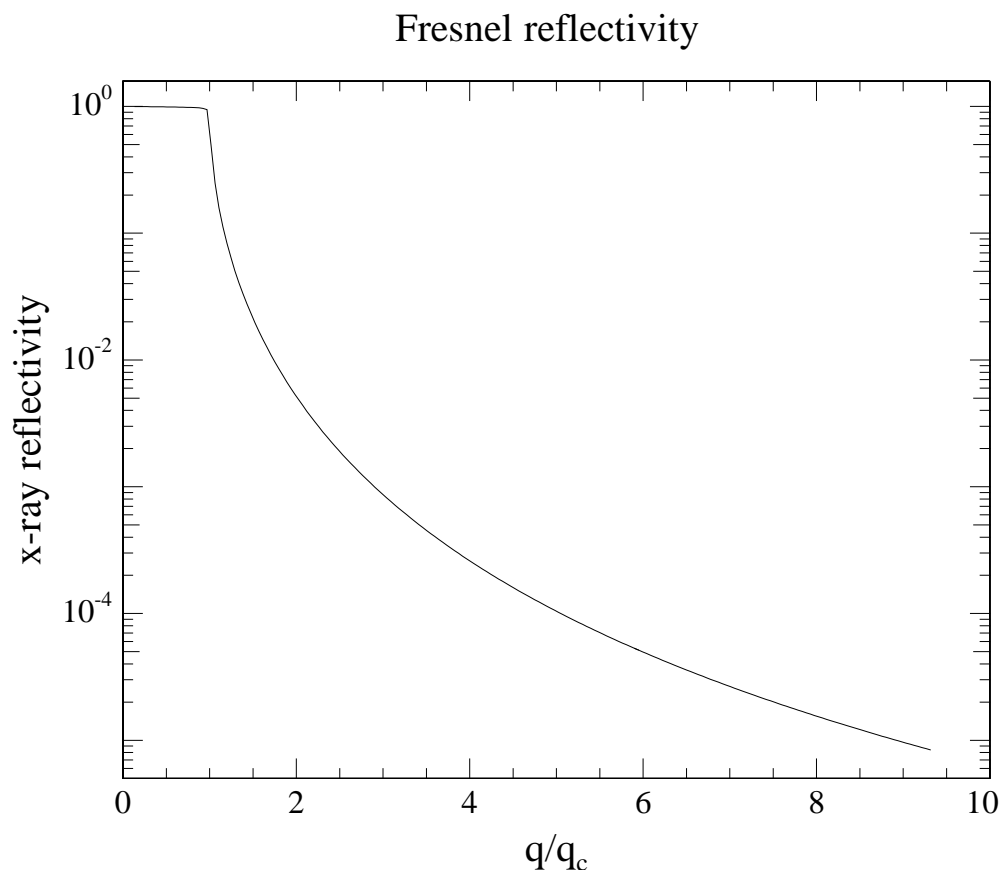


**Figure 1.2:** Logarithmic plot of the reflectivity of x-rays from a simple flat interface. The absorption parameter  $\beta$  primarily influences the shape of the reflectivity in the region of the critical angle by “beveling” the edge.

while there is a far steeper drop beyond the plateau that comprises the region below the critical angle of total reflection.

## 1.4 Structured Surfaces - Parratt Method

Introducing a vertical structuring to the surface causes a modulation of the Fresnel reflectivity which is basically proportional to the Fourier transform of the derivative of the electron density profile. Having a layer of finite thickness on top of the (infinitely thick<sup>1</sup>) substrate just establishes another interface that scatters the impinging photons in the same manner as the first one which leads to interferences.

<sup>1</sup>“infinitely thick” means much larger than the penetration depth of the x-rays which is usually on the order of a few micrometer to a few millimeters which ensures that there is no scattering from the bottom of the substrate.

An elegant way to calculate the reflectivity of a layered system is the so-called Parratt Formalism first described by Parratt in 1954 [4]. I will recapitulate how Metin Tolan handled this topic [5] from here on.

Considering a system of  $N - 1$  stratified layers on a substrate (layer 1 being vacuum or the vapor above the actual sample and layer  $N + 1$  the substrate), the transmitted and reflected wave amplitudes at interface  $j$  between layers  $j$  and  $j + 1$  are called  $T_j$  and  $R_j$  respectively and their ratio is  $X_j = R_j/T_j$ .

$X_j$  can be calculated from  $X_{j+1}$  by

$$X_j = \frac{R_j}{T_j} = e^{-2i\check{k}_j z_j} \frac{r_{j,j+1} + X_{j+1} e^{2i\check{k}_{j+1} z_j}}{1 + r_{j,j+1} X_{j+1} e^{2i\check{k}_{j+1} z_j}}. \quad (1.4.1)$$

Here,

$$r_{j,j+1} = \frac{\check{k}_j - \check{k}_{j+1}}{\check{k}_j + \check{k}_{j+1}} \quad (1.4.2)$$

is the Fresnel coefficient of reflection of interface  $j$  where  $\check{k}_j = k\sqrt{n_j^2 - \cos^2(\alpha_i)}$  is the  $z$ -component of the wave vector in layer  $j$  with refractive index  $n_j$ .

$z_j = \sum_{i=2}^j d_i$  specifies the position of interface  $j$  with  $d_i$  being the thickness of layer  $i$ . The surface of the sample is found at  $z_1 = 0$ .

Since the substrate is assumed to be infinitely thick,  $R_{N+1} = 0 = X_{N+1}$ , as there is no reflection from the bottom of the substrate.

As  $T_1$  is the equivalent to the primary beam,  $T_1 = 1$ , so the total reflectivity

$$R = |X_1|^2 = |R_1|^2 \quad (1.4.3)$$

can be calculated recursively with

$$X_N = e^{-2i\check{k}_N z_N} \frac{r_{N,N+1}}{1 + r_{N,N+1}} \quad (1.4.4)$$

as a start.

Generally,  $R_{j+1}$  and  $T_{j+1}$  can be calculated by

$$R_{j+1} = \frac{1}{t_{j+1,j}} \left( T_j r_{j+1,j} e^{-i(\check{k}_{j+1} + \check{k}_j) z_j} + R_j e^{-i(\check{k}_{j+1} - \check{k}_j) z_j} \right) \quad (1.4.5a)$$

$$T_{j+1} = \frac{1}{t_{j+1,j}} \left( T_j e^{-i(\check{k}_{j+1} - \check{k}_j) z_j} + R_j r_{j+1,j} e^{-i(\check{k}_{j+1} + \check{k}_j) z_j} \right) \quad (1.4.5b)$$

with  $t_{j+1,j} = 1 + r_{j+1,j}$ , the Fresnel coefficient of transmission for interface  $j$ .

## 1.5 Roughness

For x-rays, even a perfect crystalline interface has a relevant roughness. The dents between the atoms present a variation in the electron density distribution that will influence how x-rays are scattered by the interface since their short wave length is on the atomic scale.

In reality, roughnesses are usually even larger. Atomically flat interfaces are an exception to say the least. Organic samples are generally less ordered and consist of larger molecules and even crystals of organic molecules mostly suffer from various defects and impurities.

For liquid samples, thermally induced capillary waves introduce an additional roughness. They will be treated separately in section 1.5.1.

Mathematically, the introduction of a roughness means replacing the interface by an ensemble of interfaces whose position is varied by a probability density  $P_j(z)$ .

Its mean value is

$$\mu_j = \int z P_j(z) dz \quad (1.5.1)$$

and its variance is

$$\sigma_j^2 = \int (z - \mu_j)^2 P_j(z) dz \quad (1.5.2)$$

Averaging  $\exp(-ik(z - \mu_j))$  and equations (1.4.5) with  $P_j(z)$  yields

$$f_j(k) = e^{ik\mu_j} \int e^{-ikz} P_j(z) dz \quad (1.5.3)$$

and

$$R_{j+1} = \frac{1}{\tilde{t}_{j+1,j}} \left( T_j \tilde{r}_{j+1,j} e^{-i(\check{k}_{j+1} + \check{k}_j)z_j} + R_j e^{-i(\check{k}_{j+1} - \check{k}_j)z_j} \right) \quad (1.5.4a)$$

$$T_{j+1} = \frac{1}{f_t \tilde{t}_{j+1,j}} \left( T_j e^{-i(\check{k}_{j+1} - \check{k}_j)z_j} + R_j f_r \tilde{r}_{j+1,j} e^{-i(\check{k}_{j+1} + \check{k}_j)z_j} \right) \quad (1.5.4b)$$

with

$$\tilde{r}_{j+1,j} = \frac{f_j(\check{k}_{j+1} + \check{k}_j)}{f_j(\check{k}_{j+1} - \check{k}_j)} r_{j+1,j} \quad (1.5.5a)$$

$$\tilde{t}_{j+1,j} = \frac{1}{f_j(\check{k}_{j+1} - \check{k}_j)} t_{j+1,j} \quad (1.5.5b)$$

and

$$f_r = \frac{f_j(\check{k}_{j+1} - \check{k}_j)}{f_j(-\check{k}_{j+1} + \check{k}_j)} \frac{f_j(-\check{k}_{j+1} - \check{k}_j)}{f_j(\check{k}_{j+1} + \check{k}_j)} \quad (1.5.6a)$$

$$f_t = \frac{f_j(\check{k}_{j+1} - \check{k}_j)}{f_j(-\check{k}_{j+1} + \check{k}_j)}. \quad (1.5.6b)$$

For real value arguments,  $|f_r| = |f_t| = 1$ . While especially in the region of the critical angle, the imaginary components of the  $\check{k}_j$  can be rather large  $f_r = f_t = 1$  is a good approximation for x-rays.

Assuming an interfacial profile in the form of an error function

$$n_j(z) = \frac{n_j + n_{j+1}}{2} - \frac{n_j - n_{j+1}}{2} \operatorname{erf}\left(\frac{z - z_j}{\sqrt{2}\sigma_j}\right) \quad (1.5.7)$$

with the Gaussian error function

$$\operatorname{erf}(x) = \frac{2}{\sqrt{\pi}} \int_0^x e^{-t^2} dt. \quad (1.5.8)$$

the probability density

$$P_j(z) = \frac{1}{\sqrt{2\pi}\sigma_j} e^{-\frac{1}{2}\frac{z^2}{\sigma_j^2}} \quad (1.5.9)$$

takes the form of a Gaussian distribution. Thus the modified Fresnel coefficients become

$$\tilde{r}_{j+1,j} = r_{j+1,j} e^{2\check{k}_j \check{k}_{j+1} \sigma_j^2} \quad (1.5.10a)$$

$$\tilde{t}_{j+1,j} = t_{j+1,j} e^{\frac{(\check{k}_j - \check{k}_{j+1})^2 \sigma_j^2}{2}} \quad (1.5.10b)$$

For a simple interface that is only modified by roughness, the reflectivity thus takes the form

$$R(q_z) = R_F(q_z) \exp(-q_z^2 \sigma^2) \quad (1.5.11)$$

with an additional damping of the signal by a term similar to a Debye-Waller factor.

### 1.5.1 Capillary Waves

As described in detail by Alan Braslau *et al.* [6], the influence of thermally induced capillary waves on the surficial roughness of a liquid, and thus its x-ray reflectivity, is highly non-negligible.

There are two parts to the energy density  $U$  of surface waves. One stems from the liquid surface tensions and the other is of gravitational origin:

$$U = \frac{\gamma}{2} \int d^2\vec{r}_{xy} |\nabla h(\vec{r}_{xy})|^2 + \frac{\rho g}{2} \int d^2\vec{r}_{xy} h(\vec{r}_{xy})^2 \quad (1.5.12)$$

Here,  $\gamma$  is the liquid's surface tension and  $\rho$  is its density and  $g$  is the gravitational acceleration.

$$\vec{h}(\vec{r}_{xy}) = \frac{1}{2\pi} \int d^2\vec{Q}_{xy} \tilde{h}(\vec{Q}_{xy}) e^{i\vec{Q}_{xy}\cdot\vec{r}_{xy}} \quad (1.5.13)$$

(defined here via its Fourier transform) is the vertical elongation from the mean surface height at position  $\vec{r}_{xy}$ .

With this definition,  $U$  can also be written as

$$U = \frac{1}{2} \int d^2\vec{Q}_{xy} (\gamma|\vec{Q}_{xy}|^2 + \rho g) \tilde{h}(\vec{Q}_{xy})^2. \quad (1.5.14)$$

Applying the equipartition theorem yields

$$\langle h(0)^2 \rangle = \frac{k_B T}{4\pi^2 \gamma} \int d^2\vec{Q}_{xy} \frac{1}{|\vec{Q}_{xy}|^2 + k_g^2} \quad (1.5.15)$$

with  $k_g^2 = \rho g / \gamma$ .  $-\vec{r}_{xy} = 0$  is specifically addressed here, since the mean value has to be invariant with regard to translations.

The upper cut-off for this integral is  $\pi/r_M$  where  $r_M$  is the molecular radius of the liquid in question. The lower edge is given by the resolution of the instrument, since the gravitational limit  $k_g$  is usually beyond that.

It can be shown [6] that because of resolutional restrictions, the rms-roughness due to capillary waves obtained through x-ray reflectivity is

$$\langle h(0)^2 \rangle(q_z) \approx \frac{k_B T}{2\pi\gamma} \ln \left( \frac{k_{\max}}{2k_y} \right) = \frac{k_B T}{2\pi\gamma} \ln \left( \frac{2\pi}{r_M q_z \Delta\beta} \right) \quad (1.5.16)$$

with  $2k_y = k\alpha\Delta\beta$  and  $\Delta\beta = h_d/L$  where  $h_d$  is the height of the active area of the detector and  $L$  is the distance between sample and detector.

Additionally, a static roughness intrinsic to the liquid/vapor interface will be measured. The roughnesses add quadratically

$$\sigma_t^2(q_z) \approx \sigma_p^2 + \sigma_c^2(q_z) \quad (1.5.17)$$

and  $\sigma_t$  will be the total roughness actually measured in an x-ray reflectivity experiment.

# 2 Experimental Setup

## 2.1 Incident Side

### 2.1.1 X-Ray Source

Responsible for generating the x-rays is a 2.2kW copper anode from SEIFERT *Analytical X-ray* powered by a SEIFERT *Iso Debyeflex 3000* stabilized high voltage generator. The focus on the anode is 12mm in width and 4mm in height. Since the take off angle on the anode is  $6^\circ$  the projection of the spot in direction of the sample is  $\sin(6^\circ) \cdot 4\text{mm} \approx 0.4\text{mm}$  high. X-ray reflectometry primarily requires the beam to be narrow and collimated in the vertical direction while the horizontal extent is secondary and mostly limited by sample size and homogeneity. Especially in the region of the critical angle, it is crucial to have a vertically very constrained beam, since the footprint of the beam on the sample surface is enlarged tremendously because of the low grazing angle of incidence as depicted in figure 2.1. E.g. for an incident angle of  $0.1^\circ$ , the footprint on the sample is about 600 times the beam height.

### 2.1.2 Multilayer Mirror

The multilayer mirror is responsible for monochromatizing and collimating the originally white x-ray beam. It is composed of alternating layers of carbon and nickel with a thickness of approximately 2 nm.

One of the most challenging aspects of manufacturing a multilayer mirror is controlling the gradient in the layer thicknesses [7]. Since the incident angle of the x-rays on the mirror varies between  $\theta_1$  and  $\theta_2$  (cf. figure 2.2), maintaining the Bragg condition

$$n\lambda = 2d\sin(\theta) \tag{2.1.1}$$

requires the layer thicknesses  $d$  to increase inverse proportionally to  $\sin(\theta) \approx \theta$ . The Bragg angle corresponding to the copper  $K_\alpha$ -line ( $\lambda = 1.541 \text{ \AA}$ ) is about  $2^\circ$ . Figure C.2 shows a scan through the profile of the primary beam.

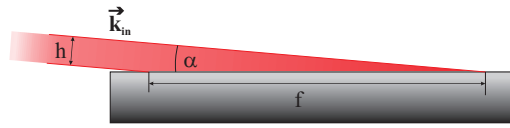


**Figure 2.1:** Illustration of the footprint effect of the low grazing angle of incidence  $\alpha$  of the x-ray beam  $\vec{k}_{in}$  on the sample. In the case illustrated here,  $\alpha = 5^\circ$  - which is actually already quite large - the footprint size  $f$  measures more than ten times the beam height  $h$ .

## 2.2 Sample

Over the course of this work, two different sample containers were used (see figure 2.4).

The first one is a Langmuir trough (MicroTroughX from Kibron Inc. - see figure C.4 in appendix C for a photo) for holding, controlling and manipulating surface films on a liquid substrate (in most cases: water). The trough is basically a rectangular metal ( $6 \times 23 \text{ cm}^2$ ) plate with a polytetrafluoroethylene (PTFE/Teflon) rim on its outer edges. A PMMA-cover with two Kapton windows protects the sample from contamination by aerosols and the like as well as from evaporation.

A set of two barriers consisting of a hydrophilic polymer (Delrin) and driven by a high precision linear motor controls the surface area of the sample and thus its surface pressure and structure. A proprietary program controls the trough and also constantly records the signal of a temperature probe and the surface pressure that is measured by means of a Wilhelmy wire.

Optionally, an external thermostated water flow can be used to additionally regulate the trough temperature.

The second one was a sealed aluminum cell constructed by our in-house workshop (figure C.5 in appendix C contains a photo). It has Kapton windows on either side, a connector to attach a gas distribution system and a temperature control consisting of a heating foil counteracting a Peltier element.

The Peltier element's hot side is cooled by a constant flow of water. Inside, a small ( $2 \times 9 \text{ cm}$ ) removable (to allow for convenient and thorough cleaning) PTFE trough, supported by an aluminum plate for increased structural stiffness, is used to hold the sample.

One side has a feedthrough for a Pt-100 temperature probe.

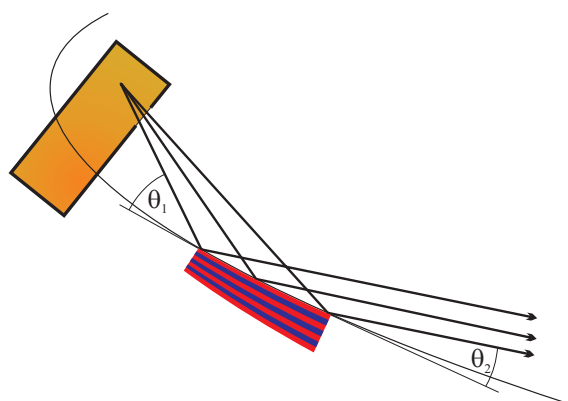


**Figure 2.2:** *The focal points of the anode and of the parabolic mirror coincide. The layer thicknesses increase continuously with distance from the source to maintain the Bragg condition.*

## 2.3 Detector side

Any stray scattered photons from the air surrounding the sample or any of the windows are filtered by an aperture at the entrance of the detector tube. Another pair of slits in front of the detector determines its angular acceptance range.

The detector itself is a proportional counter. A pulse shaper, discriminator and counter deliver the photon count to the computer.

## 2.4 Alignment

The reflectometer is entirely controlled by stepper motors.

The incident angle is tuned by rotating the primary side circle positioner (cf. figure 2.3 and also figure C.3 in appendix C for a real life picture) that controls the inclination of the incident tube - with a precision of  $1/3600^\circ$  - which has the anode together with the multilayer mirror on the far end.

On the other end, facing the sample, is a pair of horizontal and vertical slits (aperture and position adjustable by  $1/1250\text{mm}$ ) to shape the beam as well as an attenuator that limits the beam intensity in three stages, each dampening the primary intensity by a factor of approximately 7.5 (cf. figure C.1). This is mostly necessary for very low incident angles in the region of total reflection and slightly beyond, where the reflected intensity of the full direct beam would be at least high enough to push the detector beyond the limits of its dead time or could even be harmful.

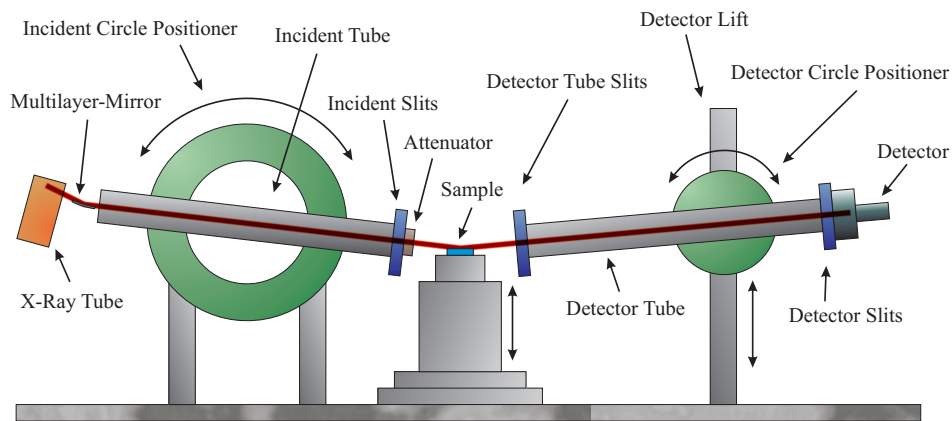


**Figure 2.3:** The red line indicates the x-ray beam path.

The sample's vertical position is adjusted by a stage with a precision of  $1/80$  mm for its surface to intersect with the beam path. For non-liquid samples, a horizontal arrangement of the sample has to be assured as well, which can be done by means of an Eulerian cradle. A liquid interface has the advantage of doing that by itself.

The entire detector tube is positioned so that the specularly reflected beam exactly hits the detector (precision:  $1/400^\circ$ ). Both the incident and detector tubes are evacuated, with the ends closed off by Kapton windows, to prevent absorption of the photons by air molecules. Considering the distance the photons have to travel in the entire setup, ignoring this influence would reduce the available intensity by a factor of about four to five.

The sample and the detector arm can also be rotated around a common vertical axis which would basically make it feasible for ordinary wide angle x-ray scattering. But since the horizontal orientation of the line focus diminishes the resolution in this direction to a large extent and a reorientation of the focus is at the least very time consuming, this degree of freedom is generally only used to record the background scattering from the subphase bulk, which is superimposed on the specular signal and has to be eliminated from the total number of photon counts.

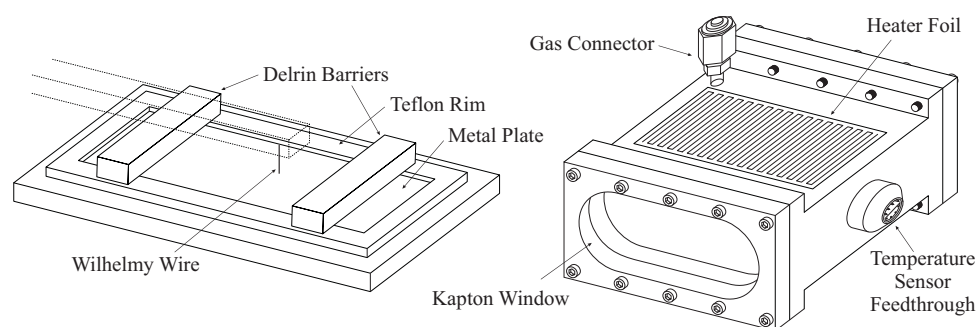


**Figure 2.4:** *The two different sample holders*  
Left: *The Langmuir Trough.* Right: *The in-house built sealed cell.*

## 2.5 Control

As previously mentioned, the whole reflectometer is controlled by stepper motors - 15, to be precise (for a complete list cf. appendix section A.3). These, in turn, are handled by a total of four stepper motor controllers. Although different interfaces are used (RS232 and GPIB) everything is conducted under a unified interface in a command line based program named “X-Surf” written in Borland Delphi™. A screenshot and a list of all commands are given in appendix A.

One of the software’s most convenient features is its ability to process macro files with an arbitrary number of commands which allows for long unattended series of measurements. It is also very easily extensible to support additional hardware just by editing a simple configuration file.

A temperature controller and the counting chain for the x-ray photons are also addressed via “X-Surf”. It has proven to be very advantageous to be able to control every aspect of the setup under a single consolidated interface.

To keep a record of everything that happens, the program generates a log-file that contains every in- and output made during a session. A variety of specifically written PERL-scripts and GENPLOT-macros takes care of data extraction and processing from these logs.



# 3 Proof of Concept: Characterization of Hydrophobized Si-Wafers

As a preliminary work, the analysis of a simple system of silicon wafers coated with a self assembled monolayer (SAM) of octadecyltrichlorosilane and dodecyltrichlorosilane was performed. The samples were provided by Hendrik Hähl, research group of Karin Jacobs at Saarland University.

## 3.1 Sample Composition

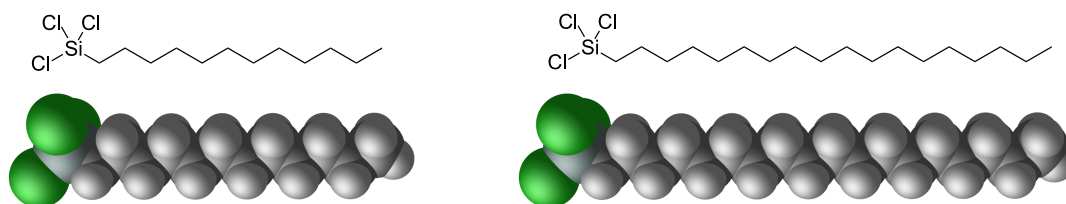


*Figure 3.1: Structure of DTS (left) and OTS (right)*

The sample has a very clear vertical structure. The substrate is the silicon itself. On top of that is a thin (about 1 nm) silicon dioxide layer that naturally manifests when exposed to air.

The coating itself can be broken down into two layers for *DTS* and *OTS* respectively: The alkyl chain which is in direct contact to the air above the sample and the trichlorosilane headgroup, whose chlorine is removed through hydrolysis during the attachment to the  $SiO_2$  layer [8–10].

While this structure is quite accessible to analysis through the Parratt method (cf. section 1.4) as it is very distinctly separable into clearly defined layers and has a rather strongly scattering substrate, it is still sufficiently complex and delicate to provide an adequate test for a newly constructed instrument.

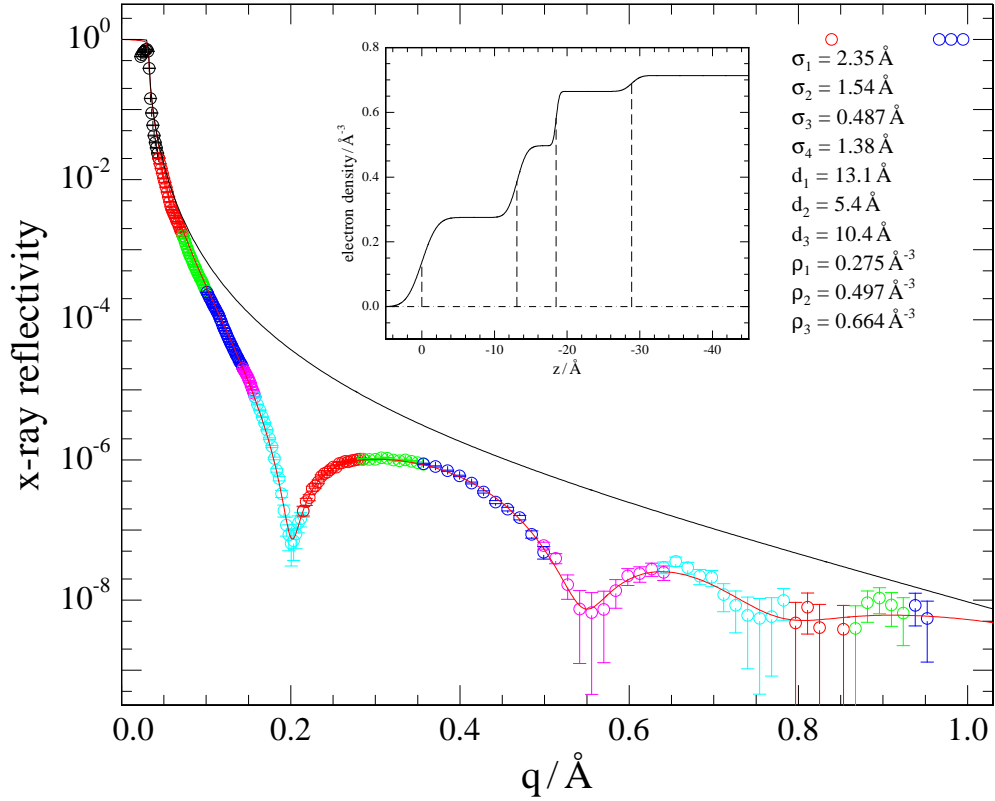


**Figure 3.2:** Reflectivity of DTS on silicon. The solid black line is the Fresnel reflectivity of silicon for comparison. The different colors represent different blocks of the measurement with varying attenuator settings.

## 3.2 Measurements

For the measurements, the samples were placed under a simple Kapton cover to protect them from aerosols. The data presented in figure 3.2 for DTS and 3.3 for OTS were fitted to a three layer electron density profile with the Parratt method using Genplot. The transition between each of the layers as well as to the substrate was smoothed with an error profile.

The three boxes can be identified (from top to bottom) as the alkyl chain, the silane head group and the native oxide layer. The data found by the fitting process is presented in the respective figures mentioned above.  $d_i$  and  $\rho_i$  correspond to the  $i$ -th layer and  $\sigma_i$  refers to the transition between layer  $i - 1$  and layer  $i$ .

Each of these measurements took about 16 hours in total.

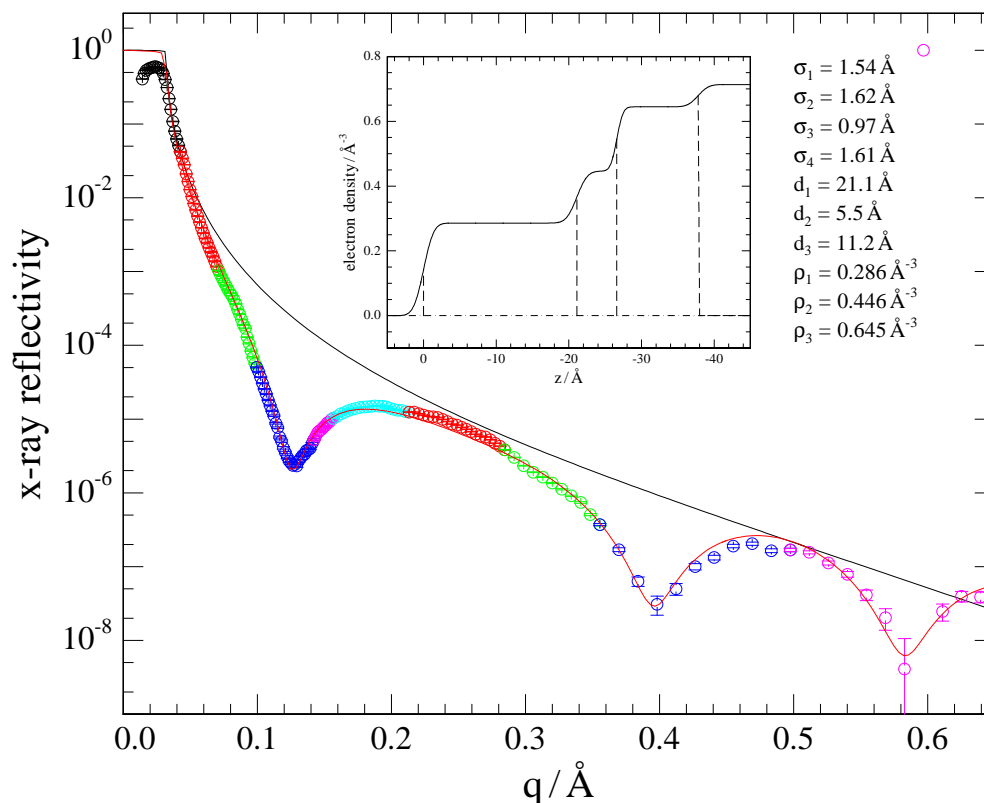


**Figure 3.3:** Reflectivity of OTS on silicon. The solid black line is again the Fresnel reflectivity of silicon for comparison.

### 3.3 Conclusions

The only significant difference between the two obtained profiles is the thickness of the alkyl layer  $d_1$ . - As is to be expected.

However, the values are smaller than is to be anticipated for a fully extended linear dodecyl and octadecyl chain respectively.

There are two possible explanations for this result: Either the chains display kink defects or they are slanted relative to the surface normal.

Since the electron densities of the alkyl layers obtained through the analysis are even slightly higher than those of the respective bulk alkanes, the slant-explanation is far more likely. - Apart from the fact that being fully extended is the energetically most accommodating conformation. Assuming the alky chains to be fully extended, they have to be tilted from the surface normal by  $34^\circ$  for DTS and  $25^\circ$  for OTS to match the measured layer strengths.

A. Seeboth and W. Hettrich [11] reported on different silanes (octadecyltrichlorosilane (OTS), octadecyltrimethoxysilane (OMS), 3-chloropropyltrichlorosilane (CPTS) and hex-1-enyltrichlorosilane (HETS)) attached to a glass surface which

they inspected using conoscopic microscopy. For OTS and low concentrations of the initial solution, they found tilt angles of up to  $22^\circ$ .

## Part II

# Constitutive

The research from the liquid samples (Langmuir films of amphiphilic diblock copolymers and gold nanoparticle suspensions) investigated during this work is presented in the following.



# 4 Langmuir Films of Amphiphilic Diblock Copolymers

The work presented in this chapter has also been previously published [12]. The structure of Langmuir films of amphiphilic di-block co-polymers (hydrophilic poly(ethylene oxide) (PEO) tail and hydrophobic poly(heptafluorobutyl methacrylate) (PHFBMA) head), provided by Karsten Busse, University of Halle-Wittenberg, was investigated by x-ray reflectometry for different surface pressures. The points on the compression isotherm, where the reflectivities were recorded are marked by crosses in figure 4.2. The isotherms were also recorded at Halle-Wittenberg in a KSV ltd. (Helsinki, Finland) Teflon Langmuir trough similar to the one presented in section 2.2.

## 4.1 Amphiphilic Polymers

Interfacial properties of amphiphilic block copolymers have a large influence on the properties of polymer blends and they also play an important role in the understanding of polymers in confined geometries [13–19]. There are a lot of potential applications, such as biological membranes [20, 21] or colloidal stabilization [22, 23]. Additionally, one fundamental property of amphiphilic block copolymers is their self-assembly in selective solvents. The morphology of the resulting structures depends mainly on the hydrophilic-lipophilic balance and the concentration [24].

The molecular behavior of amphiphilic block copolymers at the air-water interface has been the focus of many investigations [2, 5, 25–40]. X-ray and neutron reflectivity measurements (XRR and NR) and surface pressure vs mean molecular area ( $\pi$ -mMA) isothermal Langmuir trough experiments are very useful techniques to study the developing surface structure at the air-water interface. In general, the hydrophilic blocks are dissolved in the water phase, or at least, as in the case of poly(ethylene oxide) (PEO), adsorbed at low surface pressure at the interface, and the hydrophobic part is directed toward the air phase. With increasing compression, a stretched conformation (brush) of the hydrophilic block in the subphase is formed, due to anchoring by the hydrophobic block. For amphiphilic block copolymers containing a PEO block, a pancake to brush transition usually can

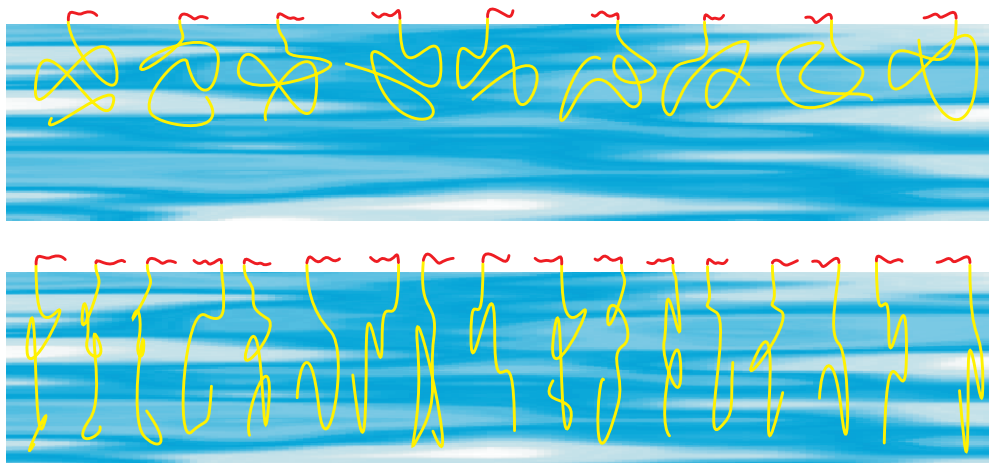


**Figure 4.1:** Sketches of the mushroom (top) and brush (bottom) phases of the PEO (yellow) polymer part. In the mushroom phase, one end of the PEO chain is pinned to the surface via the PHBFMA block (red) while the rest forms a coil below the surface. In the brush phase, due to a reduced mean molecular area ( $mmA$ ), the chain is nearly fully extended and assumes a linear conformation.

be observed at a surface pressure of  $\sim 9$  mN/m. This transition is not detectable when the length of PEO is too small compared to the hydrophobic block [28, 29].

Amphiphilic copolymers with some short hydrophobic end groups [41, 42] (such as telechelic polymers) or with lipid head groups [43–45] (such as lipopolymers) are able to form 2D micelles on the water surface, also depending on their composition [46]. Surface micelle formation and aggregation at the air-water interface were observed, e.g., for poly(ethylene oxide)-*b*-poly-(styrene) (PEO-*b*-PS) [35, 36] linear diblock copolymers, indicated by a phase transition at high surface pressure. Additionally, at high surface pressure, the hydrophobic chains are forced away from the water surface and generate a reverse U shape [47].

Fluorinated amphiphilic block copolymers are widely known for their large capability to reduce interfacial tension between fluids and their high thermal and chemical stability. A high hydrophobicity has a large effect on the functionality of materials. Several studies are using end-capped polymers [48–50], fluorinated surfactants [51], or fluorinated amphiphilic copolymers with a long fluorinated side chain  $CF_3(CF_2)_{m-1}(CH_2)_n$  [52–55]. It is well-known that the length of the side chains (the number  $m$ ) has a tremendous influence on the properties of the fluorinated polymers. Perfluoro- and semifluoro-alkyl groups  $CF_3(CF_2)_{m-1}(CH_2)_n$  with  $m \geq 8$  are known as nanoscale rigid rod-like molecules, with a helical conformation, capable of forming a liquid crystalline phase [56]. Maekawa et al. [57] reported that the surface structure of fluoroalkyl acrylate homopolymers with short side chains changes when they are brought into contact with water. They

concluded that the surficial reorientation in contact with water takes place when  $m$  is smaller than 8, where the polymers are non-crystalline.

The original publication [12] is based on the fluorinated and nonfluorinated amphiphilic copolymers poly(ethylene oxide)-*b*-poly(heptafluorobutyl methacrylate) (PEO-*b*-PHFBMA) and poly(ethylene oxide)-*b*-poly(*n*-butyl methacrylate) (PEO-*b*-PBMA) using an identical hydrophilic block and similar structures of hydrophobic blocks. However, due to the fluorine in the side chains, the PHFBMA block is more hydrophobic and exhibits a stronger electron density contrast towards the aqueous subphase than the corresponding PBMA block. Among various types of hydrophobic groups, perfluorinated carbon chains are most hydrophobic and their tendency to separate from water or hydrophilic groups is the largest [24]. A rule of thumb for the hydrophobicity of fluorinated blocks is that one  $\text{CF}_2$  group is equivalent to 1.7  $\text{CH}_2$  groups [58].

## 4.2 Polymer Synthesis

Polymerization was achieved through atom transfer radical polymerization (ATRP) with PEO-Br as macroinitiator [59, 60]. This process yields copolymers with low polydispersity, terminal functionalities and defined chain architecture [61, 62] and facilitates the combination of PEO with fluorinated blocks [52, 63]. For details, cf. [12].

Size exclusion chromatography (SEC) calibrated with poly(methyl methacrylate) (PMMA) standards and with THF as the eluent was used to determine the molar mass distribution returning polydispersities of 1.2 for  $\text{PEO}_5\text{F}_3$ ,  $\text{PEO}_5\text{F}_{15}$  and  $\text{PEO}_5\text{F}_{22}$  and 1.1 for  $\text{PEO}_5\text{F}_{64}$ . The molar masses were determined from NMR measurements to be 5.8, 9.0, 10.9 and 22.9 kg/mol respectively.

## 4.3 Compression Isotherms

As mentioned before, the surface compression isotherms shown in figure 4.2 were recorded in Halle on a KSV langmuir trough. The subphase (purified distilled water) was kept at  $22.5 \pm 0.5$  °C during compression. The compression rate was kept at  $5 \text{ cm}^2/\text{min}$ .

For mean molecular area (mmA) values above  $\sim 4000 \text{ \AA}$ , the surface pressure for all polymers remains at  $0 \text{ mN/m}$ , indicating that the molecular chains can move about freely within interfering with one another's mobility. Further decreasing the mmA brings the molecules into contact and causes the surface pressure to rise. For the three smaller polymers, there are two phase transitions starting at  $\sim 9$  and  $20 \text{ mN/m}$  while for  $\text{PEO}_5\text{F}_{64}$  there is only one between  $16$  and  $20 \text{ mN/m}$ .

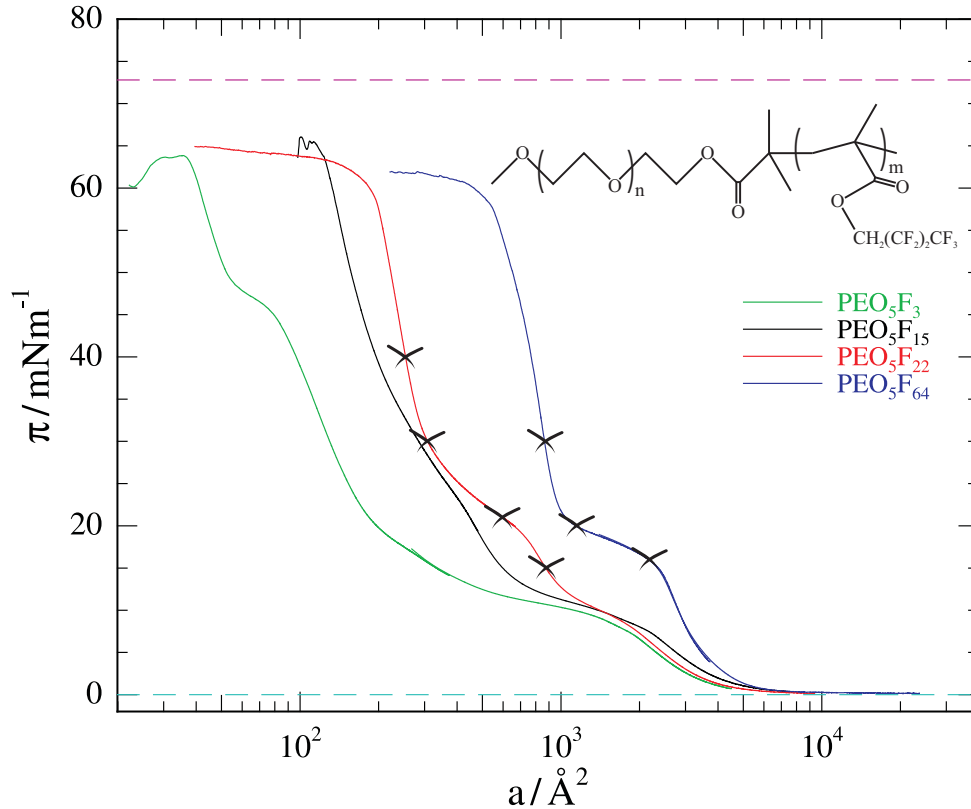


**Figure 4.2:** Compression isotherms of  $PEO_5F_m$  monolayers on an aqueous subphase for four different values of  $m$ . The upper right corner shows the molecular structure with  $n$  and  $m$  the numbers of EO and HFBMA monomers respectively. The crosses signify the points where the reflectivity measurements were taken and the dashed magenta line represents the surface tension of pure water.

The first transition is commonly found for copolymers containing PEO and marks the pancake-to-brush transition ending at the limiting brush area  $A_b$ :  $175 \text{ \AA}^2$ ,  $620 \text{ \AA}^2$  and  $980 \text{ \AA}^2$  from  $PEO_5F_3$  to  $PEO_5F_{22}$ .

The corresponding plateau is suppressed for  $PEO_5F_{64}$  as the hydrophobic part is so large that it completely dominates its behavior [64, 65].

The second transition starts as the  $m$ MA decreases below the area of a PHFBMA block lying flat on the water surface. The transition ends at about  $15 \text{ \AA}^2$  per HFBMA group for all polymers, which could either be a double layer of HFBMA side groups standing upright on the surface with the MA backbone in between (see right panel of figure 4.4) or a folded PHFBMA block with four to five side chains stacked parallel to the surface.

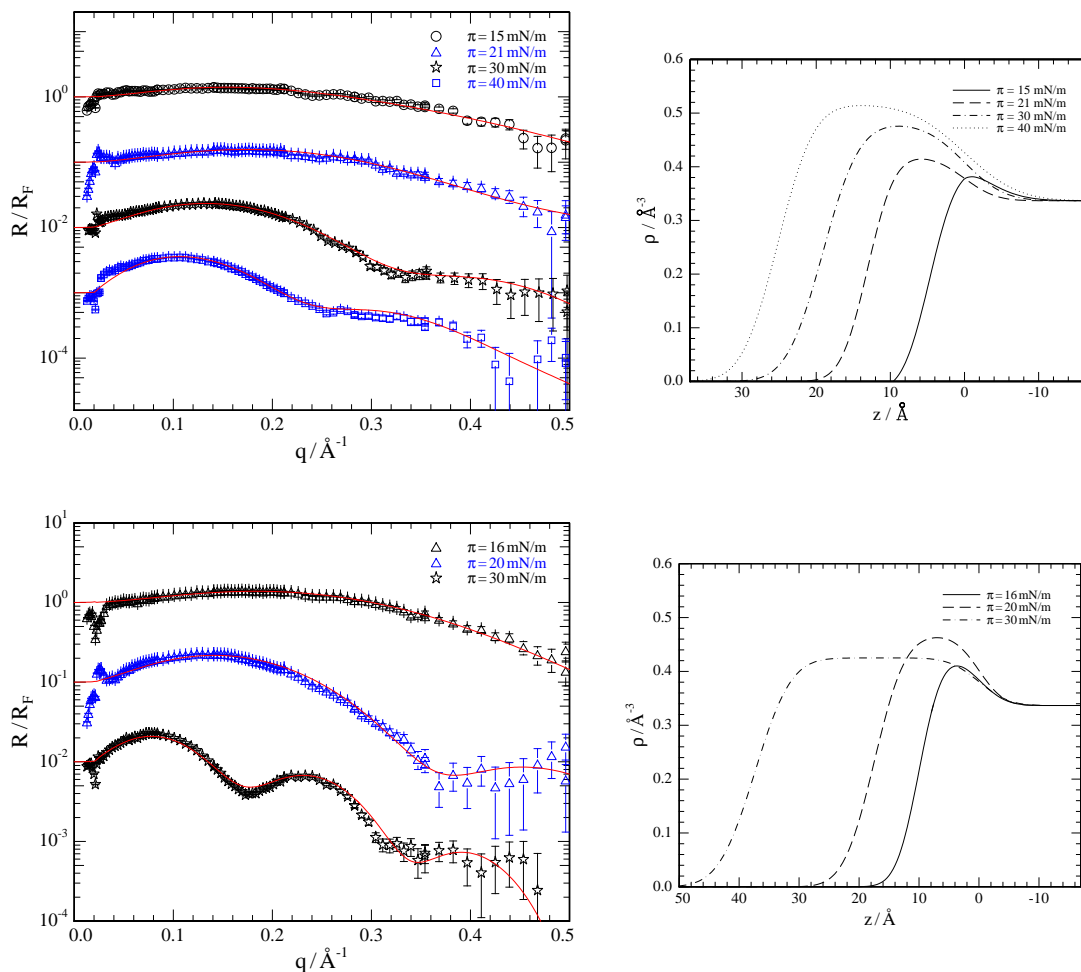


**Figure 4.3:** Reflectivities (left) and corresponding electron density profiles (right) of PEO<sub>5</sub>F<sub>22</sub> (top) and PEO<sub>5</sub>F<sub>64</sub> (bottom) at three different surface pressures.

## 4.4 X-Ray Reflectivity Measurements

To decide which of these two scenarios best describes the system, x-ray reflectivity measurements at different surface pressures (marked by crosses on the isotherms in figure 4.2) were performed for PEO<sub>5</sub>F<sub>22</sub> and PEO<sub>5</sub>F<sub>64</sub> as these two show the most pronounced second phase transition and, with their larger head groups, give the best XRR signal. The obtained reflectivities were Parratt-fitted with a single slab model, which corresponds to the hydrophobic block. The hydrophilic PEO-Block gives virtually no signal since it is contrast matched with the aqueous subphase. The resulting parameters are presented in table 4.1.

Comparing the total number of electrons for a PHFBMA chain as determined from the fit to the experimental data (column  $N_e$  (ex) in table 4.1) to the theoretical number of electrons as calculated from the polymer composition is a simple

	surface pressure $\pi$ (mN/m)	thickness $d$ (Å)	electron density $\rho$ (Å <sup>-3</sup> )	roughness $\sigma_1$ (Å)	roughness $\sigma_2$ (Å)	mmA (Å <sup>2</sup> )	$N_e$ (ex)	$N_e$ (th)
PEO <sub>5</sub> F <sub>22</sub>	15	4.66	0.478	3.03	10.19	875	1949	2948
	21	13.07	0.420	2.84	3.37	571	3047	2948
	30	19.11	0.480	3.86	4.22	310	2898	2948
	40	25.17	0.516	3.81	5.71	252	3130	2948
PEO <sub>5</sub> F <sub>64</sub>	16	9.99	0.432	3.02	3.49	2016	8674	8576
	20	17.44	0.467	4.05	3.26	1100	8959	8576
	30	37.39	0.425	4.75	3.96	750	11918	8576

**Table 4.1:** Parameters of a single slab model as determined from x-ray reflectivity measurements of PEO<sub>5</sub>F<sub>22</sub> and PEO<sub>5</sub>F<sub>64</sub>.

$N_e(ex)$ , number of electrons in the hydrophobic part per chain from experiment.

$N_e(th)$ , theoretical number of electrons in the hydrophobic part per chain.

check for consistency of the electron density profiles.

The measurements were performed with the Kibron Langmuir trough mentioned in section 2.2 with ultrapure water (Milli-Q<sup>®</sup>, Millipore, USA) as the subphase.

#### 4.4.1 PEO<sub>5</sub>F<sub>22</sub>

At 15 mN/m, the thickness of the PHFBMA layer was determined to be 4.7 Å. This value corresponds well to the diameter of the HFBMA side chains (cf. figure 4.4), which suggests that there are only flat lying PHFBMA chains present on the surface. However, the obtained interfacial roughness as presented in table 4.1 is unrealistically large. Also the number of electrons deviates from the theoretical value by about one third. The signal seems to be too weak to allow for a rigorous analysis.

At 21, 30 and 40 mN/m, at the beginning, the end and quite beyond the second phase transition, the electron counts agree quite well with the predicted values.

As mentioned before, there are two possible conformations for the PHFBMA head groups to assume. In the case of double layer of HFBMA side chains arranged perpendicular to the subphase surface, a section of reduced electron density should be present at half height where the non-fluorinated backbone is located. None of the reflectivities seem to show a feature that hints towards this scenario. However, the difference in electron density might be too small and fluctuations in the vertical position (due to capillary waves for example) might completely blur the backbone into the side chains as the reflectivity averages over the whole illumi-

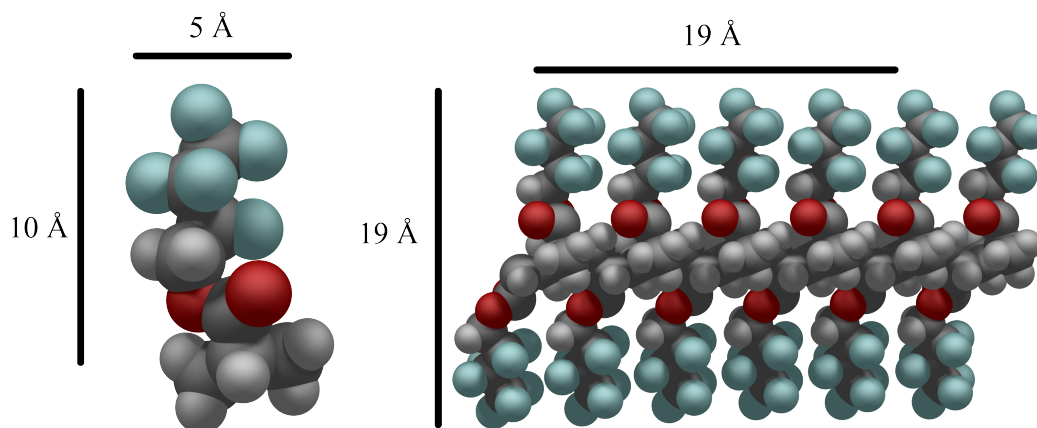


**Figure 4.4:** Left: The chemical structure of a single HFBMA monomer unit. Right: A densely packed section of the PHFBMA head group forming a double layer of HFBMA side chains. The size bars show that the thickness of the double layer corresponds to the thickness of a stack of four side chains.

nated area. The second scenario requires the side chains to be stacked parallelly to the surface. The layer thickness of  $25.17\text{ \AA}$  at  $40\text{ mN/m}$  corresponds to a staple of approximately 5 layers.

#### 4.4.2 $PEO_5F_{64}$

Reflectivities for  $PEO_5F_{64}$  were recorded at 16, 20 and  $30\text{ mN/m}$ , at the beginning, the end and beyond the second phase transition.

For  $16\text{ mN/m}$ , the PHFBMA layer thickness was determined to be  $10\text{ \AA}$ . This value could either mean that there is a monolayer of HFBMA side chains arranged perpendicular to the liquid's surface or there is a bilayer of side chains oriented parallelly to the surface. At  $20\text{ mN/m}$ , the reflectivity yields a layer thickness of  $17.4\text{ \AA}$ . This is less than a double layer of vertically oriented side chains, hinting to a slight tilt of the chains. Also, this value is just between what is to be expected for a three or four side chains staple.

At  $30\text{ mN/m}$  the electron number as determined from the fit exceeds the theoretical value by more than one third. The layer thickness of  $37.4\text{ \AA}$  corresponds to a quadruple layer of vertically oriented side chains or a stack of seven to eight lying ones.

## 4.5 Conclusion

While the findings from the x-ray reflectometries are not perfectly conclusive, there are quite some indications that hint to a horizontal arrangement of the side chains.

For once, there is the absence of any signs of a region of reduced electron density at half height in the PEO<sub>5</sub>F<sub>22</sub> at 30 mN/m and PEO<sub>5</sub>F<sub>64</sub> at 20 mN/m reflectivities, where the layer thickness matches the height of a double layer of standing side chains - despite the concerns mentioned in section 4.4.1.

Second, the layer thickness for PEO<sub>5</sub>F<sub>22</sub> at 40 mN/m and PEO<sub>5</sub>F<sub>64</sub> at 30 mN/m exceed the height of a double layer, in the second case by a factor of two. This is easier explained by a staple of lying side chains than by some obscure arrangement of stacked double layers of standing chains.

# 5 Surface Layering of Suspended Au-Nanoparticles

The system presented in this chapter is a suspension of gold nanoparticles in toluene. Dodecanethiol ligands are attached to the cores for steric stabilization. The gold core of a nanoparticle is 6nm in diameter. The 1.5nm ligand shell extends this value to 9nm. They were synthesized from AuPPh<sub>3</sub>Cl and dodecanethiol in a benzene solution according to the recipe in reference [66] in the research group of Dr. Tobias Kraus (Leibniz Institute for New Materials, Saarbrücken). This technique combines achieving a very low polydispersity (< 5%) with a reasonable yield of nanoparticles.

## 5.1 Nanoparticle Suspensions

Nanoparticle suspensions and surface films have been the subject of many studies to date. There are many applications for integrated optical devices and surface treatments.

For example, Tao *et al.* [67] examined the coupling of two dimensional silver nanoparticle arrays to external electromagnetic fields. By controlling the interparticle spacing via Langmuir-Blodgett technique, the optical response can be finely tuned.

Structural disorders can have a tremendous impact on the electronic transport in nanoparticle monolayers as was investigated by Parthasarathy *et al.* [68]. The current-voltage characteristics show signs of coulomb blockade and quantum tunneling depending on the particle density within the monolayer which has many potential applications in sensors.

Bera *et al.* [69] demonstrated the ability to form a high density Langmuir-Blodgett film of gold nanoparticles by annealing particles undergoing a reversible buckling during their transition from mono- to bilayer arrangement. In a similar study, Schultz *et al.* [70] showed that the reversibility of this process is influenced by excess thiol molecules in the Langmuir layer.

The emergence of nanoparticle self-assembled monolayers on the surface of a drying droplet of nanoparticle suspension was investigated in many studies. Bi-

gioni *et al.* [71] used an evaporating droplet of gold nanoparticles suspended in toluene to deposit a highly ordered extensive monolayer onto a  $\text{Si}_3\text{N}_4$  substrate and observed the process via optical microscopy. The resulting monolayers were analyzed via transmission electron microscopy (TEM). Park *et al.* [72] used liquid cell TEM to directly monitor the assembly of platinum nanoparticles at an evaporating surface while Narayanan *et al.* relied on grazing incidence small angle x-ray scattering (GISAXS) to monitor the formation gold nanoparticle monolayers during droplet evaporation and analyze their structure [73].

Mueggenburg *et al.* [74] deposited a Langmuir layer from a toluene suspension of gold nanoparticles onto a droplet of water. By evaporation of this droplet, a free standing membrane of nanoparticles covering a hole in the substrate was created. In a similar experiment Pang *et al.* [75] created a SAM at the interface between water and toluene. The film was stabilized to a free standing membrane by PMMA in the toluene solution that accumulated with the nanoparticles at the interface. Due to the stabilizing polymer, the resulting membranes were much larger than those of Mueggenburg *et al.* - up to several centimeters as opposed to about one micrometer.

Muralidharan *et al.* [76] investigated the applicability of 2D metal nanoparticle arrays as storage nodes in floating gate devices utilized in non-volatile electronic memories.

A nanoparticle enhanced Marangoni flow was observed by Wi *et al.* [77] in a thin film of an NP-octadecane suspension near its melting point. The effect is assumed to originate in a selective freezing out of nanoparticles which generates a large concentration gradient.

The formation of 3-dimensional superlattices in the bulk of a suspension has been investigated both experimentally [78–81] and theoretically [82, 83].

The adsorption of nanoparticles at liquid vapor interfaces has also been studied theoretically [84] (here for example with a focus on the influence of line tension, cf. the following section for details) and through molecular dynamics simulations [85].

## 5.2 Monolayer Formation

As outlined in reference [84], an interplay between the various interfacial tensions and the line tension of the three phase contact line on a particle at the liquid/vapor interface is the cause for the adsorption of a nanoparticle.

The sketch in figure 5.1 illustrates the geometry of a nanoparticle.  $r_0$  is the radius of the gold core and  $r_1$  is the radius of the particle with the thiol layer. The cap

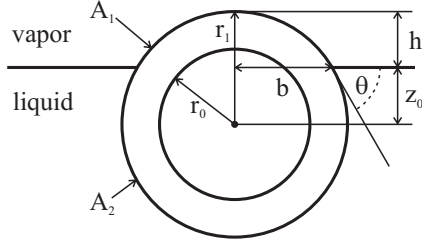


**Figure 5.1:** Sketch of a single, partly submerged nanoparticle at a liquid/vapor interface.

The cap with height  $h$  and area  $A_1$  sticks out of the liquid.

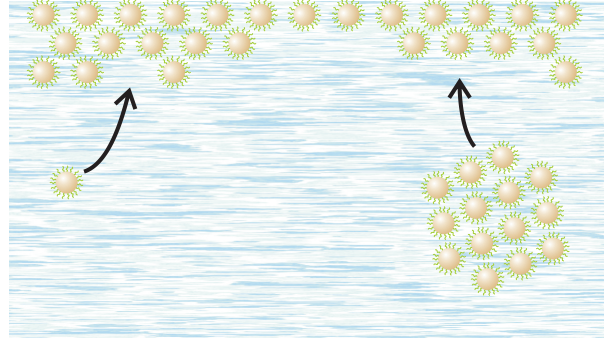


**Figure 5.2:** The two competing mechanisms of surface layer formation.

Left: A single nanoparticle is incorporated into the layered surface film.

Right: An agglomerate having formed in the bulk prior to its surface adsorption is embedded into the surface layers.

with height  $h$  and area

$$A_1 = 2\pi r_1 h \quad (5.2.1)$$

of the spherical particle sticks out of the liquid surface. The base radius of this cap is  $b$ .

Thus, by moving the particle from the bulk to the surface, the liquid vapor surface area

$$A_0 = \pi b^2 \quad (5.2.2)$$

is destroyed.

Also, the solid/vapor interface with area  $A_1$  is created while the solid/liquid interface of the same size is destroyed. The remaining solid/liquid interface area is

$$A_2 = 2\pi r_1 (2r_1 - h). \quad (5.2.3)$$

Thus, the combined interfacial energy of a submerged nanoparticle is

$$E_{\text{subm}} = (A_1 + A_2)\gamma_{\text{sl}} + A_0\gamma_{\text{lv}} \quad (5.2.4)$$

and the total surface energy of an adsorbed particle is

$$E_{\text{ads}} = A_1\gamma_{\text{sv}} + A_2\gamma_{\text{sl}} \quad (5.2.5)$$

with  $\gamma_{\text{sl,lg,sv}}$ , the interfacial tensions between solid (particle) and liquid, liquid and vapor, solid and vapor respectively.

The adsorption of a particle to the liquid's surface also creates the three phase contact line surrounding the particle that has an associated line tension  $\tau$  and thus a corresponding energy which becomes increasingly more relevant the smaller a particle is, since the circumference to surface ratio increases. This energy is

$$E_1 = 2\pi b\tau \quad (5.2.6)$$

and has to be added to the interfacial energy.

$$E'_{\text{ads}} = E_{\text{ads}} + E_1 = A_1\gamma_{\text{sv}} + A_2\gamma_{\text{sl}} + 2\pi b\tau \quad (5.2.7)$$

In total, the difference in energy between a submerged and an adsorbed particle is

$$\Delta E = E'_{\text{ads}} - E_{\text{subm}} = A_1(\gamma_{\text{sv}} - \gamma_{\text{sl}}) - A_0\gamma_{\text{lv}} + 2\pi b\tau. \quad (5.2.8)$$

The lateral organization of nanoparticles at liquid surfaces has been extensively investigated – both theoretically and experimentally – in previous studies [73, 85–88].

Capillary forces are irrelevant to the in-plane interaction of the nanoparticles as gravimetric forces are too small to have any effect [89].

Since the particles do not carry any electrical charge either, the only type of long range interaction relevant to the lateral arrangement remaining is dipole-dipole interactions.

### 5.3 Monolayer Electron Density

Assuming a close packed hexagonal arrangement of nanoparticles as illustrated in figure B.1, the cross-sectional area taken up by a gold core of radius  $r_0$  at height  $z$ , measured from the gold core center, in a unit cell is

$$A_{\text{g}}(z) = \pi b(z)^2, \quad (5.3.1)$$

with  $b = \sqrt{r_0^2 - z^2}$  being the gold core radius at height  $z$ .

If the center-to-center distance of the gold cores is  $a_1$  then the total area of the unit cell is

$$A_1 = \frac{1}{2}\sqrt{3}a_1^2 \quad (5.3.2)$$

and the area covered in toluene is

$$A_{\text{t}}(z) = A_1 - A_{\text{g}}(z). \quad (5.3.3)$$

The total average electron density  $\rho_{\text{tot}}(z)$  of a monolayer thus is

$$\rho_{\text{tot}}(z) = \begin{cases} \rho_{\text{t}} & \text{if } z < -r_0, \\ (A_{\text{t}}(z)\rho_{\text{t}} + A_{\text{g}}(z)\rho_{\text{g}})/A_1 & \text{if } -r_0 < z < z_0, \\ (A_{\text{g}}(z)\rho_{\text{g}} + A'_{\text{th}}\rho'_{\text{th}})/A_1 & \text{if } z_0 < z < r_0, \\ (A''_{\text{th}}(z)\rho''_{\text{th}}(z))/A_1 & \text{if } r_0 < z < r_1, \\ 0 & \text{if } z > r_1. \end{cases} \quad (5.3.4)$$

with

$$\rho'_{\text{th}} = \rho_{\text{th},0} \ln(r_1^2/r_0^2) \frac{r_0^2}{r_1^2 - r_0^2} \quad \text{if } z_0 < z < r_0 \quad (5.3.5a)$$

$$\rho''_{\text{th}}(z) = \rho_{\text{th},0} \ln(r_1^2/z^2) \frac{r_0^2}{r_1^2 - z^2} \quad \text{if } r_0 < z < r_1 \quad (5.3.5b)$$

and

$$A'_{\text{th}} = \pi(r_1^2 - r_0^2) \quad \text{if } z_0 < z < r_0 \quad (5.3.6a)$$

$$A''_{\text{th}}(z) = \pi(r_1^2 - z^2) \quad \text{if } r_0 < z < r_1 \quad (5.3.6b)$$

It is noteworthy that  $A_{\text{th}}$  as well as  $\rho_{\text{th}}$  - the area and density of the thiol ring in figure B.1 b) - are constant for  $z_0 < z < r_0$ . For details, see section B.1.

To accommodate for a more realistic model that accounts for thermal fluctuations, the vertical position of the nanoparticles was varied by a normal distribution and the edge of the toluene bulk was smoothed out using an error function (cf. B.2).

## 5.4 Pure Toluene

The bottom curve in figure 5.3 shows a reflectivity of a sample which was assumed to be pure toluene. The sample holder was rinsed in an ultrasonic bath of toluene (purity > 99,7%, puriss. p.a.) for about half an hour which was obviously insufficient, since there were some nanoparticle remnants stuck to the sample holder that were resuspended in the pure toluene sample.

The fact that even such a small amount of nanoparticles produces a surface layer clearly visible in the electron density profile in the inset of figure 5.3 (blue curve) suggests a high affinity of the nanoparticles to adsorb to the liquid/vapor interface.

While the exact quantity is unknown, it is safe to assume that the influence on experiments at regular concentrations would have been negligible to say the least. Nevertheless, after this discovery, an additional cleaning stage was implemented into the process.

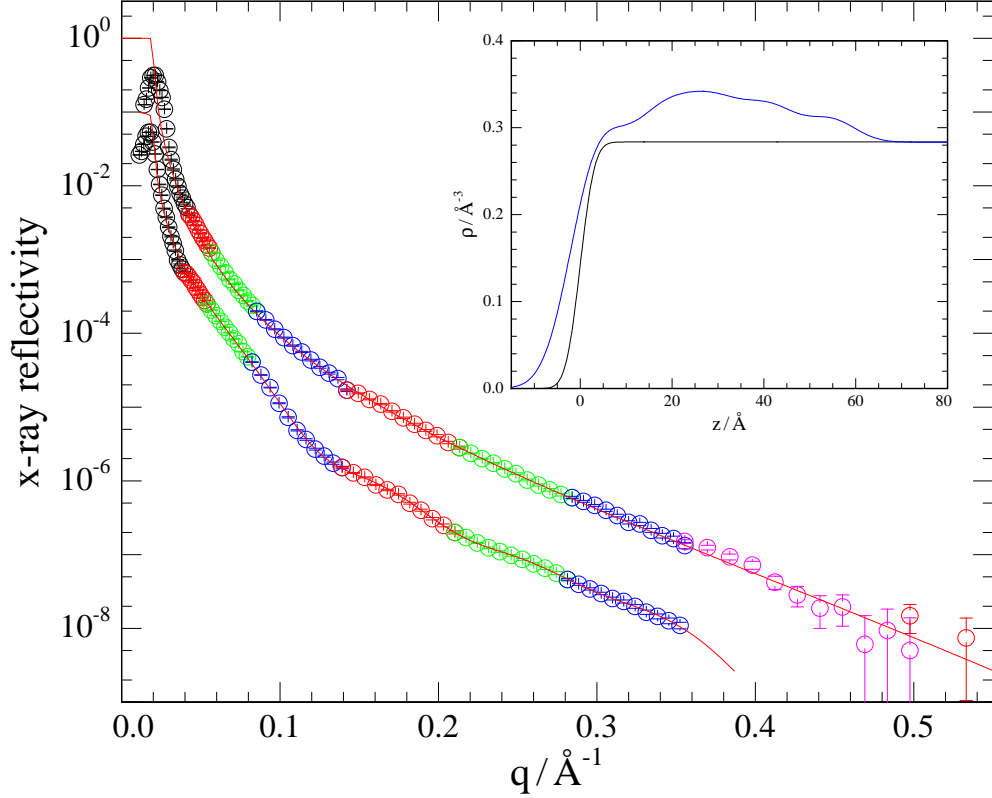


**Figure 5.3:** Reflectivity of pure toluene (top curve in the main panel) and a sample that was contaminated by remnants of nanoparticles in the sample holder (bottom curve - shifted by  $10^{-1}$  for clarity). The blue curve in the inset corresponds to the contaminated sample.

The result can be seen in figure 5.3. It shows the reflectivity of pure toluene. As is to be expected from this sample, the reflectivity data is just the Fresnel reflectivity of toluene. The electron density obtained through fitting is a very good match to the theoretical value with a deviation of only 3.6%. The surface roughness is  $3.55 \text{ \AA}$ . The capillary wave induced roughness (cf. section 1.5.1) should be around  $2.4 \text{ \AA}$ , assuming a radius of  $2.7 \text{ \AA}$  for the toluene molecules [90] and a surface tension of  $29.6 \text{ mN/m}$ , which leaves approximately  $2.6 \text{ \AA}$  as the intrinsic roughness of the interface, which in turn corresponds very well with the presumed molecular size.

Fitting the model from section 5.3 to the electron density profile of the “contaminated” toluene yields  $r_0 = 3.0 \text{ nm}$ ,  $z_0 = 2.8 \text{ nm}$ ,  $\sigma_1 = 0.72 \text{ nm}$ ,  $\sigma_2 = 1.3 \text{ nm}$  and  $a_1 = 44.05 \text{ nm}$  which corresponds to 0.5% surface coverage.

## 5.5 Multilayers

It was more by accident that it was discovered that the nanoparticles could form multilayers at the liquid/vapor interface when suspended in toluene. While simply investigating, whether or not a surface film is present when any evaporation of the solvent is suppressed, we stumbled upon this phenomenon.

After this discovery, the next logical step was to determine the circumstances which are necessary to obtain a multilayered nanoparticle film.

### 5.5.1 Formation

Once a monolayer is established, it can serve as a template for further layers. As depicted in 5.2, it is possible that either a single particle diffuses to the surface layer and is adsorbed or a (small) bulk agglomerate can attach itself as a whole. A combination of both mechanisms will result in multilayers with decreasing lateral density and eventually a rather rough cut off.

### 5.5.2 Temperature Ramps

A number of x-ray reflectivities for different concentrations and varying temperature were recorded and shall be presented in the following. The samples were prepared in the PTFE Trough and placed inside the sealed aluminum cell both mentioned in section 2.2.

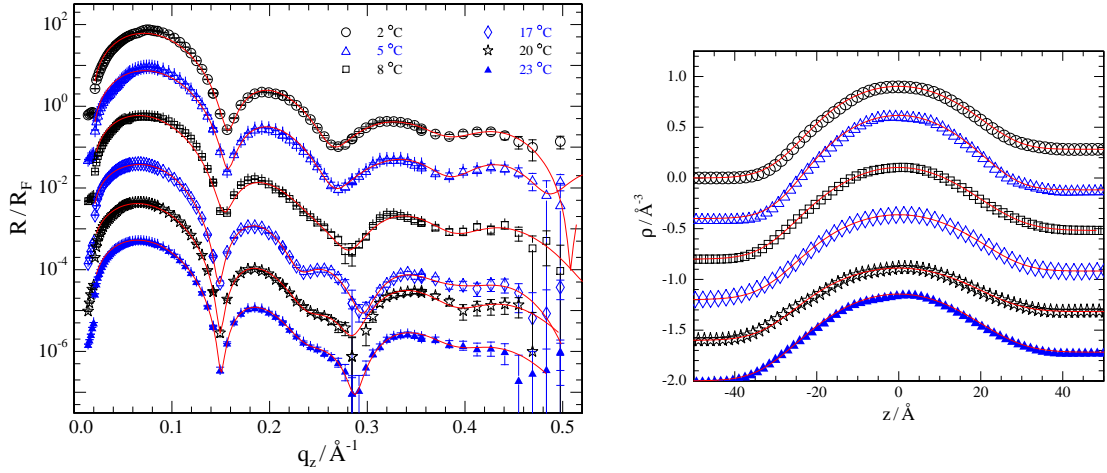
Before the sample preparation, the bottom of the aluminum cell's inside was coated with as much pure toluene as possible without spillage. This was to ensure a saturated toluene atmosphere within the cell which would prevent toluene from the actual sample from evaporating and thus preventing the mechanism mentioned in reference [71].

In short: The establishment of the surface film is explained by the retraction of the liquid surface due to evaporation which proceeds faster than the diffusion of the nanoparticles, thus "trapping" them at the liquid/vapor interface.

The electron density profiles were obtained using the stochastic fitting program StochFit by Stephen Danauskas from the University of Chicago [91]. Due to the spherical nature of the nanoparticles the analysis was not readily accessible to the conventional box model approach.

In all of the following plots, the lower curves are shifted for clarity by an easily recognizable amount relative to the top one. For each sample, the reflectivities were taken from lowest to highest temperature.

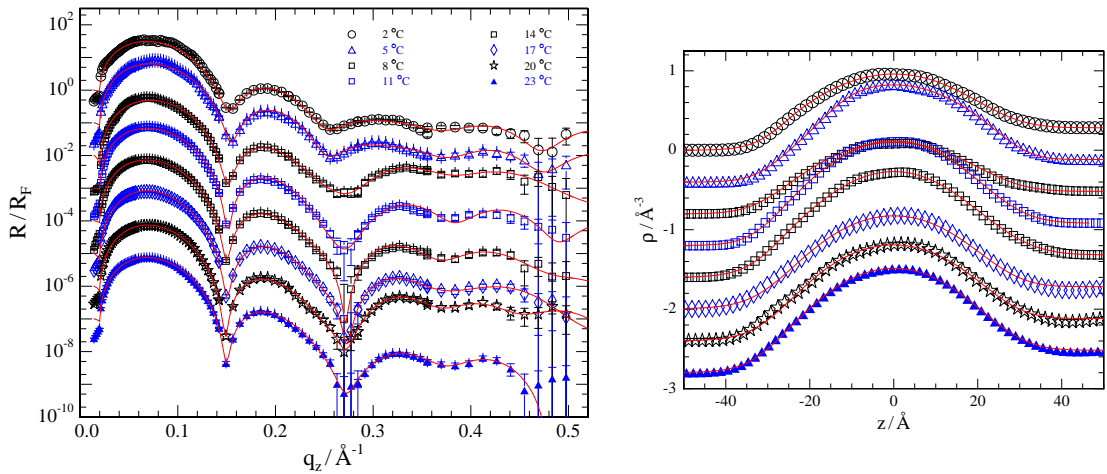
- $c = 1/100c_0^1$



While the slight change in the reflectivity curve at  $T = 17^\circ\text{C}$  might suggest a structural change in the gold nanoparticle film itself, the profiles obtained through fitting the reflectivities leave no clues to the occurrence of any temperature induced alteration of the gold layer.

Each electron density profile is fittable by the model from section 5.3. No significant trend in the surface coverage can be observed. The temperature range is arguably too small to have any effect on the monolayer.

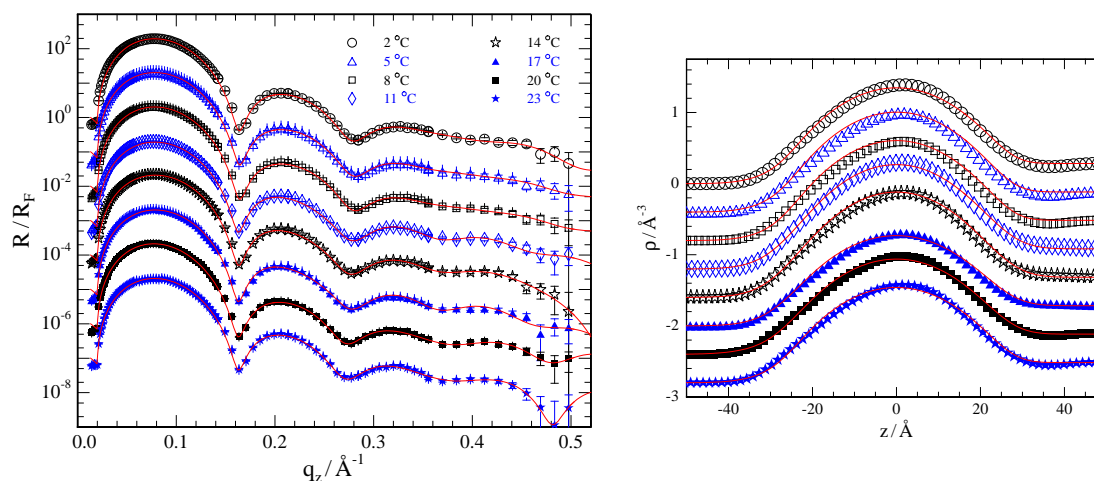
- $c = 1/30c_0$



While the overall electron density is higher for this concentration, there seems to be no temperature dependence here as well.

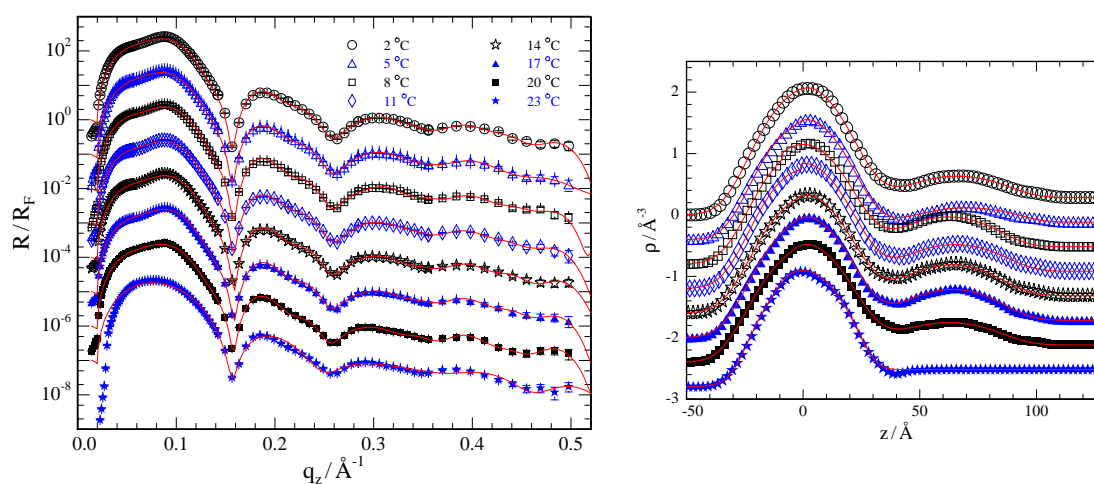
<sup>1</sup> $c_0 = 3 \pm 1 \cdot 10^{14} \text{ 1/ml}$

- $c = 1/10c_0$



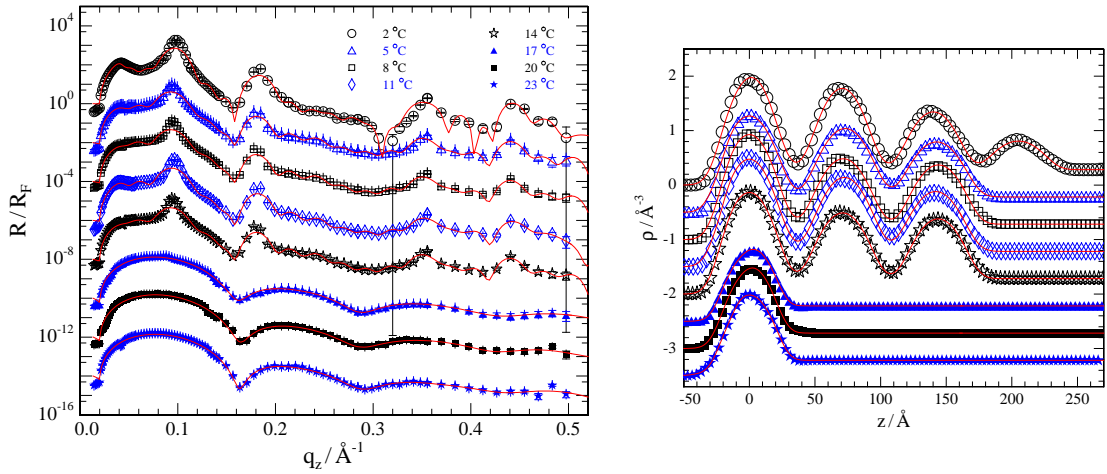
Again, the electron density of the nanoparticle film is increased while temperature has no observable effect.

- $c = 1/3c_0$



At this concentration, a second layer can be observed for the first time. A change in the reflectivity is also clearly visible, especially in the shape of a bump on the first oscillation. The bump decreases in pronunciation at 20 °C and disappears at 23 °C.

- $c = 2c_0$



This is the highest concentration that was examined. At 2 °C, a total of four layer of nanoparticles, all very clearly at the same interval can be seen in the electron density profile. The fourth layer disappears at 5 °C, leaving only three. The last three measurements are not very conclusive, unfortunately, since they were taken after the sample was left in the cell for a week following the previous measurement due to a glitch in the cooling system of the high voltage generator.

### 5.5.3 Reproducibility

The two data sets in figure 5.4 were recorded from the same sample at the same parameters ( $T = 2\text{ °C}$ ,  $c = c_0$ ) at an interval of 24 hours. The data sets are virtually identical as are the corresponding electron density profiles derived from the fits. In this case, three distinct layers with an indication of a fourth are apparent in the profiles.

Any precipitation or progressing agglomeration would lead to a change in the recorded reflectivity while these results indicate that a dynamic equilibrium is in fact maintained between nanoparticles suspended in the bulk phase and those adsorbed to the surface film.

### 5.5.4 Conclusions

The relative surface coverages as determined from the obtained electron density profiles and as defined at the end of section B.2 are presented in figure 5.5. For  $0.33c_0$  and  $2c_0$ , only that of the top layer is shown. While the data is inconclusive as to whether the temperature has any influence on the nanoparticle adsorption (while it is reasonable to assume that temperature has an influence, it is too faint to extend beyond the noise in the data at least for the temperature range in this

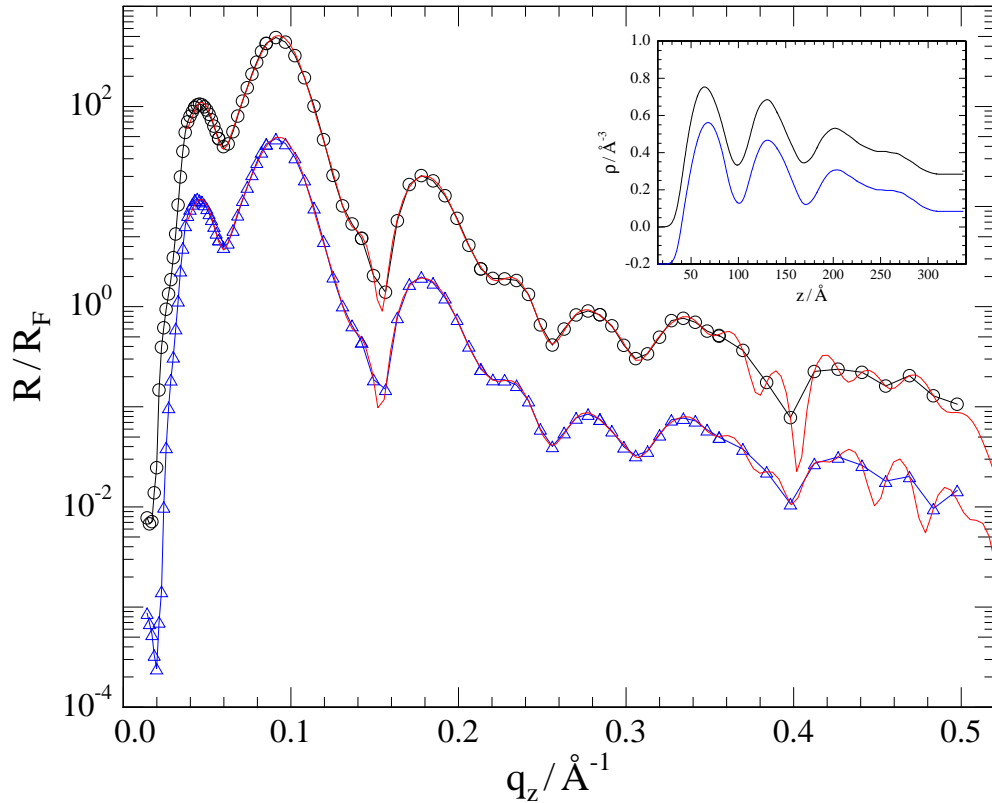


**Figure 5.4:** Two data sets of the same sample recorded with identical parameters at an interval of 24 hours. Colors of the reflectivities and the electron density profiles (inset) correspond.

study) to the liquid/vapor interface, it clearly shows that a higher concentration leads to a larger amount of adsorbed particles. - Which is hardly surprising but still worth mentioning.

From  $0.33c_0$  to  $2c_0$ , no further increase in adsorbed nanoparticles can be observed which suggests that a point of saturation is reached here. This assumption is supported by the fact that the corresponding values for the hexagonal lattice constant vary slightly around 9nm which is the size of the nanoparticles with their ligand shells.

$1/3c_0$  marks the lowest concentration for which more than one layer can be observed. Since the change in temperature seems to be sufficient for the second layer to dissolve, the absorption energy of layers beyond the first one seems to be significantly lower than that for the initial one. The findings in section 5.6 support this theory.

For  $2c_0$ , there is one additional layer at  $2^\circ\text{C}$  that vanishes at  $5^\circ\text{C}$ . The aforementioned technical difficulties with the cooling system (among other things) also made it impossible to go back down to the starting point after reaching the max-

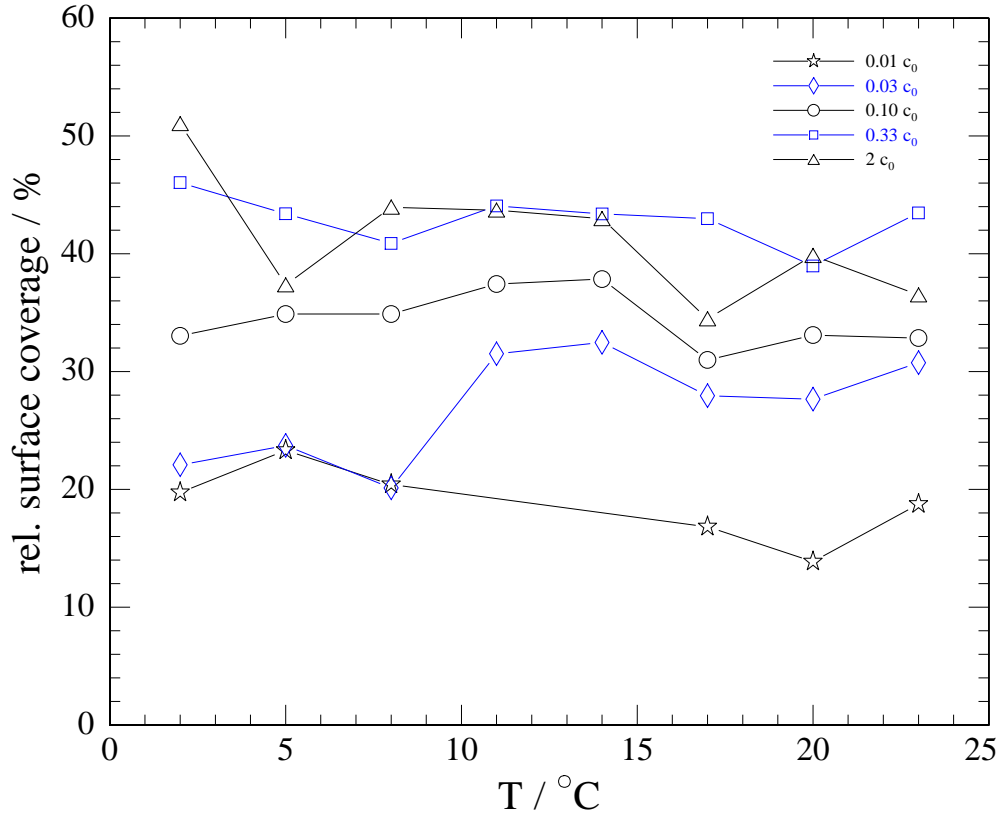


**Figure 5.5:** The relative surface coverage as obtained through fitting the electron density profiles. For  $0.33c_0$  and  $2c_0$ , only that of the top layer is shown.

imum temperature. This leaves the question whether the temperature is really responsible for the observed changes in the nanoparticle film or if it is simply a process that advances over the course of the experiment. This concern will be addressed in section 5.6.

Over all profiles with multiple layers, the distance between centers of two adjacent layers remains fairly constant at  $6.84 \pm 0.38$  nm. Assuming a close packing of the nanoparticles within the surface film, in accordance with the aforementioned 9 nm interparticle distance in the top layer, this value should be 7.35 nm, which is not too far off but still indicates that there is some amount of overlap among the ligand shells.

The values for the gold core radii are in agreement with those obtained from the electron micrographs:  $2.93 \pm 0.16$  nm averaged over all profiles.

Figure 5.6 shows an overview on the respective number of layers obtained from the analysis for each of the presented measurements. The three points in the top right corner are shaded as they represent unreliable data (cf. end of section 5.5.2). It is immediately apparent that the parametric region where only a monolayer of nanoparticles emerges at the surface is much larger than for any other configura-

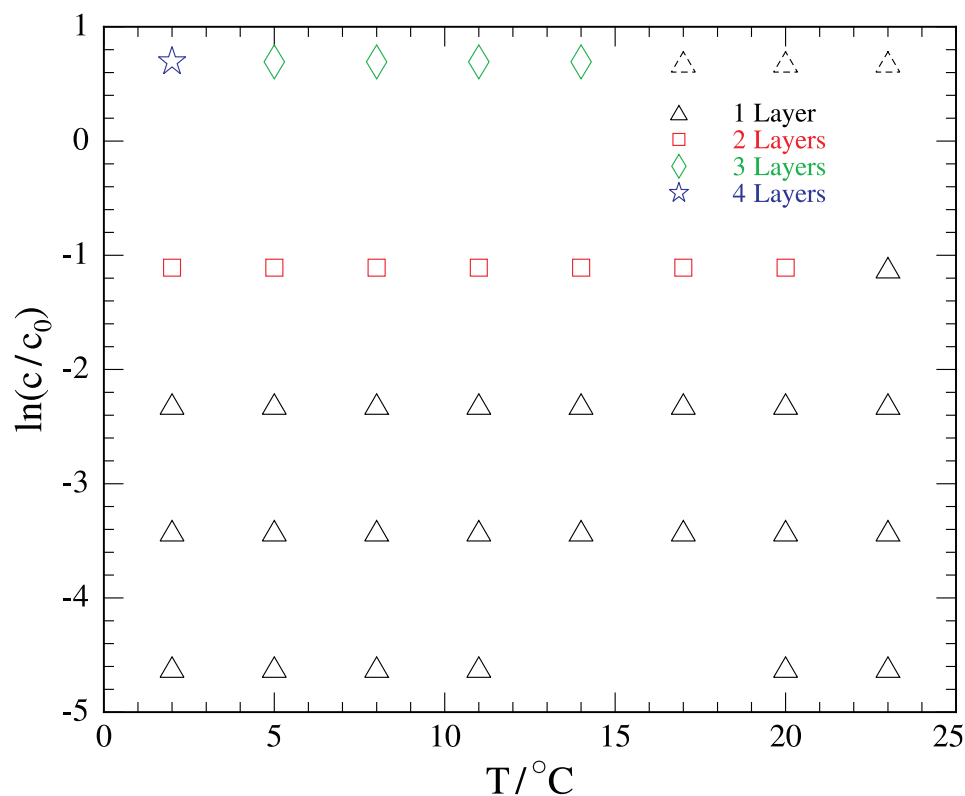


**Figure 5.6:** An overview of number of layers obtained for different values of concentration and temperature of the suspension. The three points in the top right corner are shaded as they are unreliable.

tion. An indication, that the affinity for the particles to adsorb at the surface is much larger than their interaction with each other.

## 5.6 Layering Peak Temperature Ramp

The results presented in section 5.5.2 leave doubts as to the reversibility of the multilayer formation and if it is really the change in temperature that is responsible for the gradual disappearance of the additional layers.

To assess, whether or not the temperature was in fact the determining factor, for a given sample at concentration  $2c_0$  the temperature was gradually increased from  $2^\circ\text{C}$  to  $42^\circ\text{C}$  in steps of  $0.5^\circ\text{C}$ , each of the steps taking about 25 minutes. After a few hours of waiting, the temperature was decreased again at the same rate. At each temperature, a short scan of reflected intensities over a layering peak at  $\approx 0.6^\circ$  was recorded.

The data points in figure 5.7 each represent the integrated intensity of this peak at the given temperature. While increasing the temperature (black circles in figure

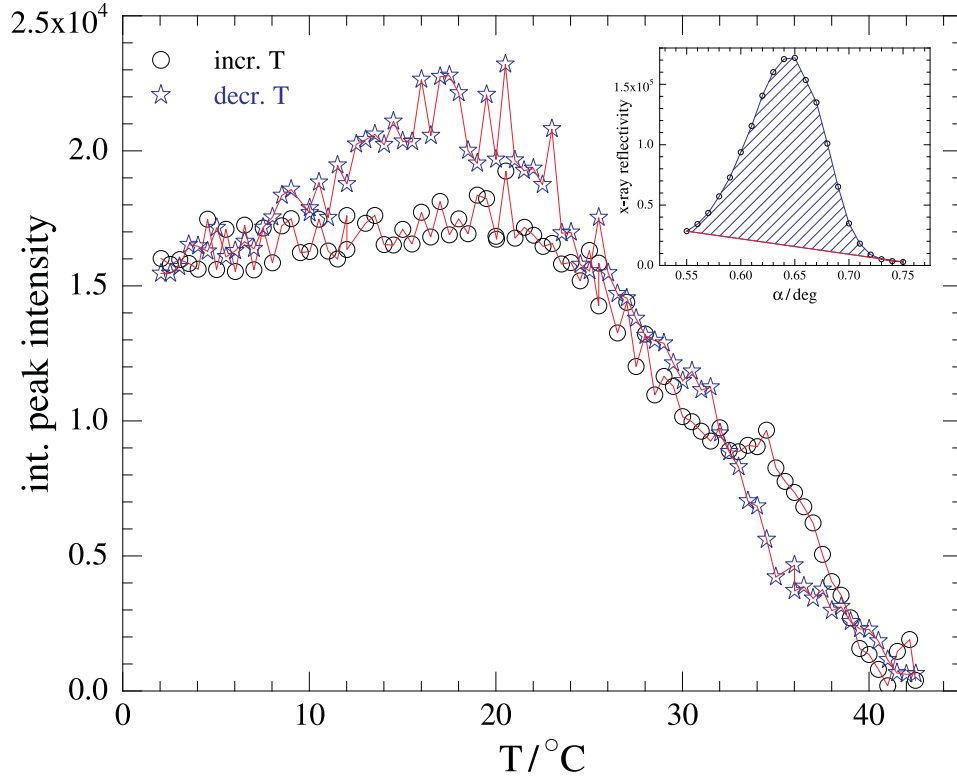


**Figure 5.7:** Each point is the integrated intensity of a short scan over a layering peak at  $\sim 0.6^\circ$  with subtracted baseline. The inset shows a single peak. The area shaded in blue corresponds to a single data point in the main plot.

5.7), the intensity remains fairly constant in the range between  $2^\circ\text{C}$  to  $22^\circ\text{C}$  and then starts to drop linearly. At  $42^\circ\text{C}$ , the peak has virtually disappeared.

While decreasing the temperature (blue stars in figure 5.7), the intensity shows the same development until the plateau is reached and then displays a small hysteresis but eventually drops to the initial value at  $2^\circ\text{C}$ .

The behavior in the  $2\text{-}20^\circ\text{C}$  range implies, that at a certain point, the multilayer reaches a state of saturation, while the hysteresis during cooling suggests an additional mechanism. It is possible that larger agglomerate-”chunks” will detach from the surface film due to gravitational forces and precipitate at the bottom of the sample and thus no longer contribute to the signal.

This would already have happened during the initial cooling before the onset of the experiment and as the temperature was increased, the agglomerates dissolved again and in that way were able to participate in the re-formation of the surface film.

The data presented in figure 5.7 confirms the assumption mentioned above and rules out the possibility that it is just a process that takes a large amount of time

and cannot be reversed.

This implies, that there is a dynamic equilibrium between particles suspended in the bulk toluene and those adsorbed at the liquid/vapor interface. As their thermal energy increases, more and more particles are able to detach from the surface layer.

Jansen *et al.* [82] suggest a square well potential for the interaction between the ligand chains of different nanoparticles whose depth is temperature dependent, to model a temperature dependent solubility of the ligands in the surrounding solvent. Since a single particle can closely interact with several particles at once (up to three) in an already established surface monolayer, whether bulk agglomerates or a multilayered surface film emerges might simply be a question of available nuclei, where a surface layer is a quite large one.

They found that for silica particles covered with octadecyl chains, solubility decreases with their radius [78]. Since the solubility is also temperature dependent, a similar mechanism might be responsible for the gradual (re)-solution of the particles from the surface film. However, the polydispersity of the particles is too low to be resolved in the obtained electron density profiles: 5% is well within the margin of error here.

## 5.7 Bulk Agglomerates

The measurement series in figure 5.8 shows data of a nanoparticle production batch different from that presented in section 5.5.2. It stands apart from the previous one in that there are two distinct peaks that are superimposed on the reflectivity pattern from a single layer at the toluene-air interface. This single layer pattern remains unchanged over the course of the entire series while the peak intensity decreases with increasing temperature and utterly disappears as 26 °C is reached.

From electron micrographs (cf. figure C.6), the nanoparticle diameter was identified to be 6 nm with a small polydispersity. As has been determined according to [79], assuming an *fcc* ordering, the peaks in figure 5.8 correspond to a nearest neighbor distance  $d$  of approximately 8.1 nm. Since the dodecanethiol chains attached to the surface of the nanoparticles are about 1.5 nm in length, they are either required to overlap by an amount of 0.9 nm or they are displaced into the larger gaps in the center of a four-particle-tetrahedron respectively.

The latter seems unlikely due to the large force required for this process while the former is in line with the interaction potential mentioned in the previous section.

It is unclear what distinguishes this sample batch from the others. A possibility might be the concentration of excess dodecanethiol molecules in the solvent as

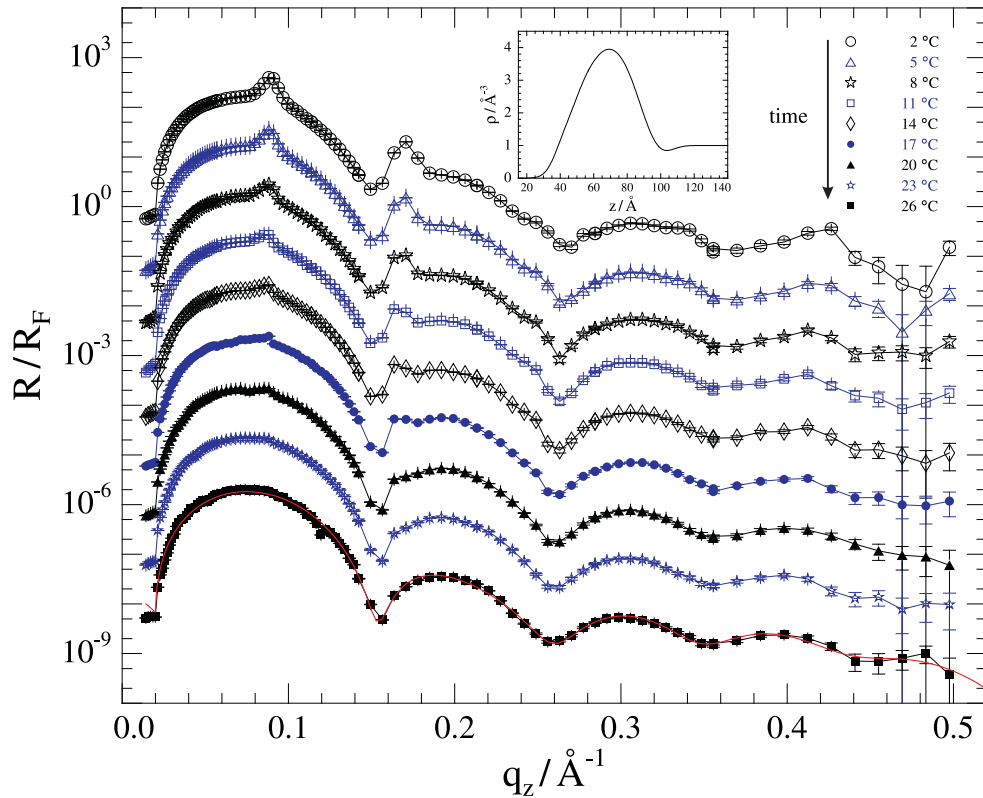


**Figure 5.8:** The two peaks at  $0.09 \text{ 1/Å}$  and  $0.17 \text{ 1/Å}$  can be identified as the  $(111)$  and  $(311)$  reflexes of an fcc lattice. The electron density profile in the inset at the top corresponds to a fit (red line) of the  $26 \text{ °C}$  data.

this has also been determined to be an influence to the nanoparticle organization by T.P. Bigioni *et al.* [71]. Or it might be as simple as some form of sample contamination, which cannot be entirely ruled out.

While, unfortunately, technical difficulties impeded the way back down to  $2 \text{ °C}$ , the temporal scale of the experiment (several days) makes it unlikely that the disappearance of the agglomerate reflexes is due to precipitation.

## 6 Summary

At the beginning of this study, an x-ray reflectometer was designed with the aim of investigating liquid samples. The installation is equipped with a copper anode as the x-ray source and a multilayer mirror to monochromatize and collimate the beam. Two different sample containers were used over the course of this work: A Langmuir trough from Kibron Inc. and a sealed sample cell built at the university workshop. Control of the setup and its peripherals is achieved via a flexible computer program that allows for a high degree of automatization.

A proof-of-concept measurement performed on silanized silicon wafers showed the applicability of the instrument. The tilt of the alkyl chains in the silane coatings was determined to be  $25^\circ$  and  $34^\circ$  for the two samples respectively.

The instrument was then used to analyze the structure of langmuir films of amphiphilic diblock copolymers (poly(ethylene oxide)-b-poly(heptafluorobutyl methacrylate) (PEO-b-PHFBMA)). Two variants with different PHFBMA-headgroup sizes were investigated at varying surface pressures to determine the structural changes in the headgroup undergone during compression of the film. While the findings were not entirely conclusive, a case can be made for a standing MA-backbone and butyl chains lying flat on the water surface.

Afterwards, toluene suspensions of gold nanoparticles ligated with dodecanethiol were studied. While initially, the goal was to verify that, even in the absence of evaporation, the nanoparticles adsorb to the liquid vapor surface, it was discovered that not only a monolayer is formed but multilayering occurs. The former was achieved by placing the samples in a small trough within a sealed cell containing a saturated toluene atmosphere. The focus then shifted to determining the conditions leading to multilayered film of nanoparticles. Both a temperature and concentration dependence could be demonstrated. While small concentrations suffice to form a monolayer of nanoparticles, multilayering requires larger ones and occurs at lower temperatures. On the other hand, temperature seems to have virtually no effect (at least not in the investigated range) on the concentration of nanoparticles within a monolayer (or the topmost layer in the case of multilayering).

## 6.1 Outlook

While it has been shown, that the formation of a multilayered surface film from a toluene suspension of dodecane thiol ligated gold nanoparticles takes place, the exact mechanisms behind it are still not altogether clear.

Further investigations through x-ray reflectometry, whether by a small anode based one or through synchrotron radiation would be sure to shed some more light on the topic. An extension of the parametric region inspected here, both in the direction of temperature and concentration is an obvious step.

On the other hand, a GISAXS study complementary to the work by Narayanan *et al.* [73] (cf. section 5.1) could divulge new information about the lateral structure of the multilayered films. However, applying this method will require synchrotron radiation.

However, it might be prudent to shift to a completely different means of investigation to gain insights to additional aspects of the phenomenon.

Ellipsometry, for example, while most probably unable to resolve individual layers, delivers much faster results on the total film thickness and should even be able to resolve the dynamic of the process.

Molecular dynamics simulations could also deliver unique insights to the topic. A thorough investigation of the thermodynamics involved in the process or a theoretical study in general could also shed some new light on the matter.

Creating thin membranes similar to those mentioned in reference [74] or [75] (cf. section 5.1), but from a multilayer film instead of a monolayer could have increased stability and rigidity.

In the introduction, I stated that this work was to show that x-ray reflectometry for liquid samples was more than a theoretical possibility for a university lab based instrument. I hope that this claim has been proven.

# Part III

## Supplemental

This part contains some complementary information: An overview of the X-Surf control program, some calculations and additional figures and photos of the equipment.



# A X-Surf

## A.1 List of Commands

- mv** motor destination  
moves motor to destination
- mvr** motor distance  
moves motor by distance from current position
- mvb** motor  
retracts motor by a small amount when end switch is hit
- stop** motor  
terminates movement of motor (only motors 1 to 10)
- spd** motor speed  
sets motor speed (values from 0 to 9)
- acc** motor acceleration  
sets motor acceleration (values from 0 to 9)
- mvab** alpha beta  
sets incident angle to alpha and reflected angle to beta  
if only one angle is specified, alpha and beta are set to the same value
- smpd** motor  
increase current for motor (only motors 1 to 10)
- smpu** motor  
decrease current for motor (only motors 1 to 10)
- status** motor  
prints status of motor (only motors 1 to 10)
- wh**  
prints position of every motor
- sl**  
prints positions and apertures of the slits
- sp** motor newPos  
set position of motor to newPos
- sslp** seconds

set sleeptime to **seconds** (waiting time after any step in a scan)

**sc** motor start end nPoints seconds

scan motor from start to end by nPoints for seconds each

**lup** motor interval nPoints seconds

scan motor from -interval to +interval from current position by nPoints for seconds each

**absc** alphaStart alphaStop [BetaStart BetaStop] nPoints seconds

scan alpha from alphaStart to alphaStop and beta from betaStart to betaStop by nPoints for seconds each

if only one angle is specified, alpha and beta are set to the same value

**csc** motors start end nPoints seconds

Coupled scan of motors from start to end respectively by nPoints for seconds each

an arbitrary amount of motors can be involved in this scan - for instance, the vertical position of the sample (sh) and the detector (oh) can be scanned simultaneously

**cent** [newPos]

move motor of last scan to center of last scan [and optionally set position to newPos afterwards (newPos can either be 'c' for 'current' or a numeric value)]

**max** [newPos]

move motor of last scan to maximum of last scan [and optionally set position to newPos afterwards (newPos can either be 'c' for 'current' or a numeric value)]

**c** seconds

count x-ray photons for seconds

**temp** temperature

set setpoint on temperature controller to temperature

**zero**

set the current positions of ir, or, sh and oh to 0 (used for quick alignment to the sample's surface orientation)

**timescan** nPoints [seconds]

count repeatedly for seconds each point while the most recent nPoints will be displayed in plot

by default seconds will be 1 if omitted

## A.2 Screenshot

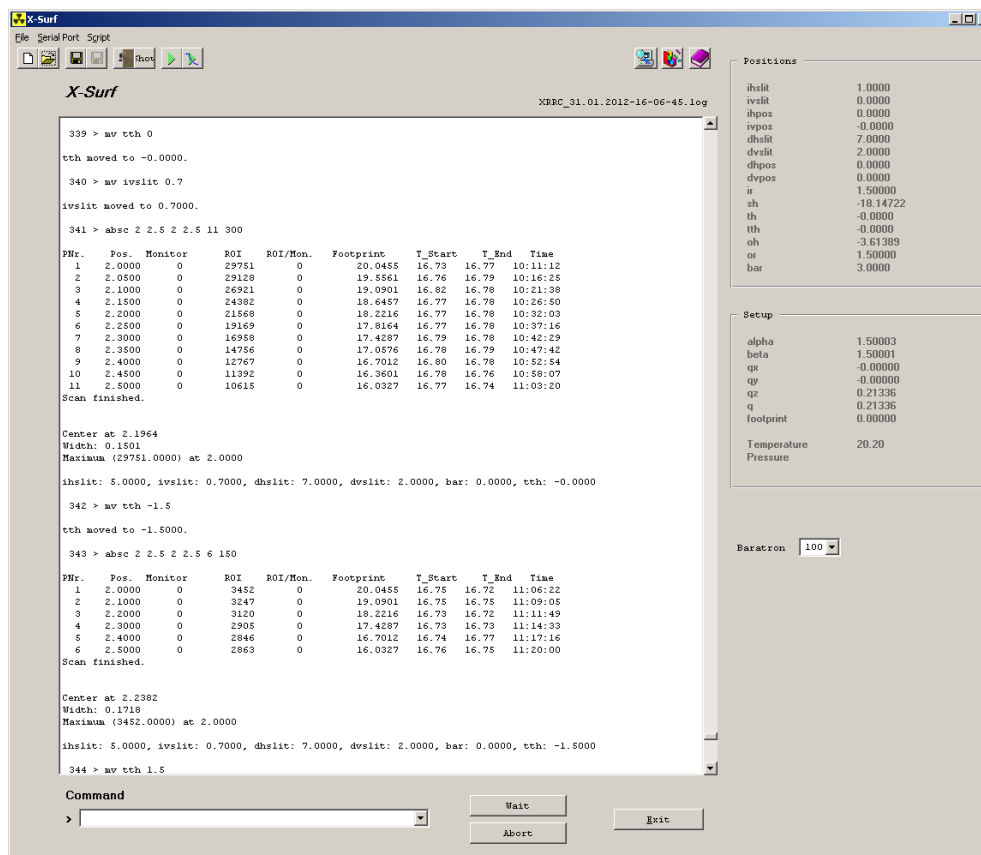


**Figure A.1:** A screenshot of the “X-Surf”-Software used to control the reflectometer. The large panel shows every in- and output. Any command is entered into the box beneath. Of the two frames on the right, the upper one shows the most recent positions of the all the motors while the one below displays some meta parameters of the system. The buttons in the top left give quick access to file control and the like.

### A.3 List of Motors

- **ihslit**: horizontal aperture of incident slit
- **ivslit**: vertical aperture of incident slit
- **ihpos**: horizontal position of incident slit
- **ivpos**: vertical position of incident slit
  
- **dhslit**: horizontal aperture of detector slit
- **dvslit**: vertical aperture of detector slit
- **dhpos**: horizontal position of detector slit
- **dvpos**: vertical position of detector slit
  
- **ir**: inclination of incident arm
- **sh**: vertical position of sample stage
- **th**:  $\theta$ , rotation of sample around the  $z$ -axis
- **tth**:  $2\theta$ , rotation of detector arm around the same axis
- **oh**: vertical position of detector arm
- **or**: inclination of detector arm
- **bar**: attenuator level

# B Calculations

## B.1 Thiol Layer Density

For the average cross sectional electron density of the dodecanethiol layer at height  $z$ , there are two cases to be considered. First, for  $z_0 < z < r_0$ , i.e. the part that sticks out of the liquid surface and at height  $z$  represents a ring (cf. figure B.1) around the gold core. Second, for  $r_0 < z < r_1$ , i.e. the cap on top of gold core (cf. figure 5.1 for clarity).

The density of the thiol layer decays towards the outer edge of the particle (with increasing radius  $r$ ) since the surface of a sphere with radius  $r$  increases proportional to  $r^2$  but the number of chains remains the same.

Assuming that for  $r = r_0$ , i.e. on the gold core's surface, the electron density is that of bulk dodcane  $\rho_{\text{th},0} = 0.26 \text{ \AA}^{-3}$ , the electron density depends on  $r$  as

$$\rho_{\text{th}}(r) = \rho_{\text{th},0} r_0^2 / r^2 \quad , \quad r_0 < r < r_1 \quad (\text{B.1.1})$$

- $z_0 < z < r_0$

Integrated over a ring at height  $z$  ( $b_0 = \sqrt{r_0^2 - z^2}$ ,  $b_1 = \sqrt{r_1^2 - z^2}$ ), the electron density is

$$\rho_{\text{th, int}}(z) = \int_{b_0}^{b_1} \rho_{\text{th}}(b) 2\pi b \, db \quad (\text{B.1.2})$$

$$= \int_{b_0}^{b_1} \rho_{\text{th},0} \frac{r_0^2}{b^2 + z^2} 2\pi b \, db \quad (\text{B.1.3})$$

$$= \rho_{\text{th},0} \pi r_0^2 \ln(b^2 + z^2) \Big|_{b_0}^{b_1} \quad (\text{B.1.4})$$

$$= \rho_{\text{th},0} \pi r_0^2 \left( \ln(b_1^2 + z^2) - \ln(b_0^2 + z^2) \right) \quad (\text{B.1.5})$$

$$= \rho_{\text{th},0} \pi r_0^2 \left( \ln(r_1^2 - z^2 + z^2) - \ln(r_0^2 - z^2 + z^2) \right) \quad (\text{B.1.6})$$

$$= \rho_{\text{th},0} \pi r_0^2 \ln(r_1^2 / r_0^2) \quad (\text{B.1.7})$$

which is independent of  $z$ .

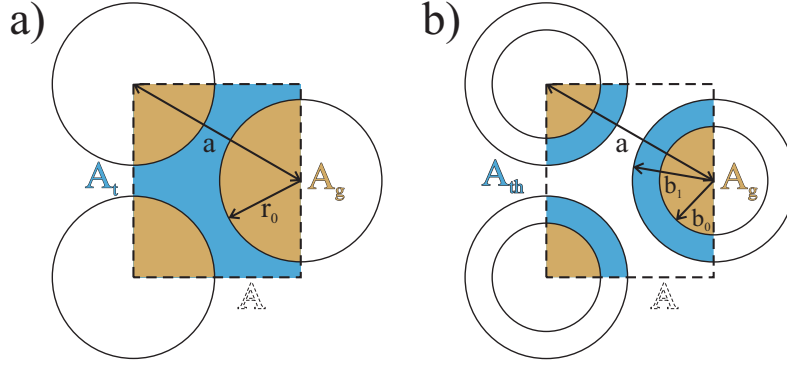


**Figure B.1:** Unit cell of an assumed hexagonal close packing of nanoparticles at the liquid vapor interface. The total area of the unit cell (dashed rectangle) is  $A$ , the area composed of gold is  $A_g$ .

a) shows a cross section through the centers of the gold cores. The space  $A_t$  in between is filled with toluene (and the optically indistinguishable dodecanethiol).

b) shows a cross section above the toluene surface. The area  $A_{th}$  is that of the ligand shell. The remaining space is vapor.

This has to be normalized to the ring area, which is

$$A'_{th}(z) = \pi(b_1^2 - b_0^2) \quad (\text{B.1.8})$$

$$= \pi(r_1^2 - z^2 - (r_0^2 - z^2)) \quad (\text{B.1.9})$$

$$= \pi(r_1^2 - r_0^2) \quad (\text{B.1.10})$$

$$=: A'_{th} \quad (\text{B.1.11})$$

which is also independent of  $z$ .

Consequently, the averaged electron density over the ring area is

$$\rho'_{th} := \frac{\rho'_{th, \text{int}}(z)}{A'_{th}(z)} = \rho_{th,0} \ln(r_1^2/r_0^2) \frac{r_0^2}{r_1^2 - r_0^2} \quad (\text{B.1.12})$$

- $r_0 < z < r_1$  The integrated electron density of a slice of the cap at height  $z$  is

$$\rho''_{\text{th, int}}(z) = \int_0^{b_1} \rho_{\text{th}}(b) 2\pi b \, db \quad (\text{B.1.13})$$

$$= \int_0^{b_1} \rho_{\text{th},0} \frac{r_0^2}{b^2 + z^2} 2\pi b \, db \quad (\text{B.1.14})$$

$$= \rho_{\text{th},0} \pi r_0^2 \ln(b^2 + z^2) \Big|_0^{b_1} \quad (\text{B.1.15})$$

$$= \rho_{\text{th},0} \pi r_0^2 (\ln(b_1^2 + z^2) - \ln(z^2)) \quad (\text{B.1.16})$$

$$= \rho_{\text{th},0} \pi r_0^2 (\ln(r_1^2 - z^2 + z^2) - \ln(z^2)) \quad (\text{B.1.17})$$

$$= \rho_{\text{th},0} \pi r_0^2 \ln(r_1^2/z^2) \quad (\text{B.1.18})$$

This has to be normalized to the slice area, which is

$$A''_{\text{th}}(z) = \pi b_1^2 = \pi(r_1^2 - z^2) \quad (\text{B.1.19})$$

Consequently, the averaged electron density of a slice is

$$\rho''_{\text{th}}(z) = \frac{\rho''_{\text{th, int}}(z)}{A''_{\text{th}}(z)} = \rho_{\text{th},0} \ln(r_1^2/z^2) \frac{r_0^2}{r_1^2 - z^2} \quad (\text{B.1.20})$$

## B.2 Complete NP (Mono)-Layer Density Model

Here a single expression for the complete electron density profile of a nanoparticle monolayer will be given.

To accommodate for thermal fluctuations, a normal distribution

$$P_{\sigma_2}(\delta) = \frac{1}{\sqrt{2\pi}\sigma_2} e^{-\frac{1}{2}\frac{\delta^2}{\sigma_2^2}} \quad (\text{B.2.1})$$

is applied to the vertical positions of the particles.

The total electron density then is

$$\rho_{\text{tot}}(z) = (\tilde{\rho}_{\text{g},1}(z) + \tilde{\rho}'_{\text{th}}(z) + \tilde{\rho}''_{\text{th}}(z) + \tilde{\rho}_{\text{t},1}(z))/A_1. \quad (\text{B.2.2})$$

Here

$$\tilde{\rho}_{\text{g},1}(z) = \int_{-\infty}^{\infty} \rho_{\text{g},0} A_{\text{g},1}(z, \delta) c_{\text{g},1}(z, \delta) P_{\sigma_2}(\delta) d\delta \quad (\text{B.2.3a})$$

is the contribution of the gold cores with

$$A_{\text{g},1}(z, \delta) = \pi b_0^2 = \pi(r_0^2 - (z + \delta)^2), \quad (\text{B.2.3b})$$

the cross sectional area of the gold core at height  $z$  varied by  $\delta$ , and

$$c_{\text{g},1}(z, \delta) = \Theta(r_0 + (z + \delta)) \Theta(r_0 - (z + \delta)). \quad (\text{B.2.3c})$$

The cut-off function  $c_{\text{g},1}(z, \delta)$  ( $\Theta$  is the Heaviside step function) is necessary to avoid the assumption of negative (and thus, non-physical) values.  $\rho_{\text{g},0}$  is the bulk electron density of gold.

The remaining summands are:

$$\tilde{\rho}'_{\text{th}}(z) = \int_{-\infty}^{\infty} \rho'_{\text{th}} A'_{\text{th}}(z, \delta) c'_{\text{th}}(z, \delta) P_{\sigma_2}(\delta) d\delta, \quad (\text{B.2.4a})$$

the contribution of the lower part of the thiol layer as calculated in (B.1.12), with

$$\rho'_{\text{th}}(z, \delta) = \rho_{\text{th},0} \ln(r_1^2/r_0^2) \frac{r_0^2}{r_1^2 - r_0^2} \quad (\text{B.2.4b})$$

$$A'_{\text{th}}(z, \delta) = \pi(r_1^2 - r_0^2) \quad (\text{B.2.4c})$$

$$c'_{\text{th}}(z, \delta) = \frac{1}{2} \left( 1 + \operatorname{erf} \left( \frac{z - z_0}{\sqrt{2}\sigma_1} \right) \right) \Theta(r_0 - (z + \delta)) \quad (\text{B.2.4d})$$

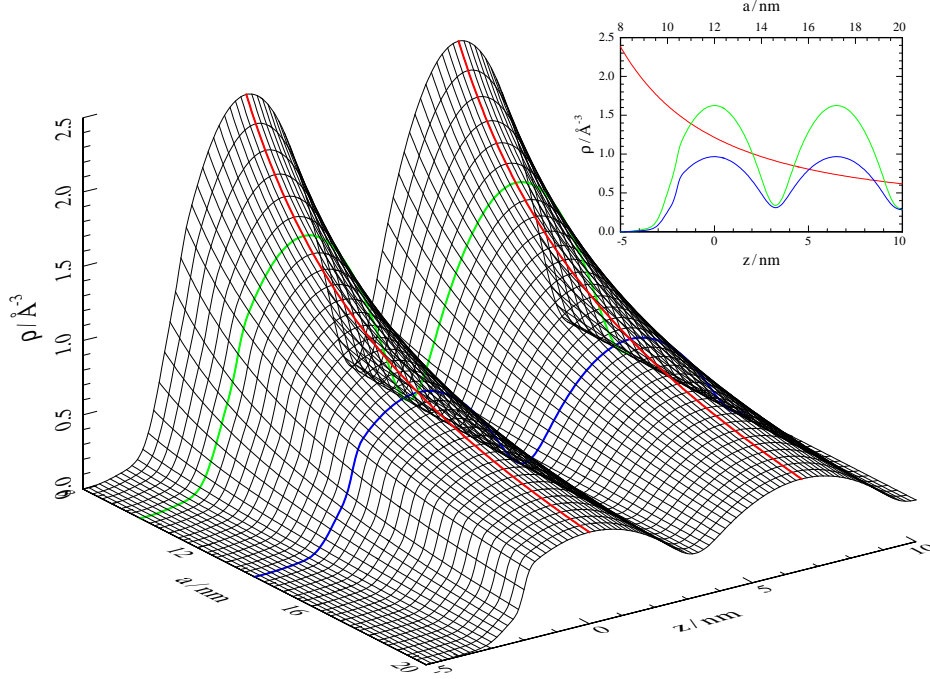


**Figure B.2:** A 3D-plot of the electron density profile of a gold nanoparticle bi-layer as a function of  $z$ , the direction perpendicular to the liquid vapor interface, and  $a$ , the lattice constant as for an assumed hexagonal ordering of the particles. The second layer has its center at  $z_2 = 6.5$  nm. The red, green and blue curves in the inset correspond to those of the same colors in the main display. The red lines are the density at  $z = 0$  and  $z = z_2$ , i.e. that of a cross section through the centers of the particles - which is also the maximum of density within the film. The green and blue lines are picked as representative profiles for  $a = 10$  nm and  $a = 14$  nm respectively.

$\text{erf}\left(\frac{z-z_0}{\sqrt{2}\sigma_1}\right)$  represents the smoothed edge of the bulk toluene with the Gaussian error function

$$\text{erf}(x) = \frac{2}{\sqrt{\pi}} \int_0^x e^{-t^2} dt. \quad (\text{B.2.5})$$

$$\tilde{\rho}_{\text{th}}''(z) = \int_{-\infty}^{\infty} \rho_{\text{th}}''(z, \delta) A_{\text{th}}''(z + \delta) c_{\text{th}}''(z + \delta) P_{\sigma_2}(\delta) d\delta \quad (\text{B.2.6a})$$

the contribution of the lower part of the thiol layer as calculated in (B.1.20), with

$$\rho_{\text{th}}''(z, \delta) = \rho_{\text{th},0} \ln(r_1^2/(z + \delta)^2) \frac{r_0^2}{r_1^2 - (z + \delta)^2} \quad (\text{B.2.6b})$$

$$A_{\text{th}}''(z, \delta) = \pi b_1^2 = \pi(r_1^2 - (z + \delta)^2) \quad (\text{B.2.6c})$$

$$c_{\text{th}}''(z, \delta) = \Theta((z + \delta) - r_0) \Theta(r_1 - (z + \delta)) \quad (\text{B.2.6d})$$

Finally, the integral

$$\tilde{\rho}_{t,1}(z) = \int_{-\infty}^{\infty} \rho_{t,0} A_{t,1}(z, \delta) c_t(z) P_{\sigma_2}(\delta) d\delta \quad (\text{B.2.7a})$$

can be calculated analogously to (B.2.3a), since

$$A_{t,1}(z, \delta) = A_1 - A_{g,1}(z, \delta). \quad (\text{B.2.7b})$$

$$c_t(z) = \frac{1}{2} \left( 1 + \operatorname{erf} \left( \frac{z_0 - z}{\sqrt{2}\sigma_1} \right) \right) \quad (\text{B.2.7c})$$

$c_t(z)$  again is the toluene bulk edge.

$$A_1 = \frac{1}{2} \sqrt{3} a_1^2 \quad (\text{B.2.8})$$

is the total area of the unit cell with lattice constant  $a_1$ .

An additional number of  $n$  layers can be introduced by adding

$$\sum_{i=2}^{n+1} \left( \tilde{\rho}_{t,i}(z) + \tilde{\rho}_{g,i}(z) \right) / A_i \quad (\text{B.2.9a})$$

with

$$\tilde{\rho}_{t,i}(z) = \int_{-\infty}^{\infty} \rho_{t,0} A_{t,i}(z, \delta) c_t(z) P_{\sigma_2}(\delta) d\delta \quad (\text{B.2.9b})$$

and

$$\tilde{\rho}_{g,i}(z) = \int_{-\infty}^{\infty} \rho_{g,0} A_{g,i}(z, \delta) c_{g,i}(z, \delta) P_{\sigma_2}(\delta) d\delta \quad (\text{B.2.9c})$$

where these are versions of  $\tilde{\rho}_{t,1}(z)$  and  $\tilde{\rho}_{g,1}(z)$  that are shifted by a distance  $z_i$ :

$$A_{g,i}(z, \delta) = \pi(r_0^2 - (z - z_i + \delta)^2), \quad (\text{B.2.9d})$$

$$c_{g,i}(z, \delta) = \Theta(r_0 + (z - z_i + \delta)) \Theta(r_0 - (z - z_i + \delta)) \quad (\text{B.2.9e})$$

$$A_{t,i}(z, \delta) = A_i - A_{g,i}(z, \delta) \quad (\text{B.2.9f})$$

Since the ligand shells in additional layers are completely submerged in the toluene bulk, their contribution is completely negligible.

While the integrals in (B.2.3a) and (B.2.4a) can be calculated analytically, the one in (B.2.6a) (to the best of my knowledge) cannot. That's why for the analysis  $\ln(r_1^2/(z + \delta)^2)$  was replaced with its Taylor expansion including the quadratic

term around  $z_p = (r_1 + r_2)/2$ . The resulting error is negligible to say the least since the contribution of  $\tilde{\rho}_{\text{th}}''(z)$  to the total profile is already rather small.

Figure B.2 shows a 3D-plot of the electron density in a bi-layer as a function of  $z$  and  $a_1 = a_2 = a$  for the following values:

$$r_0 = 3 \text{ nm} \quad r_1 = 4.5 \text{ nm} \quad z_0 = 2 \text{ nm} \quad (\text{B.2.10a})$$

$$z_2 = 6.5 \text{ nm} \quad \sigma_1 = 0.3 \text{ nm} \quad \sigma_2 = 0.3 \text{ nm} \quad (\text{B.2.10b})$$

$$\rho_{\text{t},0} = 0.28 \text{ \AA}^{-3} \quad \rho_{\text{g},0} = 4.44 \text{ \AA}^{-3} \quad \rho_{\text{th},0} = 0.26 \text{ \AA}^{-3} \quad (\text{B.2.10c})$$

It is immediately apparent that even for large values of  $a$  - and thus a small coverage of nanoparticles - the profile is dominated by the comparably huge electron density of gold as opposed to those of toluene or dodecane. While it is unreasonable to assume that a hexagonal ordering will be established for low surface coverages,  $a$  is still a useful measure for the nanoparticle fraction at the liquid/vapor interface.

If 100 % surface coverage corresponds to  $a = 6 \text{ nm}$ , i.e. the gold cores are in touch with each other - an unrealistic scenario under normal conditions - then the green exemplary profile for  $a = 10 \text{ nm}$  matches a surface coverage of 36 %.  $a = 14 \text{ nm}$  means 18.4 % and  $a = 20$  is equivalent to 9.0 %.

The toluene edge is barely perceptible for lower values of  $a$  and becomes more distinct as  $a$  increases since the fraction of gold compared to toluene decreases.



## C Additional Figures

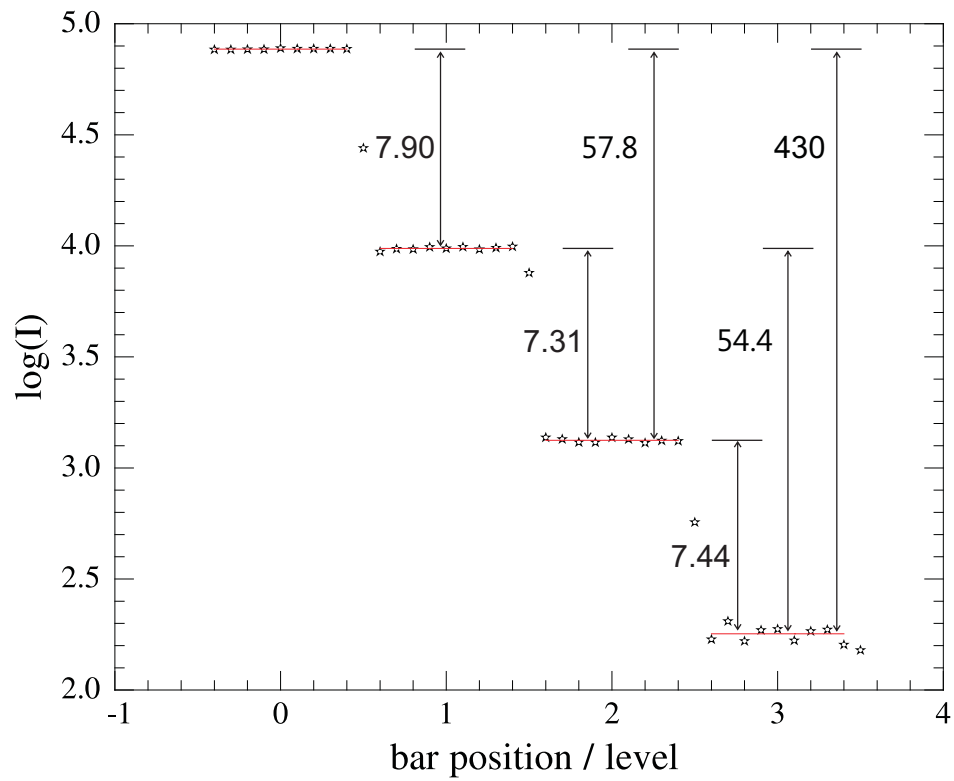


*Figure C.1: Primary beam intensity versus attenuator level.*

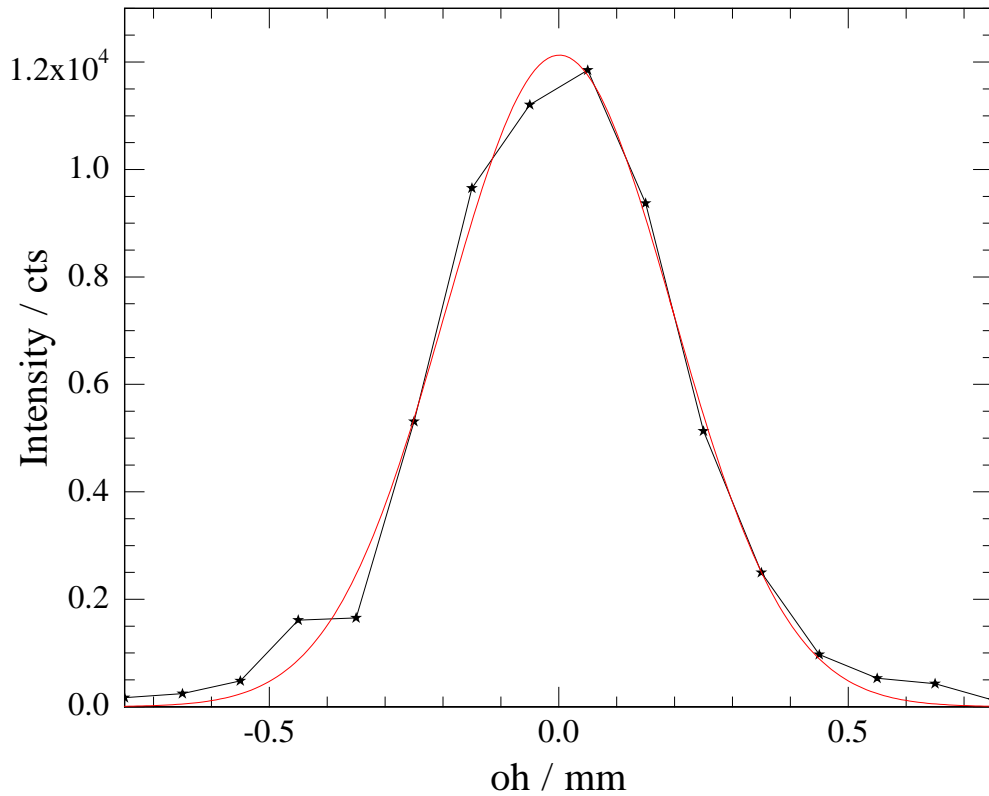


**Figure C.2:** Profile of the primary beam as recorded with  $ivslit = 10 \mu\text{m}$  and  $dvslit = 100 \mu\text{m}$ . The red line is a gaussian fit to the peak that yields  $\sigma = 0.27 \text{ mm}$ . Subtracting the influence from the slit width leaves  $0.44 \text{ mm}$  as the actual width of the primary beam at the location of the detector.

This results in a  $0.024^\circ$  divergence which basically determines the highest achievable angular resolution of the instrument.

The small imperfections probably stem from tiny flaws in the edges of the slit blades. However, for the overall signal, they are of no import.

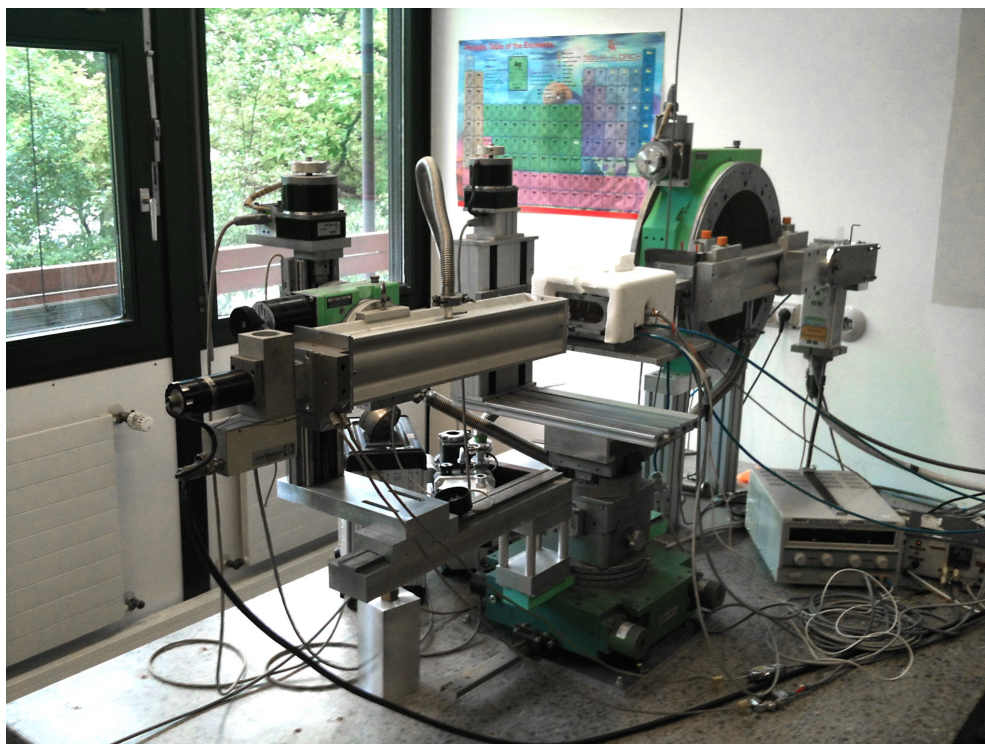


*Figure C.3: A real life picture of the reflectometer. The anode is on the far end with the sample cell in the middle covered in Styrofoam for temperature isolation.*

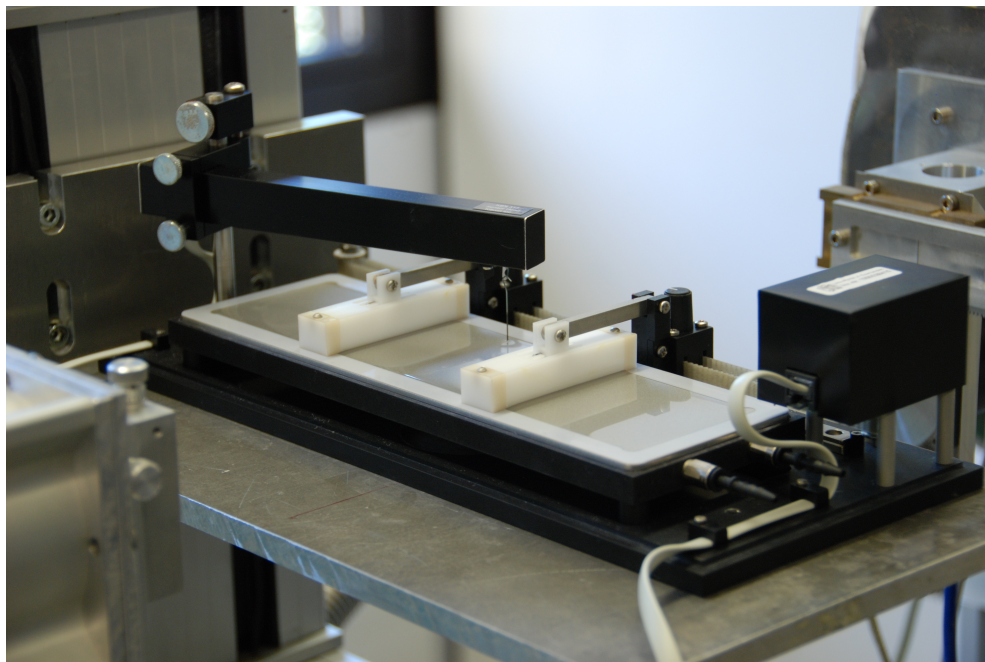


*Figure C.4: A real life picture of the Langmuir trough with the Wilhemly wire in the center of the image between the two Delrin barriers. A thin film of water covers the bottom of the trough.*

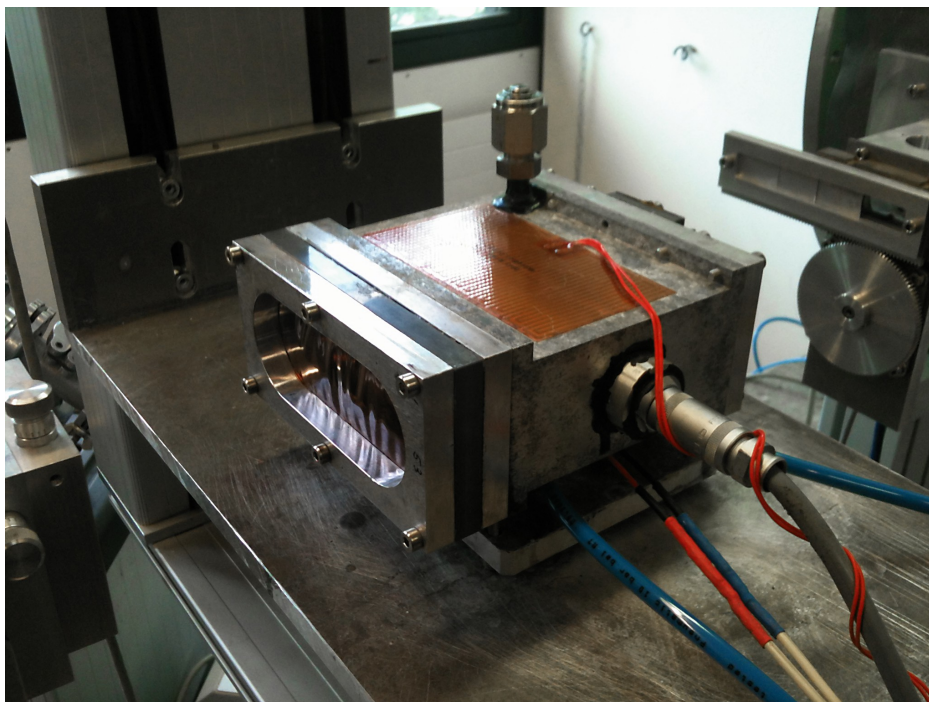


**Figure C.5:** The in house built sealed sample cell. The blue hoses at the bottom supply coolant to the Peltier cooler's hot side. The wires in between connect to the Peltier element itself. Above is the feedthrough for the temperature sensor and the orange patch on top is the heater foil.

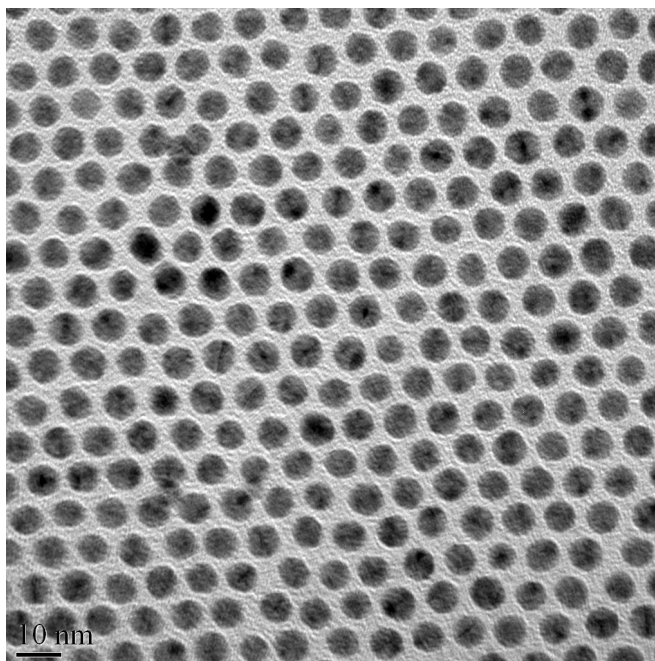


**Figure C.6:** Electron micrograph of a dried gold nanoparticle suspension. Courtesy provided by Tobias Kraus (INM Saarbrücken).

# List of Figures

## Part I

### Chapter 1: Reflection of X-Rays

1.1	Geometry of x-ray reflection . . . . .	10
1.2	Reflectivity of x-rays from a simple flat interface . . . . .	15

### Chapter 2: Experimental Setup

2.1	The footprint effect . . . . .	22
2.2	The Goebel mirror . . . . .	23
2.3	Sketch of the reflectometer . . . . .	24
2.4	Sketch of the sample holders . . . . .	25

### Chapter 3: Proof of Concept: Characterization of Hydrophobized Si-Wafers

3.1	DTS and OTS . . . . .	27
3.2	Reflectivity of DTS on silicon . . . . .	28
3.3	Reflectivity of OTS on silicon . . . . .	29

## Part II

### Chapter 4: Langmuir Films of Amphiphilic Diblock Copolymers

4.1	Mushroom and Brush Polymer Phases . . . . .	34
4.2	Polymer compression isotherms . . . . .	36
4.3	Reflectivity of PEO <sub>5</sub> F <sub>64</sub> . . . . .	37
4.4	Molecular Structure of (P)HFBMA . . . . .	39

### Chapter 5: Surface Layering of Suspended Au-Nanoparticles

5.1	Sketch of a nanoparticle . . . . .	43
5.2	Surface layer formation . . . . .	43

---

5.3	Reflectivity of pure toluene . . . . .	46
5.4	Reproducibility . . . . .	51
5.5	Relative surface coverages . . . . .	52
5.6	Overview on layer numbers . . . . .	53
5.7	Layering peak temperature ramp . . . . .	54
5.8	Agglomerate Peaks . . . . .	56

### Part III

#### Chapter A: X-Surf

A.1	X-Surf screenshot . . . . .	63
-----	-----------------------------	----

#### Chapter B: Calculations

B.1	Hexagonal nanoparticle lattice unit cell . . . . .	66
B.2	Nanoparticle bi-layer 3D-plot . . . . .	69

#### Chapter C: Additional Figures

C.1	Primary beam intensity . . . . .	73
C.2	Primary beam profile . . . . .	74
C.3	Photo of the reflectometer . . . . .	75
C.4	Photo of the Langmuir trough . . . . .	75
C.5	Photo of the cell . . . . .	76
C.6	Nanoparticle electron micrograph . . . . .	76

# Bibliography

- [1] Wilhelm Conrad Roentgen. “On A New Kind Of Rays”. In: *Nature* 53.1369 (1896), pp. 274–276 (cit. on p. 1).
- [2] Jean Daillant and Alain Gibaud. *X-ray and Neutron Reflectivity : Principles and Applications*. Vol. 770. Lecture Notes in Physics. Berlin: Springer, 2009. URL: <http://www.springerlink.com/content/g35077m42p07/#section=175715&page=1> (cit. on pp. 9, 33).
- [3] Max Born and Emil Wolf. *Principles of Optics Electromagnetic Theory of Propagation, Interference and Diffraction of Light*. Ed. by Max Born and Emil Wolf. 5th Edition. Pergamon Press, 1975 (cit. on p. 9).
- [4] L. G. Parratt. “Surface Studies of Solids by Total Reflection of X-Rays”. In: *Physical Review* 95.2 (July 1954), pp. 359–369. DOI: [10.1103/PhysRev.95.359](https://doi.org/10.1103/PhysRev.95.359). URL: <http://link.aps.org/doi/10.1103/PhysRev.95.359> (cit. on p. 16).
- [5] Metin Tolan. *X-ray scattering from soft - matter thin films*. Vol. 148. Springer Tracts in Modern Physics. Springer-Verlag, 1999 (cit. on pp. 16, 33).
- [6] A. Braslau, P. S. Pershan, G. Swislow, B. M. Ocko, and J. Als-Nielsen. “Capillary waves on the surface of simple liquids measured by x-ray reflectivity”. In: *Physical Review A* 38.5 (Sept. 1988), pp. 2457–2470. DOI: [10.1103/PhysRevA.38.2457](https://doi.org/10.1103/PhysRevA.38.2457). URL: <http://link.aps.org/doi/10.1103/PhysRevA.38.2457> (cit. on p. 19).
- [7] M. Schuster and H. Gobel. “Parallel-beam coupling into channel-cut monochromators using curved graded multilayers”. In: *Journal of Physics D: Applied Physics* 28.4A (Apr. 1995), A270–A275. ISSN: 0022-3727. DOI: [10.1088/0022-3727/28/4A/053](https://doi.org/10.1088/0022-3727/28/4A/053). URL: <http://iopscience.iop.org/0022-3727/28/4A/053/> (cit. on p. 21).
- [8] Jacob Sagiv. “Organized monolayers by adsorption. 1. Formation and structure of oleophobic mixed monolayers on solid surfaces”. In: *Journal of the American Chemical Society* 102.1 (Jan. 1980), pp. 92–98. ISSN: 0002-7863. DOI: [10.1021/ja00521a016](https://doi.org/10.1021/ja00521a016). URL: <http://dx.doi.org/10.1021/ja00521a016> (cit. on p. 27).
- [9] Ken-ichi Iimura, Yayoi Nakajima, and Teiji Kato. “A study on structures and formation mechanisms of self-assembled monolayers of n-alkyltrichlorosilanes using infrared spectroscopy and atomic force microscopy”. In: *Thin Solid Films* 379.1–2 (Dec. 2000), pp. 230–239. ISSN: 0040-6090. DOI: [10.1016/S0040-6090\(00\)01544-3](https://doi.org/10.1016/S0040-6090(00)01544-3). URL: <http://www.sciencedirect.com/science/article/pii/S0040609000015443> (cit. on p. 27).

- [10] P. Silberzan, L. Leger, D. Ausserre, and J. J. Benattar. “Silanation of silica surfaces. A new method of constructing pure or mixed monolayers”. In: *Langmuir* 7.8 (Aug. 1991), pp. 1647–1651. ISSN: 0743-7463. DOI: [10.1021/la00056a017](https://doi.org/10.1021/la00056a017). URL: <http://dx.doi.org/10.1021/la00056a017> (cit. on p. 27).
- [11] A. Seeboth and W. Hettrich. “Spatial orientation of highly ordered self-assembled silane monolayers on glass surfaces”. In: *Journal of Adhesion Science and Technology* 11.4 (1997), pp. 495–505. ISSN: 0169-4243. DOI: [10.1163/156856197X00048](https://doi.org/10.1163/156856197X00048). URL: <http://www.tandfonline.com/doi/abs/10.1163/156856197X00048> (cit. on p. 29).
- [12] Zheng Li, Volker Schön, Patrick Huber, Jörg Kressler, and Karsten Busse. “Comparison of the Monolayer Formation of Fluorinated and Nonfluorinated Amphiphilic Block Copolymers at the Air-Water Interface”. In: *J. Phys. Chem. B* 113.35 (Aug. 2009), pp. 11841–11847. ISSN: 1520-6106. DOI: [10.1021/jp905016s](https://doi.org/10.1021/jp905016s). URL: <http://dx.doi.org/10.1021/jp905016s> (cit. on pp. 33, 35).
- [13] P. G. de Gennes. “Conformations of Polymers Attached to an Interface”. In: *Macromolecules* 13.5 (Sept. 1980), pp. 1069–1075. ISSN: 0024-9297. DOI: [10.1021/ma60077a009](https://doi.org/10.1021/ma60077a009). URL: <http://dx.doi.org/10.1021/ma60077a009> (cit. on p. 33).
- [14] S. Alexander. “Adsorption of chain molecules with a polar head a scaling description”. In: *Journal de Physique* 38.8 (1977), pp. 983–987. ISSN: 0302-0738. DOI: [10.1051/jphys:01977003808098300](https://doi.org/10.1051/jphys:01977003808098300). URL: [http://jphys.journaldephysique.org/index.php?option=com\\_article&access=standard&Itemid=129&url=/articles/jphys/abs/1977/08/jphys\\_1977\\_\\_38\\_8\\_983\\_0/jphys\\_1977\\_\\_38\\_8\\_983\\_0.html](http://jphys.journaldephysique.org/index.php?option=com_article&access=standard&Itemid=129&url=/articles/jphys/abs/1977/08/jphys_1977__38_8_983_0/jphys_1977__38_8_983_0.html) (cit. on p. 33).
- [15] A. M. Gonçalves da Silva, E. J. M. Filipe, J. M. R. d’Oliveira, and J. M. G. Martinho. “Interfacial Behavior of Poly(styrene)-Poly(ethylene oxide) Diblock Copolymer Monolayers at the Air-Water Interface. Hydrophilic Block Chain Length and Temperature Influence”. In: *Langmuir* 12.26 (1996), pp. 6547–6553. DOI: [10.1021/la960604+](https://doi.org/10.1021/la960604+). URL: <http://pubs.acs.org/doi/abs/10.1021/la960604%2B> (cit. on p. 33).
- [16] Michael S. Kent, Lay Theng Lee, Bernard Farnoux, and Francis Rondelez. “Characterization of diblock copolymer monolayers at the liquid-air interface by neutron reflectivity and surface tension measurements”. In: *Macromolecules* 25.23 (Nov. 1992), pp. 6240–6247. ISSN: 0024-9297. DOI: [10.1021/ma00049a021](https://doi.org/10.1021/ma00049a021). URL: <http://dx.doi.org/10.1021/ma00049a021> (cit. on p. 33).
- [17] J. M. H. M. Scheutjens, G. J. Fleer, M. A. Cohen Stuart, T. Cosgrove, and B. Vincent. *Polymers at Interfaces*. en. Springer, Sept. 1993. ISBN: 9780412581601 (cit. on p. 33).
- [18] Frank E. Runge, Michael S. Kent, and Hyuk Yu. “Capillary Wave Investigation of Surface Films of Diblock Copolymers on an Organic Subphase: Poly(dimethylsiloxane)-Poly(styrene) Films at the Air/Ethyl Benzoate Interface”. In: *Langmuir* 10.6 (June 1994), pp. 1962–1970. ISSN: 0743-7463. DOI: [10.1021/la00018a056](https://doi.org/10.1021/la00018a056). URL: <http://dx.doi.org/10.1021/la00018a056> (cit. on p. 33).

- [19] S. T. Milner, T. A. Witten, and M. E. Cates. “Theory of the grafted polymer brush”. In: *Macromolecules* 21.8 (Aug. 1988), pp. 2610–2619. ISSN: 0024-9297. DOI: [10.1021/ma00186a051](https://doi.org/10.1021/ma00186a051). URL: <http://dx.doi.org/10.1021/ma00186a051> (cit. on p. 33).
- [20] Samuel Zalipsky and J. Milton Harris. “Introduction to Chemistry and Biological Applications of Poly(ethylene glycol)”. In: *Poly(ethylene glycol)*. Vol. 680. ACS Symposium Series. Washington, DC: American Chemical Society, Aug. 1997, pp. 1–13. ISBN: 978-0841235373. URL: <http://pubs.acs.org/doi/abs/10.1021/bk-1997-0680.ch001> (cit. on p. 33).
- [21] J. D. Andrade, V. Hlady, and S.-I. Jeon. “Poly(ethylene oxide) and Protein Resistance”. In: *Hydrophilic Polymers*. Vol. 248. Advances in Chemistry. Jan. 1996, pp. 51–59. ISBN: 9780841231337. URL: <http://pubs.acs.org/doi/abs/10.1021/ba-1996-0248.ch003> (cit. on p. 33).
- [22] Danilo D. Lasic. “Doxorubicin in sterically stabilized liposomes”. en. In: *Nature* 380.6574 (Apr. 1996), pp. 561–562. DOI: [10.1038/380561a0](https://doi.org/10.1038/380561a0). URL: <http://www.nature.com/nature/journal/v380/n6574/abs/380561a0.html> (cit. on p. 33).
- [23] Martin C. Woodle and Danilo D. Lasic. “Sterically stabilized liposomes”. In: *Biochimica et Biophysica Acta (BBA) - Reviews on Biomembranes* 1113.2 (Aug. 1992), pp. 171–199. ISSN: 03044157. DOI: [10.1016/0304-4157\(92\)90038-C](https://doi.org/10.1016/0304-4157(92)90038-C). URL: <http://europepmc.org/abstract/MED/1510996/reload=0;jsessionid=9964qVX3GbCJEK0ve0jg.22> (cit. on p. 33).
- [24] Suraj Chandra Sharma, Durga P. Acharya, Miguel García-Roman, Yasuo Itami, and Hironobu Kunieda. “Phase behavior and surface tensions of amphiphilic fluorinated random copolymer aqueous solutions”. In: *Colloids and Surfaces A: Physicochemical and Engineering Aspects* 280.1–3 (June 2006), pp. 140–145. ISSN: 0927-7757. DOI: [10.1016/j.colsurfa.2006.01.047](https://doi.org/10.1016/j.colsurfa.2006.01.047). URL: <http://www.sciencedirect.com/science/article/pii/S0927775706000938> (cit. on pp. 33, 35).
- [25] Mercedes G. Muñoz, Francisco Monroy, Francisco Ortega, Ramón G. Rubio, and Dominique Langevin. “Monolayers of Symmetric Triblock Copolymers at the Air-Water Interface. 1. Equilibrium Properties”. In: *Langmuir* 16.3 (Feb. 2000), pp. 1083–1093. ISSN: 0743-7463. DOI: [10.1021/la990142a](https://doi.org/10.1021/la990142a). URL: <http://dx.doi.org/10.1021/la990142a> (cit. on p. 33).
- [26] Alexander Wesemann, Heiko Ahrens, Roland Steitz, Stephan Förster, and Christiane A. Helm. “Internal Interface of a Compressed PEE-PEO Diblock Copolymer Monolayer”. In: *Langmuir* 19.3 (Feb. 2003), pp. 709–716. ISSN: 0743-7463. DOI: [10.1021/la0204592](https://doi.org/10.1021/la0204592). URL: <http://dx.doi.org/10.1021/la0204592> (cit. on p. 33).

- [27] Ploysai Kaewsaiha, Kozo Matsumoto, and Hideki Matsuoka. “Synthesis and Nanostructure of Strong Polyelectrolyte Brushes in Amphiphilic Diblock Copolymer Monolayers on a Water Surface”. In: *Langmuir* 20.16 (Aug. 2004), pp. 6754–6761. ISSN: 0743-7463. DOI: [10.1021/la0491145](https://doi.org/10.1021/la0491145). URL: <http://dx.doi.org/10.1021/la0491145> (cit. on p. 33).
- [28] J. Zhu, A. Eisenberg, and R. B. Lennox. “Interfacial behavior of block polyelectrolytes. 5. Effect of varying block lengths on the properties of surface micelles”. In: *Macromolecules* 25.24 (Nov. 1992), pp. 6547–6555. ISSN: 0024-9297. DOI: [10.1021/ma00050a025](https://doi.org/10.1021/ma00050a025). URL: <http://dx.doi.org/10.1021/ma00050a025> (cit. on pp. 33, 34).
- [29] J. Zhu, A. Eisenberg, and R. B. Lennox. “Interfacial behavior of block polyelectrolytes. 6. Properties of surface micelles as a function of R and X in P(S260-b-VP240/RX)”. In: *Macromolecules* 25.24 (Nov. 1992), pp. 6556–6562. ISSN: 0024-9297. DOI: [10.1021/ma00050a026](https://doi.org/10.1021/ma00050a026). URL: <http://dx.doi.org/10.1021/ma00050a026> (cit. on pp. 33, 34).
- [30] Karsten Busse, Chiranjeevi Peetla, and Jörg Kressler. “Water Surface Covering of Fluorinated Amphiphilic Triblock Copolymers: Surface Pressure-Area and X-ray Reflectivity Investigations”. In: *Langmuir* 23.13 (June 2007), pp. 6975–6982. ISSN: 0743-7463. DOI: [10.1021/la0637059](https://doi.org/10.1021/la0637059). URL: <http://dx.doi.org/10.1021/la0637059> (cit. on p. 33).
- [31] Chiranjeevi Peetla, Karlheinz Graf, and Jörg Kressler. “Langmuir monolayer and Langmuir–Blodgett films of amphiphilic triblock copolymers with water-soluble middle block”. en. In: *Colloid and Polymer Science* 285.1 (Oct. 2006), pp. 27–37. ISSN: 0303-402X, 1435-1536. DOI: [10.1007/s00396-006-1527-2](https://doi.org/10.1007/s00396-006-1527-2). URL: <http://link.springer.com/article/10.1007/s00396-006-1527-2> (cit. on p. 33).
- [32] M. C. Fauré, P. Bassereau, L. T. Lee, A. Menelle, and C. Lheveder. “Phase Transitions in Monolayers of PS-PEO Copolymer at the Air-Water Interface”. In: *Macromolecules* 32.25 (Dec. 1999), pp. 8538–8550. ISSN: 0024-9297. DOI: [10.1021/ma9900840](https://doi.org/10.1021/ma9900840). URL: <http://dx.doi.org/10.1021/ma9900840> (cit. on p. 33).
- [33] Heiko Ahrens, Stephan Förster, and Christiane A. Helm. “Polyelectrolyte Brushes Grafted at the Air/Water Interface”. In: *Macromolecules* 30.26 (Dec. 1997), pp. 8447–8452. ISSN: 0024-9297. DOI: [10.1021/ma970949e](https://doi.org/10.1021/ma970949e). URL: <http://dx.doi.org/10.1021/ma970949e> (cit. on p. 33).
- [34] Emiko Mouri, Kozo Matsumoto, and Hideki Matsuoka. “Carpetlike dense-layer formation in a polyelectrolyte brush at the air/water interface”. en. In: *Journal of Polymer Science Part B: Polymer Physics* 41.16 (2003), 1921–1928. ISSN: 1099-0488. DOI: [10.1002/polb.10561](https://doi.org/10.1002/polb.10561). URL: <http://onlinelibrary.wiley.com/doi/10.1002/polb.10561/abstract> (cit. on p. 33).

- [35] J.R. Lu, T.J. Su, R.K. Thomas, J. Penfold, and R.W. Richards. “The determination of segment density profiles of polyethylene oxide layers adsorbed at the air-water interface”. In: *Polymer* 37.1 (1996), pp. 109–114. ISSN: 0032-3861. DOI: [10.1016/0032-3861\(96\)81605-3](https://doi.org/10.1016/0032-3861(96)81605-3). URL: <http://www.sciencedirect.com/science/article/pii/0032386196816053> (cit. on pp. 33, 34).
- [36] E. P. K. Currie, F. A. M. Leermakers, M. A. Cohen Stuart, and G. J. Fleer. “Grafted Adsorbing Polymers: Scaling Behavior and Phase Transitions”. In: *Macromolecules* 32.2 (Jan. 1999), pp. 487–498. ISSN: 0024-9297. DOI: [10.1021/ma970525k](https://doi.org/10.1021/ma970525k). URL: <http://dx.doi.org/10.1021/ma970525k> (cit. on pp. 33, 34).
- [37] Emiko Mouri, Kozo Matsumoto, and Hideki Matsuoka. “Effect of pH on the nanostructure of an amphiphilic carbosilane/methacrylic acid block copolymer at air/water interface”. In: *Journal of Applied Crystallography* 36.3 (Apr. 2003), pp. 722–726. ISSN: 0021-8898. DOI: [10.1107/S0021889803006125](https://doi.org/10.1107/S0021889803006125). URL: <http://scripts.iucr.org/cgi-bin/paper?S0021889803006125> (cit. on p. 33).
- [38] Emiko Mouri, Ploysai Kaewsaiha, Kozo Matsumoto, Hideki Matsuoka, and Naoya Torikai. “Effect of Salt Concentration on the Nanostructure of Weak Polyacid Brush in the Amphiphilic Polymer Monolayer at the Air/Water Interface”. In: *Langmuir* 20.24 (Nov. 2004), pp. 10604–10611. ISSN: 0743-7463. DOI: [10.1021/la047847j](https://doi.org/10.1021/la047847j). URL: <http://dx.doi.org/10.1021/la047847j> (cit. on p. 33).
- [39] Emiko Mouri, Yasuyuki Furuya, Kozo Matsumoto, and Hideki Matsuoka. “Hydrophilic Chain Length Dependence of the Ionic Amphiphilic Polymer Monolayer Structure at the Air/Water Interface”. In: *Langmuir* 20.19 (Sept. 2004), pp. 8062–8067. ISSN: 0743-7463. DOI: [10.1021/la049256z](https://doi.org/10.1021/la049256z). URL: <http://dx.doi.org/10.1021/la049256z> (cit. on p. 33).
- [40] Emiko Mouri and Hideki Matsuoka. “Nanostructure of Ionic Amphiphilic Block Copolymer Monolayer at Air / Water Interface”. In: *Dekker Encyclopedia of Nanoscience and Nanotechnology*. Taylor & Francis, Dec. 2007, pp. 2519–2529. ISBN: 0-8247-5055-1. URL: <http://www.tandfonline.com/doi/abs/10.1081/E-ENN-120014211> (cit. on p. 33).
- [41] C. Barentin, P. Muller, and J. F. Joanny. “Polymer Brushes Formed by End-Capped Poly(ethylene oxide) (PEO) at the Air-Water Interface”. In: *Macromolecules* 31.7 (Apr. 1998), pp. 2198–2211. ISSN: 0024-9297. DOI: [10.1021/ma971665x](https://doi.org/10.1021/ma971665x). URL: <http://dx.doi.org/10.1021/ma971665x> (cit. on p. 34).
- [42] C. Barentin and J. F. Joanny. “Surface Pressure of Adsorbed Polymer Layers. Effect of Sticking Chain Ends”. In: *Langmuir* 15.5 (Mar. 1999), pp. 1802–1811. ISSN: 0743-7463. DOI: [10.1021/la981173t](https://doi.org/10.1021/la981173t). URL: <http://dx.doi.org/10.1021/la981173t> (cit. on p. 34).
- [43] Heiko Ahrens, Thomas Rosleff Bækmark, Rudolf Merkel, Johannes Schmitt, Karlheinz Graf, Roberto Raiteri, and Christiane A. Helm. “Hydrophilic/Hydrophobic Nanostripes in Lipopolymer Monolayers”. en. In: *ChemPhysChem* 1.2 (2000), 101–106. ISSN: 1439-7641. DOI: [10.1002/1439-7641\(20000915\)1:2<101::AID-](https://doi.org/10.1002/1439-7641(20000915)1:2<101::AID-)

- CPHC101>3.0.CO;2-0. URL: [http://onlinelibrary.wiley.com/doi/10.1002/1439-7641\(20000915\)1:2<101::AID-CPHC101>3.0.CO;2-0/abstract](http://onlinelibrary.wiley.com/doi/10.1002/1439-7641(20000915)1:2<101::AID-CPHC101>3.0.CO;2-0/abstract) (cit. on p. 34).
- [44] H. Ahrens, K. Graf, and C. A. Helm. “Observation of a Superstructure X-ray Peak within Lipopolymer Monolayers on the Water Surface”. In: *Langmuir* 17.11 (May 2001), pp. 3113–3115. ISSN: 0743-7463. DOI: [10.1021/la001464d](https://doi.org/10.1021/la001464d). URL: <http://dx.doi.org/10.1021/la001464d> (cit. on p. 34).
- [45] Zhong Xu, Nolan B. Holland, and Roger E. Marchant. “Conformations of Short-Chain Poly(ethylene oxide) Lipopolymers at the Air-Water Interface: A Combined Film Balance and Surface Tension Study”. In: *Langmuir* 17.2 (Jan. 2001), pp. 377–383. ISSN: 0743-7463. DOI: [10.1021/la0006770](https://doi.org/10.1021/la0006770). URL: <http://dx.doi.org/10.1021/la0006770> (cit. on p. 34).
- [46] Yongsok Seo, Alan R. Esker, Daewon Sohn, Hyong-Jun Kim, Sangwook Park, and Hyuk Yu. “Study on the Behaviors of Different Polystyrene-block-Poly(methyl methacrylate) Diblock Copolymers Adsorbed at the Air/Water Interface”. In: *Langmuir* 19.8 (Apr. 2003), pp. 3313–3322. ISSN: 0743-7463. DOI: [10.1021/la020819l](https://doi.org/10.1021/la020819l). URL: <http://dx.doi.org/10.1021/la020819l> (cit. on p. 34).
- [47] Jean-Louis Gallani, Stéphane Mery, Yves Galerne, and Daniel Guillon. “Organization of a Polar Molecule at the Air-Water Interface”. In: *The Journal of Physical Chemistry B* 108.31 (Aug. 2004), pp. 11627–11632. ISSN: 1520-6106. DOI: [10.1021/jp049612m](https://doi.org/10.1021/jp049612m). URL: <http://dx.doi.org/10.1021/jp049612m> (cit. on p. 34).
- [48] Amit Kulkarni, Juergen Reiche, and Andreas Lendlein. “Hydrolytic degradation of poly(rac-lactide) and poly[(rac-lactide)-co-glycolide] at the air–water interface”. en. In: *Surface and Interface Analysis* 39.9 (2007), 740–746. ISSN: 1096-9918. DOI: [10.1002/sia.2580](https://doi.org/10.1002/sia.2580). URL: <http://onlinelibrary.wiley.com/doi/10.1002/sia.2580/abstract> (cit. on p. 34).
- [49] B. Bangar Raju, Françoise M. Winnik, and Yotaro Morishima. “A Look at the Thermodynamics of the Association of Amphiphilic Polyelectrolytes in Aqueous Solutions: Strengths and Limitations of Isothermal Titration Calorimetry”. In: *Langmuir* 17.14 (July 2001), pp. 4416–4421. ISSN: 0743-7463. DOI: [10.1021/la001554i](https://doi.org/10.1021/la001554i). URL: <http://dx.doi.org/10.1021/la001554i> (cit. on p. 34).
- [50] Jan Kevelam, Silvia Martinucci, Jan B. F. N. Engberts, Wilfried Blokzijl, John van de Pas, Han Blonk, Peter Versluis, and Antonie J. W. G. Visser. “Microstructure of Dispersions of Lamellar Droplets Carrying Anchoring Hydrophobically Endcapped Poly(sodium acrylate)s as Novel Steric Stabilizers”. In: *Langmuir* 15.15 (July 1999), pp. 4989–5001. ISSN: 0743-7463. DOI: [10.1021/la981636v](https://doi.org/10.1021/la981636v). URL: <http://dx.doi.org/10.1021/la981636v> (cit. on p. 34).

- [51] Siwar Trabelsi, Zhongcheng Zhang, Shishan Zhang, T. Randall Lee, and Daniel K. Schwartz. “Correlating Linactant Efficiency and Self-Assembly: Structural Basis of Line Activity in Molecular Monolayers”. In: *Langmuir* 25.14 (July 2009), pp. 8056–8061. ISSN: 0743-7463. DOI: [10.1021/la900565m](https://doi.org/10.1021/la900565m). URL: <http://dx.doi.org/10.1021/la900565m> (cit. on p. 34).
- [52] Hazrat Hussain, Hendrik Budde, Siegfried Höring, Karsten Busse, and Jörg Kressler. “Synthesis and characterization of poly(ethylene oxide) and poly(perfluorohexylethyl methacrylate) containing triblock copolymers”. en. In: *Macromolecular Chemistry and Physics* 203.14 (2002), 2103–2112. ISSN: 1521-3935. DOI: [10.1002/1521-3935\(200210\)203:14<2103::AID-MACP2103>3.0.CO;2-X](https://doi.org/10.1002/1521-3935(200210)203:14<2103::AID-MACP2103>3.0.CO;2-X). URL: [http://onlinelibrary.wiley.com/doi/10.1002/1521-3935\(200210\)203:14<2103::AID-MACP2103>3.0.CO;2-X/abstract](http://onlinelibrary.wiley.com/doi/10.1002/1521-3935(200210)203:14<2103::AID-MACP2103>3.0.CO;2-X/abstract) (cit. on pp. 34, 35).
- [53] Jianguo Wang, Guoping Mao, Christopher K. Ober, and Edward J. Kramer. “Liquid Crystalline, Semifluorinated Side Group Block Copolymers with Stable Low Energy Surfaces: Synthesis, Liquid Crystalline Structure, and Critical Surface Tension”. In: *Macromolecules* 30.7 (Apr. 1997), pp. 1906–1914. ISSN: 0024-9297. DOI: [10.1021/ma961412o](https://doi.org/10.1021/ma961412o). URL: <http://dx.doi.org/10.1021/ma961412o> (cit. on p. 34).
- [54] Jan Genzer, Easan Sivaniah, Edward J. Kramer, Jianguo Wang, Hilmar Körner, Maoliang Xiang, Kookheon Char, Christopher K. Ober, Benjamin M. DeKoven, Robert A. Bubeck, Manoj K. Chaudhury, Sharadha Sambasivan, and Daniel A. Fischer. “The Orientation of Semifluorinated Alkanes Attached to Polymers at the Surface of Polymer Films”. In: *Macromolecules* 33.5 (Mar. 2000), pp. 1882–1887. ISSN: 0024-9297. DOI: [10.1021/ma991182o](https://doi.org/10.1021/ma991182o). URL: <http://dx.doi.org/10.1021/ma991182o> (cit. on p. 34).
- [55] Jan Genzer, Easan Sivaniah, Edward J. Kramer, Jianguo Wang, Hilmar Körner, Kookheon Char, Christopher K. Ober, Benjamin M. DeKoven, Robert A. Bubeck, Daniel A. Fischer, and Sharadha Sambasivan. “Temperature Dependence of Molecular Orientation on the Surfaces of Semifluorinated Polymer Thin Films”. In: *Langmuir* 16.4 (Feb. 2000), pp. 1993–1997. ISSN: 0743-7463. DOI: [10.1021/la9910327](https://doi.org/10.1021/la9910327). URL: <http://dx.doi.org/10.1021/la9910327> (cit. on p. 34).
- [56] Akira Hirao, Kenji Sugiyama, and Hideaki Yokoyama. “Precise synthesis and surface structures of architectural per- and semifluorinated polymers with well-defined structures”. In: *Progress in Polymer Science* 32.12 (Dec. 2007), pp. 1393–1438. ISSN: 0079-6700. DOI: [10.1016/j.progpolymsci.2007.08.001](https://doi.org/10.1016/j.progpolymsci.2007.08.001). URL: <http://www.sciencedirect.com/science/article/pii/S0079670007001013> (cit. on p. 34).
- [57] Takashige Maekawa, Satoshi Kamata, and Masashi Matsuo. “The relationship between structures and dynamic surface properties of perfluoroalkyl containing polymers”. In: *Journal of Fluorine Chemistry* 54.1–3 (Sept. 1991), p. 84. ISSN: 0022-1139. DOI: [10.1016/S0022-1139\(00\)83594-0](https://doi.org/10.1016/S0022-1139(00)83594-0). URL: <http://>

- [www.sciencedirect.com/science/article/pii/S0022113900835940](http://www.sciencedirect.com/science/article/pii/S0022113900835940) (cit. on p. 34).
- [58] J. C. Ravey, A. Gherbi, and M. J. Stébé. “Comparative study of fluorinated and hydrogenated nonionic surfactants. I. Surface activity properties and critical concentrations”. In: *Trends in Colloid and Interface Science II*. Ed. by V. Degiorgio. Progress in Colloid & Polymer Science 76. Steinkopff, Jan. 1988, pp. 234–241. ISBN: 978-3-7985-0777-7, 978-3-7985-1693-9. URL: <http://link.springer.com/chapter/10.1007/BFb0114199> (cit. on p. 35).
- [59] Katja Jankova, Jens H. Truelsen, Xianyi Chen, Jørgen Kops, and Walther Batsberg. “Controlled/“living” atom transfer radical polymerization of styrene in the synthesis of amphiphilic diblock copolymers from a poly(ethylene glycol) macroinitiator”. en. In: *Polymer Bulletin* 42.2 (Mar. 1999), pp. 153–158. ISSN: 0170-0839, 1436-2449. DOI: [10.1007/s002890050447](https://doi.org/10.1007/s002890050447). URL: <http://link.springer.com/article/10.1007/s002890050447> (cit. on p. 35).
- [60] Katja Jankova, Xianyi Chen, Jorgen Kops, and Walther Batsberg. “Synthesis of Amphiphilic PS-b-PEG-b-PS by Atom Transfer Radical Polymerization”. In: *Macromolecules* 31.2 (Jan. 1998), pp. 538–541. ISSN: 0024-9297. DOI: [10.1021/ma9710186](https://doi.org/10.1021/ma9710186). URL: <http://dx.doi.org/10.1021/ma9710186> (cit. on p. 35).
- [61] Timothy E. Patten and Krzysztof Matyjaszewski. “Atom Transfer Radical Polymerization and the Synthesis of Polymeric Materials”. en. In: *Advanced Materials* 10.12 (1998), 901–915. ISSN: 1521-4095. DOI: [10.1002/\(SICI\)1521-4095\(199808\)10:12<901::AID-ADMA901>3.0.CO;2-B](https://doi.org/10.1002/(SICI)1521-4095(199808)10:12<901::AID-ADMA901>3.0.CO;2-B). URL: [http://onlinelibrary.wiley.com/doi/10.1002/\(SICI\)1521-4095\(199808\)10:12<901::AID-ADMA901>3.0.CO;2-B/abstract](http://onlinelibrary.wiley.com/doi/10.1002/(SICI)1521-4095(199808)10:12<901::AID-ADMA901>3.0.CO;2-B/abstract) (cit. on p. 35).
- [62] Jiro Ueda, Mutsuhiro Matsuyama, Masami Kamigaito, and Mitsuo Sawamoto. “Multifunctional Initiators for the Ruthenium-Mediated Living Radical Polymerization of Methyl Methacrylate: Di- and Trifunctional Dichloroacetates for Synthesis of Multiarmed Polymers<sup>1</sup>”. In: *Macromolecules* 31.3 (Feb. 1998), pp. 557–562. ISSN: 0024-9297. DOI: [10.1021/ma970476b](https://doi.org/10.1021/ma970476b). URL: <http://dx.doi.org/10.1021/ma970476b> (cit. on p. 35).
- [63] Kwon Taek Lim, Min Young Lee, Myung Jun Moon, Gun Dae Lee, Seong-Soo Hong, Jasper L Dickson, and Keith P Johnston. “Synthesis and properties of semifluorinated block copolymers containing poly(ethylene oxide) and poly(fluorooctyl methacrylates) via atom transfer radical polymerisation”. In: *Polymer* 43.25 (2002), pp. 7043–7049. ISSN: 0032-3861. DOI: [10.1016/S0032-3861\(02\)00636-5](https://doi.org/10.1016/S0032-3861(02)00636-5). URL: <http://www.sciencedirect.com/science/article/pii/S0032386102006365> (cit. on p. 35).
- [64] S. M. Baker, K. A. Leach, C. E. Devereaux, and D. E. Gragson. “Controlled Patterning of Diblock Copolymers by Monolayer Langmuir-Blodgett Deposition”. In: *Macromolecules* 33.15 (July 2000), pp. 5432–5436. ISSN: 0024-9297. DOI: [10.1021/ma992029x](https://doi.org/10.1021/ma992029x). URL: <http://dx.doi.org/10.1021/ma992029x> (cit. on p. 36).

- [65] C. A. Devereaux and S. M. Baker. “Surface Features in Langmuir-Blodgett Monolayers of Predominantly Hydrophobic Poly(styrene)-Poly(ethylene oxide) Diblock Copolymer”. In: *Macromolecules* 35.5 (Feb. 2002), pp. 1921–1927. ISSN: 0024-9297. DOI: [10.1021/ma011319m](https://doi.org/10.1021/ma011319m). URL: <http://dx.doi.org/10.1021/ma011319m> (cit. on p. 36).
- [66] Nanfeng Zheng, Jie Fan, and Galen D. Stucky. “One-Step One-Phase Synthesis of Monodisperse Noble-Metallic Nanoparticles and Their Colloidal Crystals”. In: *J. Am. Chem. Soc.* 128.20 (2006), pp. 6550–6551. ISSN: 0002-7863. DOI: [10.1021/ja0604717](https://doi.org/10.1021/ja0604717). URL: <http://dx.doi.org/10.1021/ja0604717> (cit. on p. 41).
- [67] Andrea Tao, Prasert Sinsermsuksakul, and Peidong Yang. “Tunable plasmonic lattices of silver nanocrystals”. en. In: *Nature Nanotechnology* 2.7 (2007), pp. 435–440. ISSN: 1748-3387. DOI: [10.1038/nnano.2007.189](https://doi.org/10.1038/nnano.2007.189). URL: <http://www.nature.com/nnano/journal/v2/n7/abs/nnano.2007.189.html> (cit. on p. 41).
- [68] Raghuveer Parthasarathy, Xiao-Min Lin, and Heinrich M. Jaeger. “Electronic Transport in Metal Nanocrystal Arrays: The Effect of Structural Disorder on Scaling Behavior”. In: *Physical Review Letters* 87.18 (Oct. 2001), p. 186807. DOI: [10.1103/PhysRevLett.87.186807](https://doi.org/10.1103/PhysRevLett.87.186807). URL: <http://link.aps.org/doi/10.1103/PhysRevLett.87.186807> (cit. on p. 41).
- [69] M. K. Bera, M. K. Sanyal, S. Pal, J. Daillant, A. Datta, G. U. Kulkarni, D. Luzet, and O. Kononov. “Reversible buckling in monolayer of gold nanoparticles on water surface”. In: *Europhysics Letters (EPL)* 78.5 (June 2007), p. 56003. ISSN: 0295-5075, 1286-4854. DOI: [10.1209/0295-5075/78/56003](https://doi.org/10.1209/0295-5075/78/56003). URL: <http://iopscience.iop.org/0295-5075/78/56003> (cit. on p. 41).
- [70] David G. Schultz, Xiao-Min Lin, Dongxu Li, Jeff Gebhardt, Mati Meron, James Viccaro, and Binhua Lin. “Structure, Wrinkling, and Reversibility of Langmuir Monolayers of Gold Nanoparticles”. In: *The Journal of Physical Chemistry B* 110.48 (Dec. 2006), pp. 24522–24529. ISSN: 1520-6106. DOI: [10.1021/jp063820s](https://doi.org/10.1021/jp063820s). URL: <http://dx.doi.org/10.1021/jp063820s> (cit. on p. 41).
- [71] Terry P. Bigioni, Xiao-Min Lin, Toan T. Nguyen, Eric I. Corwin, Thomas A. Witten, and Heinrich M. Jaeger. “Kinetically driven self assembly of highly ordered nanoparticle monolayers”. en. In: *Nature Materials* 5.4 (Mar. 2006), pp. 265–270. ISSN: 1476-1122. DOI: [10.1038/nmat1611](https://doi.org/10.1038/nmat1611). URL: <http://www.nature.com/nmat/journal/v5/n4/abs/nmat1611.html> (cit. on pp. 42, 47, 56).
- [72] Jungwon Park, Haimei Zheng, Won Chul Lee, Phillip L. Geissler, Eran Rabani, and A. Paul Alivisatos. “Direct Observation of Nanoparticle Superlattice Formation by Using Liquid Cell Transmission Electron Microscopy”. In: *ACS Nano* 6.3 (2012), pp. 2078–2085. ISSN: 1936-0851. DOI: [10.1021/nm203837m](https://doi.org/10.1021/nm203837m). URL: <http://dx.doi.org/10.1021/nm203837m> (cit. on p. 42).

- [73] Suresh Narayanan, Jin Wang, and Xiao-Min Lin. “Dynamical Self-Assembly of Nanocrystal Superlattices during Colloidal Droplet Evaporation by in situ Small Angle X-Ray Scattering”. In: *Physical Review Letters* 93.13 (Sept. 2004), p. 135503. DOI: [10.1103/PhysRevLett.93.135503](https://doi.org/10.1103/PhysRevLett.93.135503). URL: <http://link.aps.org/doi/10.1103/PhysRevLett.93.135503> (cit. on pp. 42, 44, 58).
- [74] Klara E. Mueggenburg, Xiao-Min Lin, Rodney H. Goldsmith, and Heinrich M. Jaeger. “Elastic membranes of close-packed nanoparticle arrays”. en. In: *Nature Materials* 6.9 (July 2007), pp. 656–660. ISSN: 1476-1122. DOI: [10.1038/nmat1965](https://doi.org/10.1038/nmat1965). URL: <http://www.nature.com/nmat/journal/v6/n9/full/nmat1965.html> (cit. on pp. 42, 58).
- [75] Jiebin Pang, Shisheng Xiong, Felix Jaeckel, Zaicheng Sun, Darren Dunphy, and C. Jeffrey Brinker. “Free-Standing, Patternable Nanoparticle/Polymer Monolayer Arrays Formed by Evaporation Induced Self-Assembly at a Fluid Interface”. In: *J. Am. Chem. Soc.* 130.11 (2008), pp. 3284–3285. ISSN: 0002-7863. DOI: [10.1021/ja710994m](https://doi.org/10.1021/ja710994m). URL: <http://dx.doi.org/10.1021/ja710994m> (cit. on pp. 42, 58).
- [76] Girish Muralidharan, Navakanta Bhat, and Venugopal Santhanam. “Scalable processes for fabricating non-volatile memory devices using self-assembled 2D arrays of gold nanoparticles as charge storage nodes”. In: *Nanoscale* 3.11 (2011), p. 4575. ISSN: 2040-3364, 2040-3372. DOI: [10.1039/c1nr10884k](https://doi.org/10.1039/c1nr10884k). URL: <http://pubs.rsc.org/en/Content/ArticleLanding/2011/NR/c1nr10884k> (cit. on p. 42).
- [77] Haeng Sub Wi, Sreeram Cingarapu, Ken J. Klabunde, Chris M. Sorensen, and Bruce M. Law. “Observation of Nanoparticle-Enhanced Marangoni Transport near a Freezing Out Front”. In: *The Journal of Physical Chemistry C* 116.10 (Mar. 2012), pp. 6052–6057. ISSN: 1932-7447. DOI: [10.1021/jp211691q](https://doi.org/10.1021/jp211691q). URL: <http://dx.doi.org/10.1021/jp211691q> (cit. on p. 42).
- [78] J.W. Jansen, C.G. de Kruif, and A. Vrij. “Attractions in sterically stabilized silica dispersions: II. Experiments on phase separation induced by temperature variation”. In: *Journal of Colloid and Interface Science* 114.2 (Dec. 1986), pp. 481–491. ISSN: 0021-9797. DOI: [10.1016/0021-9797\(86\)90433-9](https://doi.org/10.1016/0021-9797(86)90433-9). URL: <http://www.sciencedirect.com/science/article/pii/0021979786904339> (cit. on pp. 42, 55).
- [79] Benjamin Abécassis, Fabienne Testard, and Olivier Spalla. “Gold Nanoparticle Superlattice Crystallization Probed In Situ”. In: *Physical Review Letters* 100.11 (Mar. 2008), p. 115504. DOI: [10.1103/PhysRevLett.100.115504](https://doi.org/10.1103/PhysRevLett.100.115504). URL: <http://link.aps.org/doi/10.1103/PhysRevLett.100.115504> (cit. on pp. 42, 55).
- [80] Philip Born, Eoin Murray, and Tobias Kraus. “Temperature-induced particle self-assembly”. In: *Journal of Physics and Chemistry of Solids* 71.2 (Feb. 2010), pp. 95–99. ISSN: 0022-3697. DOI: [10.1016/j.jpcs.2009.09.011](https://doi.org/10.1016/j.jpcs.2009.09.011). URL: <http://www.sciencedirect.com/science/article/pii/S0022369709002662> (cit. on p. 42).

- [81] Joseph Kao, Peter Bai, J. Matthew Lucas, A. Paul Alivisatos, and Ting Xu. “Size-Dependent Assemblies of Nanoparticle Mixtures in Thin Films”. In: *Journal of the American Chemical Society* 135.5 (Feb. 2013), pp. 1680–1683. ISSN: 0002-7863. DOI: [10.1021/ja3107912](https://doi.org/10.1021/ja3107912). URL: <http://dx.doi.org/10.1021/ja3107912> (cit. on p. 42).
- [82] J.W. Jansen, C.G. de Kruif, and A. Vrij. “Attractions in sterically stabilized silica dispersions: I. Theory of phase separation”. In: *Journal of Colloid and Interface Science* 114.2 (Dec. 1986), pp. 471–480. ISSN: 0021-9797. DOI: [10.1016/0021-9797\(86\)90432-7](https://doi.org/10.1016/0021-9797(86)90432-7). URL: <http://www.sciencedirect.com/science/article/pii/0021979786904327> (cit. on pp. 42, 55).
- [83] Siddique J. Khan, F. Pierce, C. M. Sorensen, and A. Chakrabarti. “Self-Assembly of Ligated Gold Nanoparticles: Phenomenological Modeling and Computer Simulations†”. In: *Langmuir* 25.24 (2009), pp. 13861–13868. ISSN: 0743-7463. DOI: [10.1021/la9008202](https://doi.org/10.1021/la9008202). URL: <http://dx.doi.org/10.1021/la9008202> (cit. on p. 42).
- [84] Haeng Sub Wi, Sreeram Cingarapu, Ken J. Klabunde, and Bruce M. Law. “Nanoparticle Adsorption at Liquid–Vapor Surfaces: Influence of Nanoparticle Thermodynamics, Wettability, and Line Tension”. In: *Langmuir* 27.16 (2011), pp. 9979–9984. ISSN: 0743-7463. DOI: [10.1021/la201791g](https://doi.org/10.1021/la201791g). URL: <http://dx.doi.org/10.1021/la201791g> (cit. on p. 42).
- [85] Shengfeng Cheng and Gary S. Grest. “Structure and Diffusion of Nanoparticle Monolayers Floating at Liquid/Vapor Interfaces: A Molecular Dynamics Study”. In: *arXiv:1205.0224* (May 2012). URL: <http://arxiv.org/abs/1205.0224> (cit. on pp. 42, 44).
- [86] István Robel, Xiao-Min Lin, Michael Sprung, and Jin Wang. “Thermal stability of two-dimensional gold nanocrystal superlattices”. In: *Journal of Physics: Condensed Matter* 21.26 (July 2009), p. 264011. ISSN: 0953-8984, 1361-648X. DOI: [10.1088/0953-8984/21/26/264011](https://doi.org/10.1088/0953-8984/21/26/264011). URL: <http://iopscience.iop.org/0953-8984/21/26/264011> (cit. on p. 44).
- [87] R. Banerjee, S. Hazra, S. Banerjee, and M. K. Sanyal. “Nanopattern formation in self-assembled monolayers of thiol-capped Au nanocrystals”. In: *Physical Review E* 80.5 (Nov. 2009), p. 056204. DOI: [10.1103/PhysRevE.80.056204](https://doi.org/10.1103/PhysRevE.80.056204). URL: <http://link.aps.org/doi/10.1103/PhysRevE.80.056204> (cit. on p. 44).
- [88] S. Kutuzov, J. He, R. Tangirala, T. Emrick, T. P. Russell, and A. Böker. “On the kinetics of nanoparticle self-assembly at liquid/liquid interfaces”. In: *Physical Chemistry Chemical Physics* 9.48 (2007), p. 6351. ISSN: 1463-9076, 1463-9084. DOI: [10.1039/b710060b](https://doi.org/10.1039/b710060b). URL: <http://pubs.rsc.org/en/Content/ArticleLanding/2007/CP/b710060b> (cit. on p. 44).

- 
- [89] P.A. Kralchevsky, N.D. Denkov, V.N. Paunov, O.D. Velev, I.B. Ivanov, H. Yoshimura, and K. Nagayama. “Formation of two-dimensional colloid crystals in liquid films under the action of capillary forces”. In: *Journal of Physics: Condensed Matter* 6.23A (June 1994), A395–A402. ISSN: 0953-8984, 1361-648X. DOI: [10.1088/0953-8984/6/23A/065](https://doi.org/10.1088/0953-8984/6/23A/065). URL: <http://iopscience.iop.org/0953-8984/6/23A/065> (cit. on p. 44).
- [90] H. Kashiwagi and T. Makita. “Viscosity of twelve hydrocarbon liquids in the temperature range 298–348 K at pressures up to 110 MPa”. en. In: *International Journal of Thermophysics* 3.4 (Dec. 1982), pp. 289–305. ISSN: 0195-928X, 1572-9567. DOI: [10.1007/BF00502346](https://doi.org/10.1007/BF00502346). URL: <http://link.springer.com/article/10.1007/BF00502346> (cit. on p. 46).
- [91] Stephen M. Danauskas, Dongxu Li, Mati Meron, Binhua Lin, and Ka Yee C. Lee. “Stochastic fitting of specular X-ray reflectivity data using StochFit”. In: *Journal of Applied Crystallography* 41.6 (Nov. 2008), pp. 1187–1193. ISSN: 0021-8898. DOI: [10.1107/S0021889808032445](https://doi.org/10.1107/S0021889808032445). URL: <http://scripts.iucr.org/cgi-bin/paper?S0021889808032445> (cit. on p. 47).

# Acknowledgements

While any attempt to recognize everyone I owe my gratitude to would be futile, I shall certainly try.

First and foremost, I'd like to thank my supervisor Prof. Dr. Patrick Huber for giving me the opportunity to compose my dissertation in his research group. His advice and the discussions we had were instrumental to the success of this study.

Along the same line, I want to thank my fellow PhD students, most of all René Berwanger, Simon Grüner, Anke Henschel, Christoph Schäfer and Matthias Wolff for the entertaining and fruitful atmosphere.

Moreover, all the members of the research groups Huber, Knorr and Wagner as well as the administrative and technical personnel share my appreciation: Elke Huschens and Evelyn Treib, Karin Kretsch and Rolf Kiefer as well as the staff of the university workshop of Michael Schmidt and electronical technicians Jürgen Hoppe and Stefan Loew. Assembling and maintaining the reflectometer would not have been possible without them.

Thank you to Prof. Dr. Christian Wagner for providing me with shelter in his research group for the last few months.

I also have to thank Dr. Karsten Busse, Dr. Tobias Kraus and Dr. Philip Born for the interesting topics they brought into our research group and to my attention and for their input on various subjects.

Special thanks to my family and friends. Among the latter, the support of my roommates (both present and past) Sarah Meiser, Bastian Jung, Tina Momper, Daniel Krauß and my proofreader Steffen Witt stands out. – Thank you, guys.